Advanced Photonic Measurement Techniques for Fiber Optic Characterization, Sensing and Imaging

by

Yifei Wang

Submitted in partial fulfillment of

The requirements of the degree of

Doctor of Philosophy

Department of Electrical and Electronic Engineering

The University of Melbourne

September 2017

Abstract

In the past few years, coherent detection has achieved dramatic success due to adoption of powerful electronic digital signal processing (DSP). In the meantime, direct detection (DD) based optical communication systems have also attracted attentions because of its low cost and simple implementation. The directly-detected optical channel, however, is nonlinear due to the square-law detection of the photo-diodes. In order to remove the nonlinearity, it is necessary to calibrate the response for each optoelectronic component.

In the meantime, the rapid growth of the bandwidth-rich internet applications has driven the research in maximizing the capacity of optical transport. As the spectral efficiency (SE) in single-mode fiber (SMF) is ultimately limited by the fiber nonlinearity, the natural solution is to use large effective-area SMF, or even multi-mode fiber (MMF) with center launch technique to excite only the fundamental (LP_{01}) mode to mitigate the nonlinearity penalty. Most importantly, MMF or few-mode fiber (FMF) supports many spatial modes, and therefore the fiber capacity can be increased in theory by taking advantage of this additional degree of freedom in space aided by multiple-input multiple-output (MIMO) transmission.

In this thesis, we propose and demonstrate a novel digital signal processing (DSP) algorithm for photodiode characterization probed by three wavelengths. The DSP algorithm has low computational complexity and scales only with logarithmic of number of the spectral points. We verify our proposed algorithm by measuring the phase response of an electrical filter. We also characterize the frequency response for a high-speed optical receiver with 30-GHz bandwidth photodiode, and a low-speed optical receiver with 14-GHz bandwidth photodiode, respectively.

For the investigation of few-mode fibers (FMFs), we present novel design and fabrication of few-mode fiber based optical sensors. Particularly, we report two FMF based discrete sensors, one is a fiber Sangac loop sensor based on polarimetric interference, and the other is a few-mode interferometer sensor based on

intermodal interference. We also continue to introduce the concept of FMF based distributed sensors. We demonstrate characterization of SBS in a FMF based on Brillouin optical time domain analysis (BOTDA) technique and propose two BOTDA methods for the FMF. The proposed setup can also be used as a Brillouin distributed sensor.

For the characterization of the modal propagation in few-mode fibers (FMFs), we propose and implement a novel method called complex imaging to recover both amplitude and phase images and coherently detect the in-phase and quadrature components of the heterodyne signal simultaneously with a pair of charge-coupled device (CCD) cameras. In this way, both amplitude mode pattern and phase mode pattern (or mode image) for modes transmitted in optical fibers could be characterized. In this thesis, we characterize mode patterns of pure fundamental mode and higher-order modes in FMFs as a validation of our imaging method. Then our method is also applied to mode decomposition and modal content analysis of an arbitrary mixed mode pattern. Finally, we also sweep the input wavelength and measure differential mode delay (DMD) in FMFs.

Declaration

(i) This thesis comprises only my original work towards the degree of Doctor of Philosophy except where indicated in the preface;

(ii) due acknowledgement has been made in the text to all other material used; and

(iii) this thesis is fewer than the maximum word limit in length, exclusive of tables, maps, bibliographies and appendices

Signature_____

Date_____

Preface

(i) Contents arising from each contributing chapter towards the thesis:

Original contributions (overall percentage: 90%) of Chapter 3: proposed the DSP algorithm for photodiode characterization, including problem formulation; verified the proposed algorithm; demonstrated experiments of frequency response calibration; processed collected data and analyzed experimental results.

Contributions from co-contributors (overall percentage: 10%) of Chapter 3: supervised overall development of work (name of co-contributors: William Shieh); guided and aided experimental design (name of co-contributors: Xi Chen and William Shieh).

Original contributions (overall percentage: 70%) of Chapter 4: derived formula of temperature and strain sensitivity for FMF based discrete optical sensors; designed experimental setup for FMF based discrete optical sensors; demonstrated experiments, processed collected data and analyzed experimental results for FMF based discrete optical sensors; aided experimental design for FMF based distributed optical sensors.

Contributions from co-contributors (overall percentage: 30%) of Chapter 4: designed experimental setup, demonstrated experiments, processed collected data and analyzed experimental results for FMF based distributed optical sensors (name of co-contributors: An Li); guided and aided experimental design for FMF based discrete optical sensors (name of co-contributors: An Li, William Shieh); supervised overall development of work (name of co-contributors: William Shieh).

Original contributions (overall percentage: 90%) of Chapter 5: proposed and implemented a novel technique for complex imaging, including problem formulation; designed experimental setup; configured digital signal

processing procedures; demonstrated experiments, including simulation for comparison; processed collected data and analyzed experimental results.

Contributions from co-contributors (overall percentage: 10%) of Chapter 5: supervised overall development of work (name of co-contributors: William Shieh); guided and aided experimental design (name of co-contributors: An Li, William Shieh)

(ii) None of the work towards the thesis has been submitted for other qualifications.

(iii) None of the work towards the thesis was carried out prior to enrolment in the degree.

(iv) No third party editorial assistance was provided in preparation of the thesis.

(v) Publications arising from each contributing chapter towards the thesis:

Publications arising from Chapter 3:

1) Y Wang, Q Hu, X Chen, T Anderson, W Shieh, “Using 3 wavelengths to measure photodiode phase response with laser phase noise robustness”, Optical Fibre Technology, 2014 OptoElectronics and Communication Conference (2014)

   Contributions from co-authors: Yifei Wang (overall percentage: 85 %): wrote the manuscript, experimental design, conducted experiments, and data analysis. Qian Hu (overall percentage: 2 %): helped to evaluate and edit the manuscript. Xi Chen (overall percentage: 5 %): guided and aided experimental design. Trevor Anderson (overall percentage: 2 %): helped to evaluate and edit the manuscript. William Shieh (overall percentage: 6 %): supervised overall development of work; guided and aided experimental design; helped to evaluate and edit the manuscript.

2) Y Wang, Q Hu, X Chen, A Li, T Anderson, W Shieh, “3-λ characterization of phase response for optical receivers”, Optics letters 39 (3), 670-673 (2014)

Contributions from co-authors: Yifei Wang (overall percentage: 85 %): wrote the manuscript, experimental design, conducted experiments, and data analysis. Qian Hu (overall percentage: 2 %): helped to evaluate and edit the manuscript. Xi Chen (overall percentage: 4 %): guided and aided experimental design. Trevor Anderson (overall percentage: 2 %): helped to evaluate and edit the manuscript. An Li (overall percentage: 2 %): helped to evaluate and edit the manuscript. William Shieh (overall percentage: 5 %): supervised overall development of work; guided and aided experimental design; helped to evaluate and edit the manuscript.

Publications arising from Chapter 4:

1) Y Wang, A Li, X Chen, W Shieh, “Characterization of temperature and strain sensitivity of low cost few-mode fiber based interferometer sensor”, CLEO: Science and Innovations, SM2O. 3 (2015)

Contributions from co-authors: Yifei Wang (overall percentage: 85 %): wrote the manuscript, experimental design, conducted experiments, and data analysis. An Li (overall percentage: 5 %): guided and aided experimental design. Xi Chen (overall percentage: 2 %): helped to evaluate and edit the manuscript. William Shieh (overall percentage: 8 %): supervised overall development of work; guided and aided experimental design; helped to evaluate and edit the manuscript.

2) Y Wang, A Li, X Chen, Q Hu, W Shieh, “Characterization of in-line interferometric based temperature sensors in two-mode fibers”, Asia Communications and Photonics Conference, AW3D. 4 (2014)

Contributions from co-authors: Yifei Wang (overall percentage: 85 %): wrote the manuscript, experimental design, conducted experiments, and

data analysis. An Li (overall percentage: 5 %): guided and aided experimental design. Xi Chen (overall percentage: 2 %): helped to evaluate and edit the manuscript. Qian Hu (overall percentage: 2 %): helped to evaluate and edit the manuscript. William Shieh (overall percentage: 6 %): supervised overall development of work; guided and aided experimental design; helped to evaluate and edit the manuscript.

3) A Li, Y Wang, Q Hu, W Shieh, “Few-mode fiber based optical sensors”, Optics express 23 (2), 1139-1150

   Contributions from co-authors: An Li (overall percentage: 55 %): wrote the manuscript, experimental design, conducted experiments, and data analysis. Yifei Wang (overall percentage: 35 %): experimental design, conducted experiments, and data analysis. Qian Hu (overall percentage: 2 %): aided experimental design, helped to evaluate and edit the manuscript. William Shieh (overall percentage: 8 %): supervised overall development of work; guided and aided experimental design; helped to evaluate and edit the manuscript.

4) A Li, Y Wang, J Fang, W Shieh, “Distributed temperature and strain discrimination using a few-mode fiber”, CLEO: Science and Innovations, SM1L. 3

   Contributions from co-authors: An Li (overall percentage: 85 %): wrote the manuscript, experimental design, conducted experiments, and data analysis. Yifei Wang (overall percentage: 5 %): aided experimental design, helped to evaluate and edit the manuscript. Jian Fang (overall percentage: 5 %): helped to evaluate and edit the manuscript. William Shieh (overall percentage: 5 %): supervised overall development of work; guided and aided experimental design; helped to evaluate and edit the manuscript.

5) A Li, Y Wang, J Fang, MJ Li, BY Kim, W Shieh, “Few-mode fiber multi-parameter sensor with distributed temperature and strain discrimination”, Optics letters 40 (7), 1488-1491

Contributions from co-authors: An Li (overall percentage: 85 %): wrote the manuscript, experimental design, conducted experiments, and data analysis. Yifei Wang (overall percentage: 4 %): aided experimental design, helped to evaluate and edit the manuscript. Jian Fang (overall percentage: 2 %): helped to evaluate and edit the manuscript. Mingjun Li (overall percentage: 2 %): helped to evaluate and edit the manuscript. Byoung Yoon Kim (overall percentage: 2 %): helped to evaluate and edit the manuscript. William Shieh (overall percentage: 5 %): supervised overall development of work; guided and aided experimental design; helped to evaluate and edit the manuscript.

6) A Li, Y Wang, Q Hu, D Che, X Chen, W Shieh, "Measurement of distributed mode coupling in a few-mode fiber using a reconfigurable Brillouin OTDR", Optics letters 39 (22), 6418-6421

   Contributions from co-authors: An Li (overall percentage: 85 %): wrote the manuscript, experimental design, conducted experiments, and data analysis. Yifei Wang (overall percentage: 4 %): aided experimental design, helped to evaluate and edit the manuscript. Qian Hu (overall percentage: 2 %): helped to evaluate and edit the manuscript. Di Che (overall percentage: 2 %): helped to evaluate and edit the manuscript. Xi Chen (overall percentage: 2 %): helped to evaluate and edit the manuscript. William Shieh (overall percentage: 5 %): supervised overall development of work; guided and aided experimental design; helped to evaluate and edit the manuscript.

Publications arising from Chapter 5:

1) Y Wang, J Fang, A Li, Q Yang, W Shieh, "Complex imaging via coherent detection", Optics Express 25 (15), 17294-17305 (2017)

   Contributions from co-authors: Yifei Wang (overall percentage: 85 %): wrote the manuscript, experimental design, conducted experiments, and data analysis. Jian Fang (overall percentage: 2 %): helped to evaluate and

edit the manuscript. An Li (overall percentage: 2 %): guided and aided experimental design. Qi Yang (overall percentage: 2 %): helped to evaluate and edit the manuscript. William Shieh (overall percentage: 9 %): supervised overall development of work; guided and aided experimental design; helped to evaluate and edit the manuscript.

2) Y Wang, X Chen, A Li, J Fang, Q Yang, W Shieh, “Complex imaging for detecting few-mode fiber modes”, Signal Processing in Photonic Communications, SpTh2D. 3 (2017)

   Contributions from co-authors: Yifei Wang (overall percentage: 85 %): wrote the manuscript, experimental design, conducted experiments, and data analysis. Xi Chen (overall percentage: 2 %): helped to evaluate and edit the manuscript. An Li (overall percentage: 2 %): guided and aided experimental design. Jian Fang (overall percentage: 2 %): helped to evaluate and edit the manuscript. Qi Yang (overall percentage: 2 %): helped to evaluate and edit the manuscript. William Shieh (overall percentage: 7 %): supervised overall development of work; guided and aided experimental design; helped to evaluate and edit the manuscript.

3) Y Wang, J Fang, A Li, Q Yang, W Shieh, “Nearfield complex imaging”, Optical Fiber Communication Conference, Th4H. 4 (2017)

   Contributions from co-authors: Yifei Wang (overall percentage: 85 %): wrote the manuscript, experimental design, conducted experiments, and data analysis. Jian Fang (overall percentage: 2 %): helped to evaluate and edit the manuscript. An Li (overall percentage: 2 %): guided and aided experimental design. Qi Yang (overall percentage: 2 %): helped to evaluate and edit the manuscript. William Shieh (overall percentage: 9 %): supervised overall development of work; guided and aided experimental design; helped to evaluate and edit the manuscript.

(vi) Research towards the thesis was supported by the Australian Government through the Australian Research Council's Linkage Projects funding scheme

with project title ‘High-performance and cost-effective coherent OTDR’ and linkage grant number LP150101270.

Acknowledgement

This thesis is a summary of my academic work during my Ph.D. candidature at the University of Melbourne, which cannot be finished without the help and supports from so many incredible individuals.

First and foremost, I would like to give my sincerest gratitude to my supervisors, Prof. William Shieh and Dr. Trevor Anderson, for their high-quality supervision, patient guidance, constant encouragement and generous support during my entire Ph.D. candidature. Their profound thinking and technical insights have inspired me and helped me develop deep understanding on my research topic.

In addition, I would like to express my sincere gratitude to Dr. Fred Buchali at Bell Labs, Alcatel-Lucent Germany, for providing me an internship opportunity. It was an invaluable experience for me to learn from him and other experts at Bell Labs.

My sincere gratitude also goes to my Ph.D. advisory committee member, Prof. Ying Tan, for her stimulating discussion and precious advice. Moreover, I am thankful to the University of Melbourne, Department of Electrical & Electronic Engineering and NICTA Victoria Research Laboratory for offering me the scholarship, as well as the outstanding research environment and facilities.

Also, I would like to thank my colleagues and friends who have helped me during the past: Qian Hu, An Li, Di Che, Jian Fang, Miao Sun, Chuanbowen Sun, Xi Chen, Hamid Khodakarami, Lihua Ruan, Tian Liang and Yu Tian. I especially appreciate their assistance and encouragement during the time I experienced difficulties.

I am forever indebted to my loving parents, Mr. Wang and Mrs. Xu, for their unconditional love, sacrifice and endless support. It is cruel that I got so much time in study, and so little with my family. Especially my dearest grandparents Hancheng and Jindi, that I never got the chance to say goodbye to them. I owe my family so much that words cannot express. I will always find them in here, my heart.

Contents

List of Figures

List of Tables

1 Introduction

1.1 Introduction

The rapid growth of the bandwidth-rich internet applications has driven the research in maximizing the capacity of optical transport. Meanwhile, tremendous breakthrough in high- speed optical transmission networks has been made by utilizing polarization multiplexing, high-order modulation and coherent optical detection, in both coherent single carrier and multi-carrier formats. As the spectral efficiency (SE) in single-mode fiber (SMF) is ultimately limited by the fiber nonlinearity, the natural solution is to use large effective-area SMF, or even multi-mode fiber (MMF) with center launch technique to excite only the fundamental (LP01) mode to mitigate the nonlinearity penalty. Most importantly, MMF or few-mode fiber (FMF) supports many spatial modes, and therefore the fiber capacity can be increased in theory by taking advantage of this additional degree of freedom in the form of multiple-input multiple-output (MIMO) transmission [1]. To date, three types of SDM transmission experiments have been demonstrated: (i) core-multiplexed transmission over multi-core fiber (MCF), (ii) MDM transmission over single-core FMF, and (iii) core multiplexed MDM transmission over FM-MCF. The highest capacity (1.01 Pb/s) of core-multiplexed transmission is demonstrated by Takara et al. [2] in a 52 km single span of 12-core MCF in 2012. In the other experiment by Igarashi et al. in 2013 [3], the reach is extended to 7326 km and net total capacity is 140.7 Tb/s, leading to a record capacity–distance product of 1030.8 Pb／s × km. Recent developments on FMF fabrication and FM-EDFAs have enabled demonstration of long-distance MDM transmission. Long-haul transmission using FMF with inline amplification via parallel single-mode EDFAs was first demonstrated in 2012 [4] with maximum transmission distance of 4200 km. Enabled by an FM-EDFA with modal gain equalization, the first loop experiment with an inline FM-EDFA was demonstrated in 2013[5].

1.2 Fibers types for fiber-optic communications

❖ *Single-mode fibers (SMF)*

SMFs are optical fibers which are designed such that they support only a single propagation mode (LP01) per polarization for a given wavelength. Higher-order modes like LP_{11}, LP_{20}, etc., do not exist, except for only cladding modes which are not localized around the fiber core. SMFs usually have a relatively small core (with a diameter of only a few microns) and a small refractive index difference between core and cladding. The mode radius is typically a few microns. However, there are also large mode area fibers with a relatively large mode area [6-8].

A peculiar property of SMFs is that the transverse intensity profile at the fiber output has a fixed shape, which is independent of the launch conditions and the spatial properties of the injected light, assuming no significant birefringence in the fiber. The launch conditions only influence the efficiency with which light can be coupled into the guided mode.

Intermodal dispersion can of course not occur in SMFs if we temporarily ignore the polarization dispersion. This is an important advantage for the application in optical fiber communications at high data rates (multiple Gbit/s), particularly for long distances. Essentially for this very reason, as well for their extremely low propagation losses, SMFs are exclusively used for long-haul data transmission, and for most of the outdoor short-reach applications. For short-reach indoor use, MMF are more common, mostly because that allows the use of cheaper multimode data transmitters which can couple the light into the MMF more efficiently.

❖ *Multi-mode fibers (MMF)*

MMFs are optical fibers which support multiple transverse guided modes for a given optical frequency and polarization [9]. The number of guided modes is determined by the wavelength and the refractive index profile. For step-index fibers, the relevant quantities are the core radius and the numerical aperture (NA), which in combination determine the V number. For large V values, the number of modes is proportional to V^2. Particularly for fibers with a relatively large core (right-hand side

in Fig. 1.1), the number of supported modes can be very high. Such fibers can guide light with poor beam quality (e.g. generated with a high-power diode bar), but for preserving the beam quality of a light source with higher brightness it can be better to use a fiber with smaller core and moderate NA, even though efficient launching can then be more difficult.

Compared with standard SMFs, MMFs usually have significantly larger core areas, but also generally a higher NA in the order of 0.2–0.3. High NA leads to robust guidance, even under conditions of tight bending, but also to higher propagation losses without bending, as irregularities at the core–cladding interface can scatter light more effectively. The refractive index profile can be rectangular (step-index fibers), or parabolic, etc.

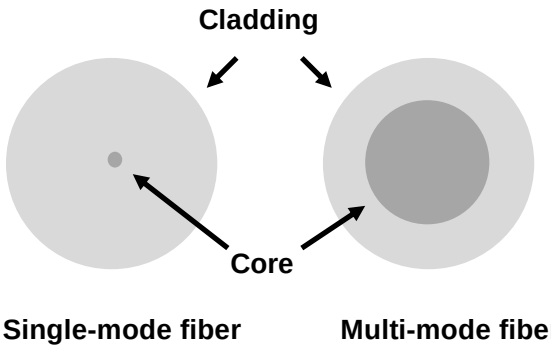

Fig. 1.1. A single-mode fiber (left, the core to cladding diameter ratio is usually 9 microns to 125 microns in construction) has a core which is very small compared with the cladding, whereas a multi-mode fiber (right, the core to cladding diameter ratio is usually 50 microns to 125 microns and 62.5 microns to 125 microns in construction) can have a large core.

❖ *Few-mode fibers (FMF)*

There is the distinction between SMF, supporting only one guided mode per polarization, and conventional MMF, supporting hundreds of guided mode. For the multimode fibers supporting only a relatively small number of guided modes – for example, from 2 to 15 modes, the term 'few-mode fiber' (FMF) is commonly used.

The guided modes are usually characterized as linearly polarized (LP) modes under weakly- guiding condition. For example, a six-mode fiber may have the

LP_{01} (fundamental mode), LP_{11}, LP_{21}, LP_{02}, LP_{31} and LP_{12}. As all modes with non-zero azimuthal index exist with two different spatial orientations, the full number of spatial modes is actually $2+4\times 2=10$. Also counting polarization directions, one would arrive at the total number of modes of 20. Similarly, a two-mode fiber (with LP_{01} and LP_{11}) actually possesses 6 different modes considering spatial and polarization degeneracies [10-13].

In contrast to SMF, in FMF one can have intermodal nonlinear effects such as inter-modal cross-phase modulation and parametric amplification, and also those involving nonlinearities with a delayed response such as stimulated Brillouin scattering. The tendency for such phenomena can be increased in fibers with low differential mode delay (DMD).

1.3 Motivations for using few-mode fiber devices

Compared to the MMF solution, FMF can have three advantages: first, with FMF, mode selective coupling/splitting can be controlled more accurately by fiber-based or free-space optics, and therefore the performance of mode multiplexer and de-multiplexer of FMF can be improved over MMF. Second, in spatial-mode multiplexed systems aided by MIMO signal processing [14], the group delay between selectively launched propagation modes can be equalized either by a time or frequency domain filter, or by a large cyclic prefix (CP) overhead in the case of orthogonal frequency-division multiplexing (OFDM). This computation complexity is directly related to the number of modes involved because the channel delay and channel matrix size are proportional to the mode number. Utilizing only a few modes can reduce the computation complexity to a manageable level. Third, existence of only few modes can result in negligible modal mixing in the FMF due to large mismatch of modal effective indices. Subsequently we could achieve simple capacity improvement by having an efficient method of individually exciting and selectively detecting the orthogonal modes in a FMF.

Initial effort has been concentrated on TMFs [1, 15-17], having V-numbers between 2.4 and 3.8, which support two spatial modes, namely the LP_{01} and LP_{11}

modes in the weakly guiding approximation. Precise measurement of propagation velocities of the two modes is possible using prism output coupling of the evanescent fields. The beat length between the two modes for a given fiber shows a small variation over the operating wavelength range, and commercially available fibers have beat lengths ranging from a few tens to a few hundreds of microns depending upon the core size and the index difference between the core and cladding. A more complete manipulation of the guided modes could be achieved using an inter-modal coupler and a highly selective modal filter. The inter-modal coupler coherently couples optical power from one mode to the other using an externally applied periodic microbend whose period is the same as the beat length between the two modes. The modal filter provides means of separating the two guided modes into two separate fibers through an evanescent field directional coupler formed by a TMF and a SMF. This device demonstrates more than 25 dB mode selectivity. These components form the basis for advanced forms of TMF devices.

A potentially important application of highly elliptical core TMF is fiber optic interferometric sensors, where two arms of the interferometer consist of the two spatial modes [10]. The basic components are again inter-modal couplers and modal filters that combine and separate the optical waves for the two modes. This type of interferometer is compact and can be very sensitive to certain parameters while immune to others due to the fact that the two arms of the interferometer occupy the same physical space. Basically it senses the differential phase shift between the two modes in response to environmental perturbations. Several unique characteristics of this kind of interferometer stem from the fact that the group velocities of the two modes are the same at a particular wavelength for a given fiber while the phase velocities are different. This implies that a low coherence source or short optical pulses can be used without losing the interference signal, and that source phase induced intensity noise can be eliminated.

1.4 Thesis outline

The content of the thesis is structured as follows:

Chapter 1 Introduction This chapter reviews different fiber types for fiber-optic communications, their properties and advantages/disadvantages. The motivation for using few-mode fiber devices is also introduced in this chapter. We focus on the advanced optical characterization and photonic measurement, which includes characterization for optical systems, investigation of FMF optical sensors, and demonstration of advanced coherent complex imaging.

Chapter 2 Literature Review In this chapter, the motivation of the frequency response characterization is illustrated first. Then, we review the principle, the architecture and the development of space-division-multiplexed systems for ultra-high-capacity optical transmission. Finally, we review recent developments in fiber optic sensors (FOSs) and the potential to use FMFs as in-line FOSs.

Chapter 3 Characterization of Frequency Response for Optical Receivers with Laser Phase Noise Robustness This chapter first introduces the motivations and fundamentals to characterize the frequency response of the optical receivers. Then the chapter introduces the principle of 2 - λ approach for amplitude response and 3 - λ approach for phase response, which includes theoretical fundamentals, algorithm derivation, and calibration arrangement of the approach. After that, we verify our proposed 3 - λ approach by comparing the phase response of an electrical filter calibrated through the proposed 3 - λ approach with that calibrated through conventional back-to-back electrical signal. For the experiment, we demonstrate the frequency response calibration of a high-speed optical receiver with 30-GHz bandwidth photodiode, and a low-speed optical receiver with 14-GHz bandwidth photodiode.

Chapter 4 Few-mode Fiber Based Optical Sensors In this chapter, we review our recent progress in the design and fabrication of FMF based optical sensors. Firstly, we review some fundamentals of fiber-based optical sensors and FMFs. Secondly, we report two FMF-based discrete sensors, one is a fiber Sangac loop interferometer sensor based on polarimetric interference, and the other

is a few-mode interferometer sensor based on intermodal interference. The system configurations of both sensors are illustrated and their sensitivities to the temperature and strain are shown and compared. Thirdly, we move on to FMF based distributed sensors. We review the basic concept of stimulated Brillouin scattering (SBS), and demonstrate characterization of SBS in a FMF based on Brillouin optical time domain analysis (BOTDA) technique. We also propose two BOTDA methods for FMF used as a Brillouin distributed sensor. We launch a pump and a probe signal through specific LP modes into a FMF, and monitor the Brillouin frequency shift (BFS) in each mode. By analyzing the temperature and strain coefficients of the BFS of the two lowest order (LP_{01}, LP_{11}) modes, discrimination of temperature and strain is successfully demonstrated.

Chapter 5 Complex Imaging via Coherent Detection In this chapter, we propose and implement a novel method to recover both amplitude and phase images and to coherently detect the in-phase and quadrature components of the heterodyne signal simultaneously with a pair of CCD cameras. Firstly, we introduce the motivations and review current technologies of complex imaging. Secondly, we give the fundamentals of our proposed complex imaging technique including the principles and theoretical algorithms. Thirdly, we introduce the system configuration and the digital signal processing (DSP) procedures of complex imaging, and then demonstrate mode fields in the far-field and near-field of a TMF using complex imaging technique, including theoretical fundamentals and simulation results for comparison. Finally, we use our proposed imaging technique for fiber characterizations. We firstly characterize mode patterns of pure fundamental mode and higher-order modes in FMFs as a validation of our imaging method. Next our method is also applied to mode decomposition and modal content analysis of an arbitrary mixed mode pattern. Furthermore, we sweep the input wavelength and measure differential mode delay (DMD) in FMFs.

Chapter 6 Conclusions In this chapter the main results of the thesis are reviewed and summarized.

1.5 Contributions

The contributions of this work in thesis are listed as follows:

Chapter 3 We propose a novel DSP algorithm for photodiode characterization probed by three wavelengths. The DSP algorithm has low computational complexity and scales only with logarithmic of the number of spectral points. We verify our proposed algorithm by measuring the phase response of an electrical filter. Specifically, we demonstrate the frequency response calibration of a high-speed optical receiver with 30-GHz bandwidth, and a low-speed optical receiver with 14-GHz bandwidth, respectively. For the first time, the phase response of photodiode is characterized up to 20 GHz.

Chapter 4 We report our recent progress in the design and fabrication of FMF based optical sensors. Firstly, we characterize the performance of discrete optical sensor based on interferometer structure. The first kind is polarimetric interferometer sensor in a polarization-maintaining (PM) FMF utilizing mode beating between the polarizations (x and y), and wavelength shift of the interfering transmission spectrum against temperature and strain is characterized as -1.72 nm/°C and 24.5 pm/με. The second kind is intermodal interferometer sensor in a TMF utilizing mode beating between the spatial modes (LP_{01} and LP_{11}), and its wavelength shift against temperature and strain is characterized as -0.043 nm/℃ and -0.0023 nm/με. The proposed TMF intermodal interferometer sensor exhibits great potential due to high interfering visibility, good linearity, high sensitivity, and low cost. We then present the concept of a distributed optical sensor based on SBS effect in a FMF. We demonstrate efficient generation of Brillouin dynamic grating (BDG) in a FMF using two counter propagating pump waves in LP_{01} mode and one probe wave in LP_{11} mode. Combined with coherent detection and optical time-domain analysis, we propose a unique FMF based multi-parameter optical fiber sensor for distributed measurement of temperature and strain, with an accuracy of 1.2 °C and 21.9 με.

Chapter 5 We propose the concept of complex imaging via coherent detection for acquiring two-dimensional nearfield optical image that recovers amplitude and

phase simultaneously. We then illustrate the system configurations and the DSP procedures for our novel imaging technique, and also demonstrate the experimental results of mode fields in the far-field and near-field for a TMF. Based on the proposed coherent complex imaging, we experimentally demonstrate the technique by imaging FMF modes with high extinction-ratio of > 17 dB. Complete mode decomposition is also performed using complex imaging in FMFs, and cross-correlation coefficients between the experimental complex fields and reconstructed complex fields are above 0.99. Finally we also characterize the FMF DMD which agrees well with the theoretical predication.

1.6 Publications

1. Y Wang, X Chen, A Li, J Fang, Q Yang, W Shieh, “Complex imaging for detecting few-mode fiber modes”, Signal Processing in Photonic Communications, SpTh2D. 3 (2017)

2. Y Wang, J Fang, A Li, Q Yang, W Shieh, “Complex imaging via coherent detection”, Optics Express 25 (15), 17294-17305 (2017)

3. Y Wang, J Fang, A Li, Q Yang, W Shieh, “Nearfield complex imaging”, Optical Fiber Communication Conference, Th4H. 4 (2017)

4. Y Wang, A Li, X Chen, W Shieh, “Characterization of temperature and strain sensitivity of low cost few-mode fiber based interferometer sensor”, CLEO: Science and Innovations, SM2O. 3 (2015)

5. Y Wang, A Li, X Chen, Q Hu, W Shieh, “Characterization of in-line interferometric based temperature sensors in two-mode fibers”, Asia Communications and Photonics Conference, AW3D. 4 (2014)

6. Y Wang, Q Hu, X Chen, T Anderson, W Shieh, “Using 3 wavelengths to measure photodiode phase response with laser phase noise robustness”, Optical Fibre Technology, 2014 OptoElectronics and Communication Conference (2014)

7. Y Wang, Q Hu, X Chen, A Li, T Anderson, W Shieh, “3-λ characterization of phase response for optical receivers”, Optics letters 39 (3), 670-673 (2014)

8. A Li, Y Wang, J Fang, W Shieh, “Distributed temperature and strain discrimination using a few-mode fiber”, CLEO: Science and Innovations, SM1L. 3

9. A Li, Y Wang, J Fang, MJ Li, BY Kim, W Shieh, “Few-mode fiber multi-parameter sensor with distributed temperature and strain discrimination”, Optics letters 40 (7), 1488-1491

10. A Li, Y Wang, Q Hu, W Shieh, “Few-mode fiber based optical sensors”, Optics express 23 (2), 1139-1150

11. A Li, Y Wang, Q Hu, D Che, X Chen, W Shieh, “Measurement of distributed mode coupling in a few-mode fiber using a reconfigurable Brillouin OTDR”, Optics letters 39 (22), 6418-6421

12. Q Hu, D Che, Y Wang, F Yuan, Q Yang, W Shieh, “Complex modulation and detection with directly modulated lasers”, Optics express 23 (25), 32809-32819

13. Q Hu, D Che, Y Wang, A Li, J Fang, W Shieh, “Beyond amplitude-only detection for digital coherent system using directly modulated laser”, Optics letters 40 (12), 2762-2765

14. Q Hu, D Che, Y Wang, W Shieh, PMD induced impairment mitigation in Stokes vector direct detection systems”, Optical Fiber Communications Conference and Exhibition (OFC), 2015, 1-3

15. Q Hu, D Che, Y Wang, W Shieh, “Advanced modulation formats for high-performance short-reach optical interconnects”, Optics express 23 (3), 3245-3259

16. A Li, X Chen, D Che, Y Wang, W Shieh, “Capacity Limit of Few-Mode Fibers for Space-Division Multiplexed Coherent Optical OFDM Superchannel”, Asia Communications and Photonics Conference, AW3F. 1

17. A Li, Q Hu, D Che, Y Wang, W Shieh, “Measurement of distributed mode coupling in a few-mode fiber using a Brillouin optical time domain reflectometer”, Optical Communication (ECOC), 2014 European Conference on, 1-3

18. D Che, F Yuan, Q Yang, H Khodakarami, Y Wang, J Fang, W Shieh, “Reinventing Optical Direct Modulation by Frequency Chirp”, Asia Communications and Photonics Conference, AF1C. 3

19. D Che, A Li, X Chen, Q Hu, Y Wang, W Shieh, “Stokes vector direct detection for linear complex optical channels”, Journal of Lightwave Technology 33 (3), 678-684

20. D Che, X Chen, A Li, Q Hu, Y Wang, W Shieh, “Optical direct detection for 100G short reach applications”, Asia Communications and Photonics Conference, AF1H. 4

21. D Che, A Li, X Chen, Q Hu, Y Wang, W Shieh, “160-Gb/s stokes vector direct detection for short reach optical communication”, Optical Fiber Communication Conference, Th5C. 7

22. D Che, A Li, X Chen, Q Hu, Y Wang, W Shieh, “Stokes vector direct detection for short-reach optical communication”, Optics letters 39 (11), 3110-3113

23. X Chen, D Che, A Li, J He, Y Wang, Q Hu, W Shieh, “Training Symbol Assisted Signal-to-Signal Beat Noise Cancellation for Direct Detected Optical OFDM Systems”, Asia Communications and Photonics Conference, AF1E. 2

24. A Li, D Che, X Chen, Q Hu, Y Wang, W Shieh, “Signal-to-Signal Beat Noise Cancellation for Direct Detection Optical OFDM System Based on Block-wise Signal Phase Switching”, Asia Communications and Photonics Conference, AF1E. 6

25. A Li, D Che, X Chen, Q Hu, Y Wang, W Shieh, “48.8-Gb/s 16-QAM direct-detection optical OFDM based on block-wise signal phase switching”, Optical Communication (ECOC 2013), European Conference and Exhibition on Optical Communication, London, 2013, pp. 1-3

26. A Li, D Che, X Chen, Q Hu, Y Wang, W Shieh, “61 Gbits/s direct-detection optical OFDM based on blockwise signal phase switching with signal-to-signal beat noise cancellation”, Optics letters, 2013

27. X Chen, A Li, D Che, Q Hu, Y Wang, J He, W Shieh, “Block-wise phase switching for double-sideband direct detected optical OFDM signals”, Optics express 21 (11), 13436-13441

28. C Xi, A Li, D Che, Q Hu, Y Wang, J He, W Shieh, “High-speed fading-free direct detection for double-sideband OFDM signal via block-wise phase switching”, Optical Fiber Communication Conference, PDP5B. 7

29. X Chen, A Li, Q Hu, J He, D Che, Y Wang, W Shieh, “Demonstration of direct detected optical OFDM signals via block-wise phase switching”, Journal of Lightwave Technology 32 (4), 722-728

2 Literature Review

2.1 Introduction

Humans have continuously devised new technologies for communication. Thus, many forms of increasingly complex communication systems have appeared over the long history of civilization. The basic motivations behind each one are either to improve the transmission fidelity so that fewer errors occur in the received message, or to increase the transmission capacity of a communication link so that more information could be sent, or to increase the transmission distance so that messages can be sent farther without the need to restore the signal fidelity periodically along its path.

Prior to the nineteenth century, all communication systems operated at a very low information rate and involved only optical or acoustical means, such as signaling lamps or horns. One of the earliest known optical transmission links, for example, was the use of a fire signal by the Greeks in the eighth century B.C. for sending alarms, calling for help, or announcements of certain events [18]. Improvements of these systems were not pursued very actively because of technological limitations at the time. Thus it turned out to be faster, more efficient, and more dependable to send messages by a courier over the road networks.

The invention of the telegraph by Samuel F. B. Morse in 1838 ushered in a new epoch in communications—the era of electrical communications. In the ensuing years increasingly sophisticated electrical communication systems with progressively larger information capacities were developed. This activity led to the birth of free-space radio, television, microwave, and satellite links, and high-capacity terrestrial and undersea wire lines for sending voice and data to virtually anywhere in the world.

However, since the physical characteristics of both free-space and electric wire-based communication systems impose an upper bound on the transmission

capacities, alternative transmission media were investigated. A natural extension was the use of optical links. In 1969, Charles K. Kao with M.W. Jones measured the intrinsic loss of bulk-fused silica at 4 dB/km, which is the first evidence of ultra-transparent glass and awarded the 2009 Nobel Prize in Physics [19]. After extensive research and development on the needed electro-optical components, optical fiber communication systems started to appear in the 1970s. It is this technology that the thesis addresses.

In this chapter, we first review the receiver for optical communication systems, including coherent detection receiver and direct detection receiver. Principle and system architecture for each scheme is reviewed respectively. The motivation of the frequency response characterization is also illustrated. Then, we review the principle, the system configuration, and the development of space-division-multiplexing (SDM) for ultra-high-capacity optical transmission. Finally, we review recent development in fiber optic sensor (FOS) technology and the potential to use FMFs as in-line FOSs.

2.2 The receiver for optical communication systems

Since its introduction nearly two decades ago, optical fiber has become the preferred medium for high-throughput point-to-point digital communications. The primary advantages of optical fiber are its large bandwidth, low attenuation, immunity to interference, and high security. There are four distinct generations of fiber-optic transmission systems [20-24]; each new generation overcame a limitation of its predecessor.

The first generation, deployed in the 1970‘s, uses MMFs at short wavelengths near 850 nm. First-generation systems suffer from three severe limitations: attenuation, chromatic dispersion (CD), and modal dispersion (MD). The attenuation of optical fiber, which limits the distance between transmitter and receiver, is about 2 dB/km for wavelengths near 850 nm. The dispersion of fiber, due to the different wavelengths in a light beam arriving at their destination at slightly different times, causes short rectangular pulses to spread temporally into long smooth pulses as they propagate, which limits the speed at which data can be transmitted. CD occurs

because light at different frequencies travels through the fiber at different speeds. Similarly, multimode dispersion occurs because the different modes of light that can propagate down the large core of a MMF travel at different speeds.

Second-generation systems, introduced in the 1980‘s, avoid CD by operating at 1300 nm, the wavelength of minimum CD in fiber. In all silica-based optical fibers, minimum material dispersion occurs naturally at a wavelength of approximately 1300 nm, when material dispersion and waveguide dispersion cancel one another. A secondary advantage of 1300 nm is its lower attenuation, only 0.5dB/km. Again, this generation uses MMF, and thus still suffers from MD.

Third-generation systems came of age in the mid-I980’s, again operating at 1300 nm, but this time through SMFs; the core radius of a SMF is chosen small so that only a single mode can propagate. Hence, third-generation systems avoid MD as well, but still suffer from a transmission loss of about 0.5 dB/km.

The minimum attenuation of optical fiber, about 0.2 dBlkm, occurs for wavelengths between 1450 and 1650 nm. To exploit this immense low-loss bandwidth of over 25 000 GHz, fourth-generation systems shifted operation up to 1500 nm. However, there is a significant amount of chromatic disperison at these wavelengths, so only spectrally pure lasers - single-frequency lasers with a single longitudinal mode - can be used.

The modulation/demodulation scheme used by the four generations of transmission systems mentioned above is called intensity-modulation/direct detection (IM/DD). Intensity modulation means that information is carried only by the intensity or power of the transmitted lightwave, not by its frequency or phase. The term direct detection refers to the receiver configuration, where the received signal is applied directly to a photodetector. An important performance measure for optical receivers is the receiver sensitivity, measured by the number of detected photons per bit (at peak power). Practical IM/DD systems, although easy to implement, have poor sensitivity.

The quest for better performance in optical receivers has spurred the recent surge of interest in coherent detection — the fifth generation. There are two fundamental advantages of coherent receivers over direct detection receivers; first, they are more sensitive [19, 23-25]. This increased receiver sensitivity allows, for example, an increase in repeater spacing in long-haul point-to-point applications. Second, coherent receivers are more selective; they are better able to select one channel from a frequency-division multiplexed signal [26-28]; they can perform channel selection in the electrical domain using sharp digital filters, unlike direct detection receivers, which are forced to use broad optical filters. The selectivity promised by coherent receivers is key to exploiting the immense bandwidth of optical fiber.

2.2.1 Coherent detection receiver of optical digital transmission

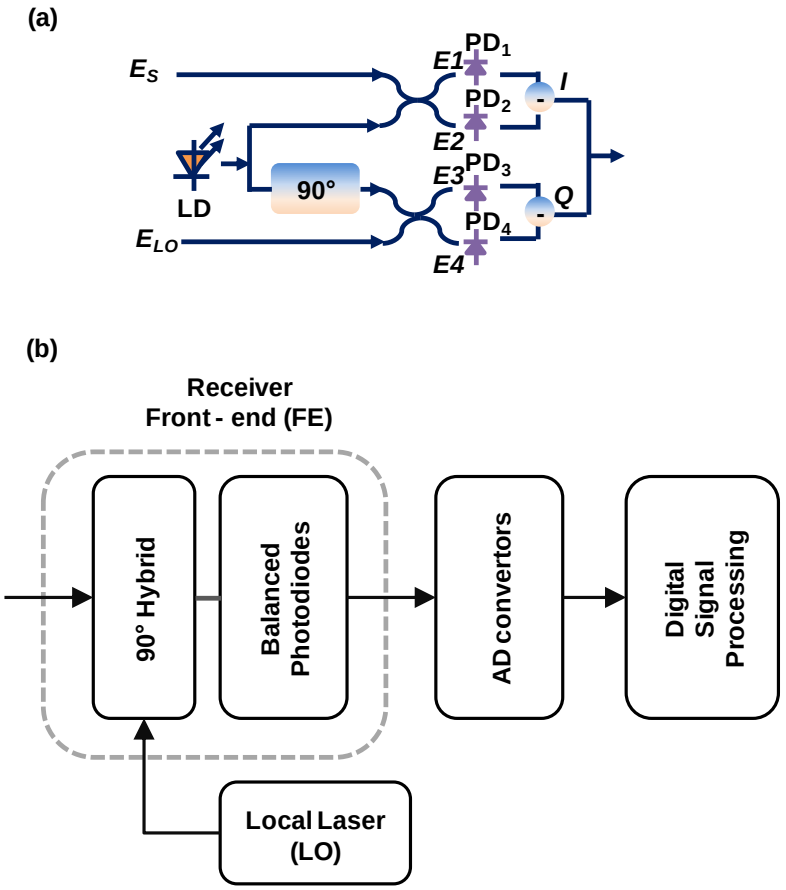

Fig. 2.1. (a) Coherent receiver composed by an optical 90º hybrids and two pairs of balanced photodiodes. (b) Different subsystems of a digital coherent optical receiver [29].

In this section, we review some of the basic principles of optical communications. In particular, we review the basics of coherent detection and its receiver structure. The coherent receiver can be used to detect the optical field, including its intensity, phase and polarization, with the help of local oscillator (LO). Based on where the LO frequency is placed, coherent receiver can be divided into two categories, the homodyne receiver and heterodyne receiver.

The homodyne receiver recovers the real and imaginary parts of the signal in parallel, and therefore needs twice as many photodetectors (PDs) as in the heterodyne receiver. In contrast, the heterodyne receiver needs an image rejection filter to recover the real and imaginary parts, and therefore requires twice the bandwidth as required in the homodyne receiver.

The conceptual diagram of a coherent receiver is shown in Fig. 2.1, which consists of a 6-port 90° optical hybrid, and a pair of balanced PD [30, 31]. The received optical signal is mixed with the LO in 90° optical hybrid, generating a 180° phase shift between the two branches for the balanced PD, and a 90° phase shift between the *I* and *Q* components [32, 33]. Denoting the input signal and LO as E_s and E_{LO}, the four outputs of the 90° optical hybrid are $E_1 = \frac{1}{\sqrt{2}}[E_s + E_{LO}]$, $E_2 = \frac{1}{\sqrt{2}}[E_s - E_{LO}]$, $E_3 = \frac{1}{\sqrt{2}}[E_s - jE_{LO}]$ and $E_4 = \frac{1}{\sqrt{2}}[E_s + jE_{LO}]$. The PD takes square operation for the optical signal. Thus, the output photocurrents of PD1 and PD2, I_1 and I_2, are

$$I_1 = \frac{1}{2}\left\{|E_s|^2 + |E_{LO}|^2 + 2\,\mathrm{Re}\left\{E_s E_{LO}^*\right\}\right\} \tag{2.1}$$

$$I_2 = \frac{1}{2}\left\{|E_s|^2 + |E_{LO}|^2 - 2\,\mathrm{Re}\left\{E_s E_{LO}^*\right\}\right\} \tag{2.2}$$

Considering the amplified spontaneous emission (ASE) noise of the optical signal and the relative intensity noise (RIN) of the LO source, we can write the intensity of the signal and LO, $|E_s|^2$ and $|E_{LO}|^2$, as

$$|E_s|^2 = |E_r|^2 + |n_o|^2 + 2\,\mathrm{Re}\left\{E_r n_o^*\right\} \tag{2.3}$$

$$\left|E_{LO}\right|^2 = I_{LO}\left(1+I_{RIN}\left(t\right)\right) \tag{2.4}$$

where E_r is the received signal with on ASE noise, n_o is the ASE noise, I_{LO} is the average power of LO and I_{RIN} is the RIN of LO. The balanced PD subtracts the photocurrents obtained from the two PDs, and provides us

$$I_I\left(t\right) = I_1 - I_2 = 2\,\mathrm{Re}\left\{E_s E_{LO}^*\right\} \tag{2.5}$$

. The square terms in Eqs. (2.1) and (2.2) are cancelled during the subtraction operation, suppressing the impact from ASE noise and RIN. From the left term, the *I* component of the signal is recovered, giving the real part of the beating term. Similarly, the *Q* component is recovered by another pair of PDs, PD3 and PD4. Combining the *I* and *Q* components, the constructed complex signal is the replica of the optical field with frequency down-shifted by the LO.

In a digital coherent receiver, there are three key subsystems as shown in Fig. 2.1(b):

1) Optical front-end, which linearly maps the optical field into a set of electrical signals.
2) Analog-to-digital converter (ADC), which converts from the electrical signals into a set of discrete-time-quantized signals at the sampling rate.
3) Digital demodulator, which converts the digital samples into a set of signals at the symbol rate.

Coherent detection represents the ultimate performance in receiver sensitivity, spectral efficiency. The advantages are twofold: (1) the linear down-conversion of the received optical signal, and (2) the suppressing of the common mode noise. Together with the *I*/*Q* modulator, the coherent detection, leads to a linear channel, where complex signal can be transmitted and processed easily using DSP.

2.2.2 Direct detection receiver of optical digital transmission

In this section, we review some of the basics of direct detection and its receiver structure. Direct-modulation/direct detection (DM/DD) is the simplest DD scheme [34-36]. Since the CD introduces severe nonlinear distortion to the signal due to the square-law photo-detection, the transmission distance of DM/DD is limited to tens of kilometers. Furthermore, the phase and polarization dimensions are not utilized by DM/DD, leading to low electrical SE.

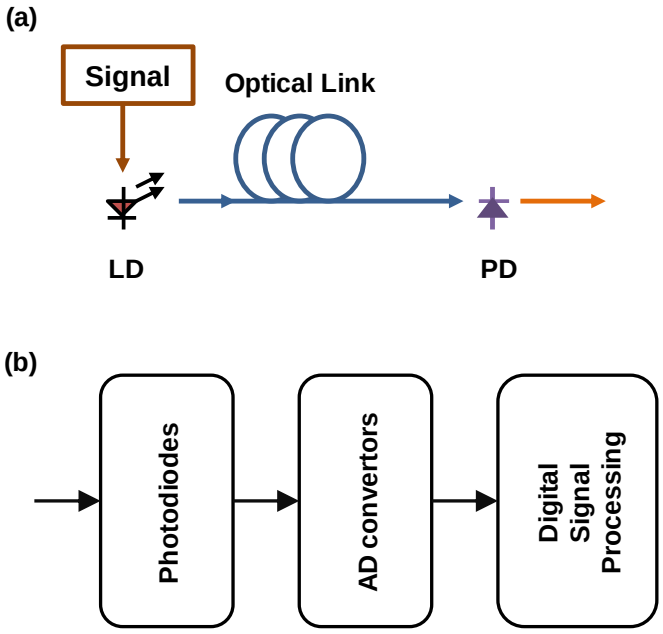

Fig. 2.2. (a) Conceptual diagram of a conventional DD system. (b) Different subsystems of a digital direct optical receiver

Conventional DD, referring to DM/DD, has the merits of simple implementation and low cost. As shown in Fig. 2.2, DM/DD modulates the non-negative signal directly onto a laser, and converts it to the photocurrent by a single-ended PD at the receiver [36].

2.2.3 Frequency response of a receiver

To support the transmission of hundreds of kilometers, a linear channel is needed where linear mapping can be obtained between the baseband and optical signal. For the high-performance short-reach optical networks, we aim to find promising solutions which can achieve a linear channel in a cost efficient way. By using coherent detection, the channel response can be compensated by DSP. However,

characterization of each individual optoelectronic component is still critically important, especially for direct detection. In direct detection, the channel is nonlinear, and thus separation of the optical channel and radio frequency (RF) channel is essential to remove the photodiode nonlinearity arising from its square-law detection [37]. Consequently, it is necessary to calibrate both amplitude and phase response of individual optoelectronic components.

Usually, a calibrated electrical vector net-work analyzer (VNA), modulated optical source, and calibrated optical reference receiver are used to accurately measure the frequency response of a large class of optoelectronic devices including Mach–Zehnder modulators, electro-absorption modulators, directly modulated semiconductor lasers, and linear optical receivers. Although this type of measurement system is commonly used in the optoelectronics, the theories behind the measurements and the procedures and restrictions necessary for accurate calibration are not generally well known. Indeed, these methods are only applicable to obtaining amplitude response, incapable of detecting phase response [38-41].

2.3 Space-Division-Multiplexing for communications

The capacity of the optical networks has witnessed a huge growth during the last few decades, due to the exploration of the advanced optical communication technologies. To sustain the capacity increase, various multiplexing techniques have been intensely investigated to make full utilization of the available modulation freedoms in fiber channels. Nowadays, commercial coherent optical transmissions are able to multiplex the signal in dimensions of time, wavelength, phase and polarization, in order to pack up more information into a single fiber [42-50]. Using the multiplexing techniques, the optical system achieves a higher data rate with reduced cost per bit, making the multiplexing scheme a favorable choice when upgrading the capacity. With the development of various multiplexing technologies, the available freedom in SMF has been maximally explored. As a result, the capacity of SMF is approaching its fundamental limit quickly [49]. To keep up with the increasing demand of data traffic, one option is to install new fibers to transmit more information through parallel channels. The cost will increase linearly with the

capacity using parallel channels. The increased cost will undoubtedly put a pressure on the capacity growth in the future.

Another option is to find a new dimension for the signal multiplexing. SDM uses the spatial mode as an additional degree of modulation freedom, sustaining a constant growth of the channel capacity [51-57].

2.3.1 Fundamentals of few-mode fiber

The guided modes in an optical fiber are referred to the modes that can be well-confined in the core area, and propagate for a long distance with low loss. The mode condition in a fiber is usually described by the normalized frequency parameter, which is also called as *V*-number [58-60]. The *V*-number is defined as

$$V = k_0 a \sqrt{n_1^2 - n_1^2} \tag{2.6}$$

where n_1 and n_2 are the refractive indexes of the core and cladding layers, a is the radius of the core, $k_0 = 2\pi / \lambda$ is the wave-number, and λ is the wavelength of the optical signal. For a step-index fiber with a *V*-number smaller than 2.405, only one guided mode is supported in the fiber. When the core is enlarged, the *V*-number increases as well. The channel capacity is enlarged by *N* times when *N* guided modes are propagated in the fiber. To recover the modes after the random mode coupling during the propagation, 2*N* by 2*N* MIMO DSP is needed at the receiver where the factor of 2 accounts for polarization degeneracy. To control the DSP complexity to a manageable level, FMF has been proposed, leading to a small mode number. The simplest case of FMF is two-mode fiber (TMF), which has a *V*-number above single-mode condition but below three-mode condition, 2.4<V<3.8. TMF supports the propagation of two spatial modes, LP_{01} and LP_{11}. Since LP_{11} mode includes two orthogonal spatial modes, LP_{11a} and LP_{11b}, a TMF actually supports the propagation of 6 modes, considering the two polarization modes for each spatial mode [10-13]. By exciting all 6 modes, the channel capacity can be improved by 3 times compared to the SMF transmission.

The Ge-doped TMF used in our lab [1, 15-17] has a step-index profile with a core diameter of 11.9 μm and refractive index step of 5.4×10^{-3}. The *V*-number of the TMF is calculated to be 3.62, which fits into the two-mode condition, $2.4<V<3.8$. The CD of LP_{11} mode is measured to be 17 ps/nm·km, which is similar to that of the SMF, while the CD of LP_{01} mode is measured to be 22.1 ps/nm·km, slightly higher than the SMF. With the fiber parameters, the modal index is simulated for different wavelength. As shown in Fig. 2.3, three spatial modes are supported in the transmission window around 1550 nm, including the fundamental mode LP_{01}, and two degenerate modes, LP_{11a}, LP_{11b}. The degenerate mode LP_{11} is cut off at the wavelength of 2323 nm, so the fiber can be used as a SMF above the wavelength of 2323 nm. Great difference in the effective refractive index is observed between the modes, LP_{01} and LP_{11}. As a result, the two modes are subject to a small mode coupling and a large modal dispersion (MD) of 3 ps/m. The loss of the fiber is measured to be 0.26 dB/km.

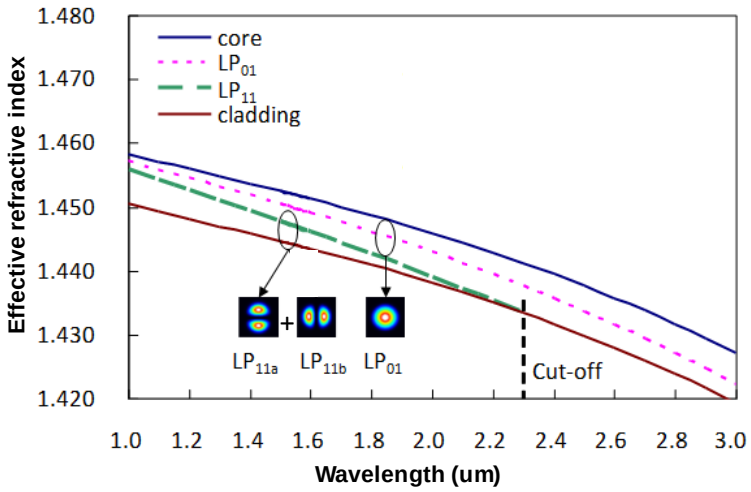

Fig. 2.3. The modal index of the TMF vs. wavelength.

2.3.2 Mode multiplexing/demultiplexing components

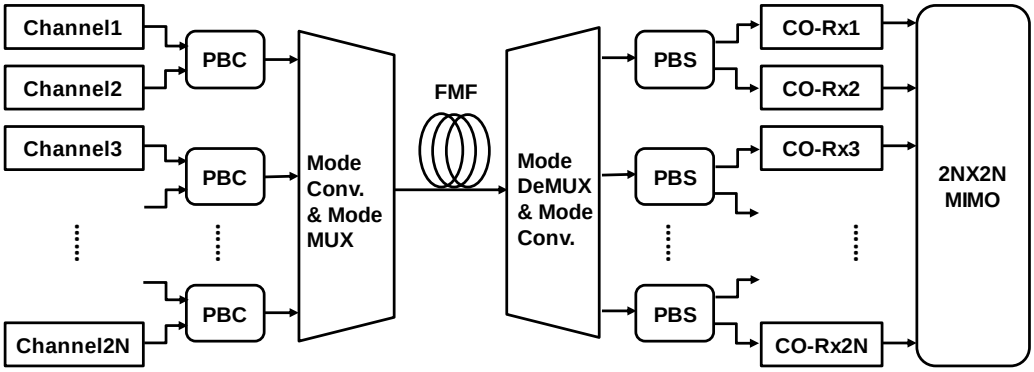

Fig. 2.4. Schematic diagram of FMF transmission.

For a FMF with *N* spatial modes, a total of 2*N* modes can be used for signal transmission, considering two polarization modes in each spatial mode. Fig. 2.4 shows the schematic diagram of the FMF transmission [15-17]. The transmitted signals are generated with 2*N* transmitters as signals for 2*N* independent channels. The two polarization modes are first combined using polarization beam combiner (PBC). Then, the signals are converted to the corresponding spatial modes and combined using a mode multiplexer before launched into the FMF. After the transmission, the spatial modes are separated using a mode demultiplexer, and the high-order spatial modes are converted back to the fundamental mode. The polarization modes are separated by the polarization beam splitter (PBS), followed by coherent receivers to detect the signal in each mode. 2*N*x2*N* MIMO DSP is used to compensate the linear channel impairments, and recover the signals [14]. High-performance mode converter and mode multiplexing/demultiplexing (MUX/DEMUX) device are the critical components in a FMF transmission system. Mode converter can be obtained using different materials and structures, such as long-period fiber grating (LPFG), spatial light modulator (SLM), free-space phase plate, or fused spatial mode coupler (SMC). LPFG based mode MUX/DEMUX and SLM based MUX/DEMUX will be reviewed in the following.

2.3.2.1 Long-period fiber grating based mode multiplexer/ mode demultiplexer

Fig. 2.5 shows the free-space based setup to convert and multiplex modes in a TMF. The transmitter generates the signal in fundamental mode. To convert the

fundamental mode to a higher-order mode, SMF is spliced with TMF to transfer the power into TMF. A mode striper is then used to strip out the higher-order mode in TMF, leaving fundamental mode in the fiber. After that, mode converter is used to convert the fundamental mode into desired mode, LP_{11}. Modes LP_{11a} and LP_{11b} are combined together using a mode combiner. The mode combiner is carefully aligned to reduce the insertion loss (IL) and launch the signal into the correct mode of the transmission fiber. The mode demultiplexing and conversion at the receiver side can be achieved using a setup constructed in a reverse order of Fig. 2.5. The mode striper, mode converter and mode combiner are discussed in detail below.

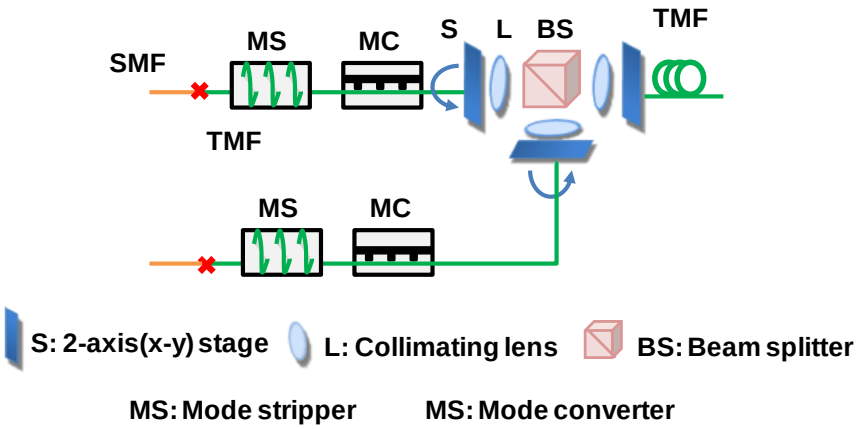

Fig. 2.5. LPFG based mode conversion and multiplexing setup.

❖ *Mode striper*

Mode striper is fabricated based on the mechanism of macro-bending [61]. By tightly winding the TMF around a post with diameter of 8 mm for more than 20 turns, the higher-order mode, such as LP_{11} mode, experiences a huge attenuation, while the attenuation for the fundamental mode, LP_{01}, is smaller than 0.2 dB. A rejection ratio higher than 30 dB is obtained for LP_{11} mode. Therefore, the LP_{11} mode is stripped out, leaving only the LP_{01} mode.

❖ *Mode converter*

In this section, we describe a LPFG based mode converter, where a grating structure is built in the fiber. Resonant coupling is induced between two spatial modes when the grating pitch Λ equals to the beating length of the two modes [62-63]. We use

the TMF mentioned in Section 2.3.1 to build a mode converter for modes LP_{01} and LP_{11} modes. A metal grating with evenly-spaced grooves is pressed against the TMF, leading to the deformation of the fiber core. Therefore, the LPFG is built in the fiber. In order to decide the groove pitch for the metal grating, we measured the MD of the TMF. The beating length for modes LP_{01} and LP_{11} is expressed as [11-13]

$$L_B = 2\pi / (\beta_{01} - \beta_{11}) \tag{2.7}$$

where β_{01} and β_{11} are the propagation constants of modes LP_{01} and LP_{11}. With the MD of 3 ns/km, the mode beating length is calculated to be 524 μm, which corresponds to the groove pitch for the metal grating. The core deformation has an s-bend arc shape. With the core deformation radius of 0.2 μm, the coupling length of 8.1 mm is needed for the mode converter to achieve its maximum coupling efficiency. An extinction ratio over 20 dB is measured around the wavelength of 1550 nm for wavelength range more than 10 nm. The metal grating and TMF are mounted on a 3-axis stage to adjust the angle and pressure applied between the metal grating and fiber. After careful adjustment, we achieve the maximum extinction ratio at the wavelength of 1550 nm.

❖ *Mode combiner*

Fig. 2.6 shows a free-space based mode combiner to combine three spatial modes, LP_{11a}, LP_{11b} and LP_{01}. The combiner consists of three XY translation stages, two 50:50 beam splitters and four collimating lenses. The three XY translation stages are connected to the input fiber, through which the modes LP_{11a}, LP_{11b} and LP_{01} are launched into the setup. The fiber ends are connected with FC type adapters. The orientations of the LP_{11a} and LP_{11b} modes are adjusted to be orthogonal to each other by rotating the fiber adapters axially. The input modes are then collimated to a spot size of 2 mm by the three collimating lenses with numerical aperture NA of 0.25 and effective focal length f of 11.0 mm. The collimated beams pass through the beam splitters in either transmission or reflection direction, and arrive at the output collimator. The beam spot is focused by the output collimator and launched into the core of the output fiber. To achieve the maximum coupling ratio, the three input XY

translation stages are carefully aligned to put the beam spots to the correct position. The free-space beam combiner is polarization insensitive. The minimum loss is 3 dB for the LP_{01} mode, and 6 dB for the LP_{11} modes. The setup can also be used as mode splitter by exchanging the input and output.

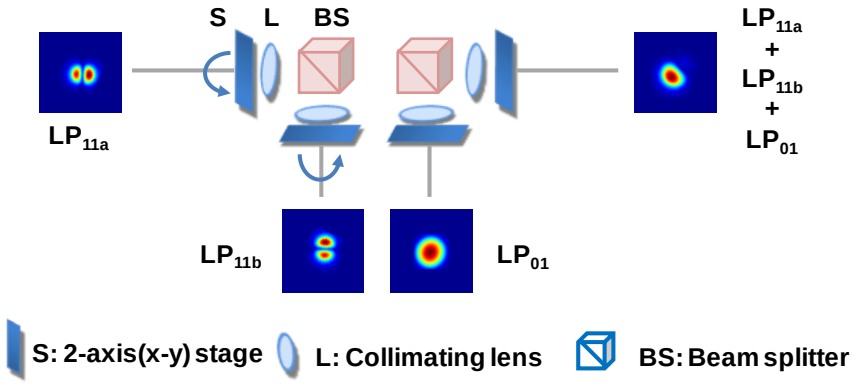

Fig. 2.6. Mode combiner for three spatial modes LP_{11a}, LP_{11b} and LP_{01}.

2.3.2.2 Spatial light modulator based mode multiplexer/ mode demultiplexer

❖ ***Introduction of SLM***

A SLM is a device that imposes spatially varying modulation onto a beam of light. A simple example is an overhead projector transparency. Usually when the phrase SLM is used, it means that the transparency can be controlled by a computer. In the 1980s, large SLMs were placed on overhead projectors to project computer monitor contents to the screen. Since then more modern projectors have been developed where the SLM is built inside the projector. These are commonly used in meetings of all kinds for presentations.

Usually, an SLM modulates the intensity of the light beam. However, it is also possible to produce devices that modulate the phase of the beam or both the intensity and the phase simultaneously. SLMs are used extensively in holographic data storage setups to encode information into a laser beam in exactly the same way as a transparency does for an overhead projector. They can also be used as part of a holographic display technology.

The Liquid Crystal-on-Silicon (LCOS) based SLM functions through controlling an active-matrix phase-only liquid-crystal display (LCD), working in reflective mode with 1920 X 1080 resolutions and a 0.7" diagonal. The signal is addressed via a standard digital visual interface (DVI) signal by a PC's graphics card. Basically the LCOS phase display works like an extended monitor, were all phase function (gratings, phase masks, holograms, etc.) are addressed via DVI. Via the RS-232 interface and with the provided software, one is able to configure the modulator for different applications and wavelengths. The SLM used in our lab is the PLUTO-TELCO for common telecommunication wavelength, which ranges from 1520 - 1620 nm, as shown in Fig. 2.7. The parameters of the phase display are listed in the Table 2.1.

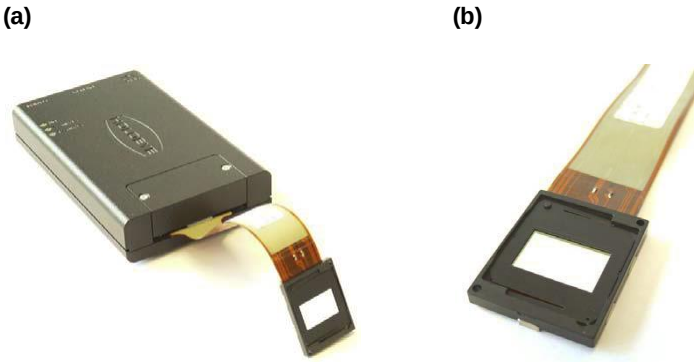

Fig. 2.7. (a) PLUTO phase modulator. (b) High-definition (HD) phase display

Table 2.1. Parameters for HD phase display

Parameter	Unit	Value
Type		LCOS (reflective), Active Matrix LCD
Mode		Nematic
Phase levels		256 (8-bit) grey levels
Active Area		15.36 mm x 8.64 mm
Nominal Resolution		1920 x 1080 pixels
Pixel Pitch	μm	8.0
Image Frame Rate	Hz	60
0th order intensity		60%
Illumination (max.)	W / cm²	~ 2
Operating temp.	°C	+10 to +70
Wavelength	nm	1520 - 1620

❖ *Phase Characterization of SLM*

The modulator of the SLM (HOLOEYE, HED600-L) is a 'Liquid Crystal' that is optically active and changes the phase of reflected light by applying an electric field. By

programming and applying different electric voltage onto each pixel of the 'Liquid Crystal' phase display, different spatial phase patterns can therefore be modulated on the input signal beam. To apply different electric voltage onto each pixel of the phase display, greyscale image is programmed and addressed on the phase display by using the supplied Pattern Generator software (or the SLM Slideshow Player software or standard image viewer software). For the greyscale image, the grey level indicates the brightness of a pixel and each gray level also indicates a corresponding electric voltage value. The minimum grey level is 0. The maximum grey level depends on the digitisation depth of the image, and for the TELCO, it is 255. In other words, in the greyscale image displayed on the phase display, a pixel can take on any value between 0 and 255.

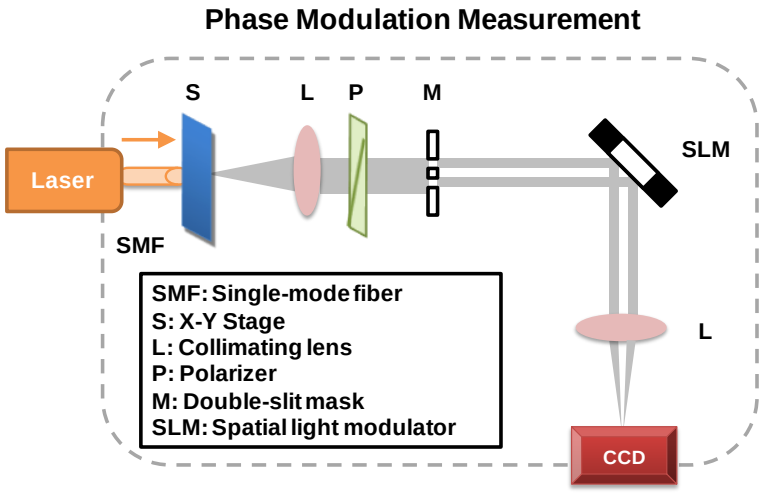

Fig. 2.8. Experimental setup for phase modulation measurements.

Each SLM has its own properties and specifications, and therefore, the phase modulation of the phase display needs to be characterized before using. That is to say, the relationship between the gray level and the phase retardation modulated onto the reflected light needs to be characterized. The phase modulation characterization is obtained with two-beam interference setup shown in Fig. 2.8. It is noted that the incident polarization for phase only modulation should be kept along the long display axis (parallel to the longer axis of the phase display).

For the measurement, we characterize the curve of phase retardation vs. gray level and is shown in Fig. 2.9. The TELCO is optimized for applications with typical

telecommunication wavelengths. The anti-reflective (AR) coating assures a front reflection of less than 0.5% between 1520 and 1620nm. The TELCO enables 2π phase retardation up to ~1600nm.

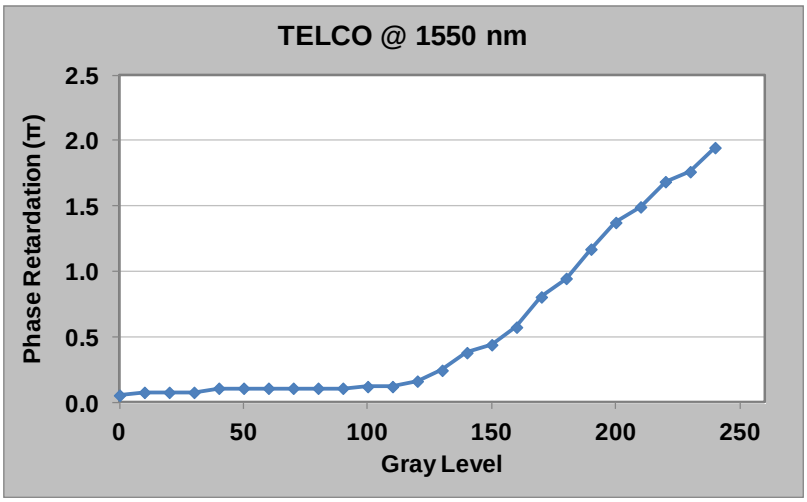

Fig. 2.9. Phase measurements @ 1550nm with PLUTO-TELCO.

❖ *SLM for Space-Division-Multiplexing (SDM)*

SLMs have the ability to manipulate the phase front of a beam with high resolution in a reconfigurable way. It can be used in the context of mode division multiplexing (MDM) transmission experiments as the mode multiplexer/demultiplexer [64-65], and/or to perform processing such as optical MIMO [64] as well as switching [65-67]. In a laboratory setting, the reconfigurable and flexible nature of the SLM also makes it useful as a means of rapid testing and prototyping. Unlike other multiplexing methods such as using phase plates [68], offset spots [69] or photonic lanterns [70] which are designed and optimized for particular type of fiber, an SLM based system is not bound to any particular fiber type or multiplexing method (LP, orbital angular momentum (OAM), offset spots, etc.). It can be reprogrammed to launch and receive in any basis within the NA of the optical system itself. The ability of the SLM-based system to align itself and compensate for aberrations [71] allows it to achieve better performance using off-the-shelf components whilst maintaining a compact size and high degree of automation.

Fig. 2.10 illustrates an SLM based mode multiplexer/demultiplexer which would be installed at either end of the fiber under test (FUT). When operating as a mode multiplexer, Gaussian beams from the SMF array for each channel are incident on the SLM at different angles after passing through some polarization diversity optics, which is required to align the incoming polarization of the beam with the polarization required for the liquid crystals of the SLM. The phase mask programmed onto the surface of the SLM forms the modes for the different channels at different angles such that each SMF in the array excites the desired mode for that channel on the core of the FUT. The principle is similar to the traditional phase mask and beamsplitter approach [68] except the SLM is performing the function of both the correlation filter and the beamsplitter.

The primary advantage of SLM-based approach is the compactness and flexibility. For example, assuming there are sufficient fibers in the SMF array, the number of channels can be changed without installing/removing bulk optic beamsplitters and phase masks. The system is also not tied to any particular fiber or basis and can emulate different launch conditions.

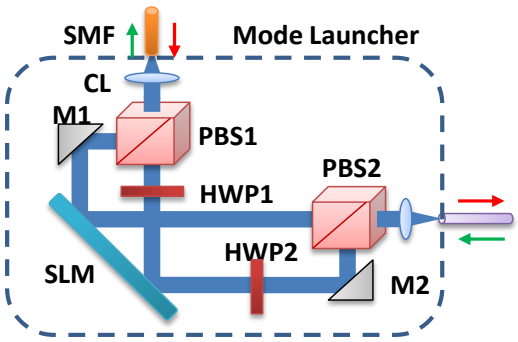

Fig. 2.10. SLM based mode multiplexer/demultiplexer. SMF: Single-mode fiber, CL: Collimating lens, M1/M2: Turning mirror, PBS1/PBS2: Polarizing beam splitter, HWP1/HWP2: Half-wave plate, SLM: Spatial light modulator.

2.3.2.3 Mode multiplexer/ mode demultiplexer summery

The properties for different mode multiplexers/ mode demultiplexers are compared and summarized in the flowing Table.

Table 2.2 Mode multiplexer summery

Mode multiplexer	Insertion loss (IL)	Mode dependent loss (MDL)	Bulk size
LPFG based	0.4 ~ 1.5 dB	Large incease with the number of modes	Large
SLM based	4.5 ~ 5.2 dB	Steady incease with the number of modes	Small
Offset launch	NA	Large incease with the number of modes	Large

2.3.3 Ultra-high-capacity optical transmission in few-mode fibers

SDM has been widely adopted in wireless communications, usually in combination with code/time/frequency division multiplexing (CDM/TDM/FDM). The multipath propagation in SDM system results in multipath fading, inter symbol interference (ISI) and inter-channel interference (ICI), which needs to be dealt with for minimum penalty. OFDM is an efficient modulation scheme for mitigating the effects of multipath channel with excellent transmission performance since the ISI can be eliminated through insertion of CP.

In optical communications, SDM can be achieved through either a MCF or a MMF. The different spatial modes can be treated as independent channels to transmit the signal simultaneously. Compared to the parallel channels, SDM can increase the channel capacity in a cost efficient way. The fiber capacity is greatly increased with different spatial modes closely packed in one fiber link. Meanwhile, the cost per bit is significantly reduced, since the cost of cable and its installation is reduced by the large capacity. A huge amount of effort has been devoted to develop the enabling technologies for the SDM transmission. With the innovations of the high-performance MMFs, MUX/DEMUX components, SDM has become a promising solution for the high-capacity transmission [72-74].

The crosstalk between the different spatial modes is an important issue in SDM system [75]. Coherent transmission provides a solution for overcome this problem by using MIMO signal processing. Similar to the polarization mode dispersion (PMD) in SMF which can be compensated using 2x2 MIMO with coherent transmission, the

MD in MMF can be compensated by 2*N*x2*N* MIMO, where *N* is the number of spatial modes supported in fiber [76-81].

The FMF channel can be described by a channel matrix, which plays a critical role in receiver design and determines the ultimate performance of the FMF system. An in-depth understanding of the statistical properties of fiber channel subject to DMD is essential to assist the system design and achieve an optimal system performance.

Beside the mode MUX/DEMUX components, few-mode amplifier for FMF transmission is also very important if there is significant fiber link loss. The loss could come from the mode MUX/DEMUX or fiber loss. The feasibility of few-mode amplification using Erbium-doped fiber amplifier (EDFA) or Raman pump has recently been demonstrated [82-85] with the inclusion of aforementioned mode convertors. FMF compatible EDFA opens an avenue for the long-haul FMF transmission [82-83, 85-86]. As is well known, the nonlinear effects in silica fiber impose a hard constraint on the achievable channel capacity. For FMF based transmission, there is strong field overlapping between different modes, thus it is important to analyze the FMF systems taking into account potential inter-modal nonlinearity [87]. There have already been many theoretical studies on the nonlinear propagation modeling and simulation of FMF based transmission systems [87-88], and also some work [89] have shown the experimental characterization of nonlinear parameters in a FMF. Some other work also proposed a method to mitigate the nonlinear noise on subsystem level, namely using symbol-rate optimized multi-carrier formats [90-94] which could fit well for future Terabit/s SDM superchannel transmission.

2.4 Space-Division-Multiplexing for sensors

Almost forty years have passed since the study of optical fiber sensors began. Various ideas have been proposed and various techniques have been developed for various measurands and applications. To date, various types of FOSs have been commercialized, but it is also true that, among a myriad of techniques that have been studied, only a limited number of techniques and applications have been

commercially successful. However, in many fields of application, FOSs have to compete with other rather mature technologies such as electronic measurements. To appeal to users already accustomed to other mature technologies, the superiority of FOSs over other techniques needs to be clearly demonstrated. Typical users are not interested in specific techniques involved in measurement. They simply desire sensor systems having good performances with reasonable price except for very special uses. Hence, FOS systems should be designed in the form of complete systems including detecting and signal-processing electronics. In some cases such as electric protection relaying systems, the sensor systems are simply subsystems of rather larger systems. In some cases such as optical gyroscopes and optical current sensors, FOSs compete with other optical bulk sensors as well. Even with these difficulties, considerable efforts have been made to study of FOSs, and some of them are now approaching maturity.

2.4.1 Recent developments in fiber optic sensor technology

2.4.1.1 Fiber optic sensor principles

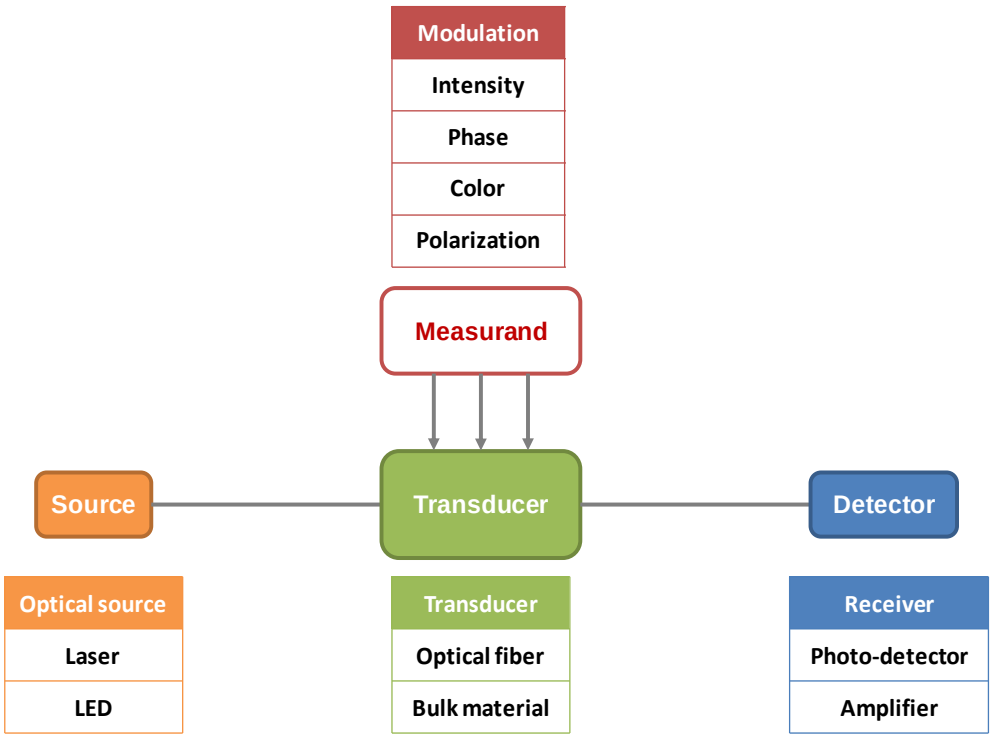

Fig. 2.11. Basic elements of an optical fiber sensor system.

The general structure of an optical fiber sensor system is shown in Fig. 2.11 which is mainly composed of four components including source, measurand, transducer and detector. In more details, optical fiber as transducer can be either single or multimode; an optical detector and actuating circuitry could be processing electronics, oscilloscope, optical spectrum analyzer etc. In an FOS, the optical parameters that can be modulated are the amplitude, phase, color (or wavelength), and state of polarization [95-96]. The optical modulation methods of the sensors involve the following.

- ***Intensity-modulated sensors***

The variation of the light intensity that is proportional to the perturbing environmental parameters can be detected by sensors. The concepts associated with intensity modulation include transmission, reflection, and micro bending. For this, a reflective or transmissive target can be incorporated in the fiber. Other mechanisms that can be used independently or in conjunction with the above three primary concepts include absorption, scattering, fluorescence, and polarization. Intensity modulated sensors normally require more light to function than phase modulated sensors; as a result, they employ large core multimode fibers or bundles of fibers.

- ***Phase-modulated sensors***

The phase of the light in a sensing fiber is compared with a reference fiber in a device known as an interferometer. These sensors employ a coherent laser light source and two SMFs. The light is split and injected into the reference and sensing fibers. If the light in the sensing fiber is exposed to the perturbing environment, a phase shift occurs between them. The phase shift is detected by the interferometer. Phase modulated sensors are much more accurate than intensity-modulated sensors.

2.4.1.2 Optical fiber sensors' advantages over traditional sensors

The advance in research and development of FOS devices has spread their applications to various fields of technology, such as medical, chemical, and

telecommunications industries. They have been developed to work on a wide variety of physical properties, such as temperature, chemical changes, electric and magnetic fields, vibrations, strain, displacement (position), flow, pressure, rotation, radiation, liquid level, light intensity, and color. For performance in harsh environments, FOS proves more reliable and rigid than conventional electronic sensors where they meet difficulties [95, 97-98].

Optical fiber sensors exhibit a number of advantages over other types of sensors: (1) small sensor size; (2) non-electrical; (3) sensitivity to multiple environmental parameters; (4) requiring small cable sizes and weights; (5) permitting remote sensing; (6) allowing access into normally inaccessible areas; (7) often no need for physical contact; (8) immunity to radio frequency interference (RFI) and electromagnetic interference (EMI); (9) no contamination to their surroundings and are not subject to corrosion; (10) high sensitivity, resolution and dynamic range; (11) ease interface with data communication systems.

2.4.1.3 Optical fiber sensing applications

Under harsh environmental condition and when sensing over long distances, optical sensing is considered as the ideal solution for the applications where conventional electrical sensors such as foil strain gages, thermocouples, and vibrating wires have proven ineffective or difficult to use.

❖ *Medical field*

Optical-chemical and biochemical sensing is being researched extensively around the world, and these sensors are finding an increasing number of applications in medicine, biomedicine, and chemical analysis [99]. The main physical phenomena exploited for optical chemical sensing are absorption and fluorescence, although chemical luminescence, Raman scattering, and Plasmon resonance have also been used. Health-care is unquestionably the application field which seems to have the most potential for future development [100-101]. Optical biosensors are finding ever-increasing applications in different branches of medicine.

❖ *Energy field*

Fiber Bragg grating (FBG) optical sensing has unique attributes that make it suitable for traditionally difficult applications. For example, monitoring the structural integrity of a wind turbine blade with electrical sensors would often result in noisy measurements because of long copper lead wires. With optical sensing, accurate and noise-free strain measurements on wind turbine blades are possible with little added weight to the structure. Furthermore, the nonconductive and distributed nature of optical fibers lends well for many uses in oil and gas applications, including pipeline monitoring and downhole monitoring. Applications of energy FOS devices are wind turbine blade monitoring, pipeline monitoring, power line monitoring, offshore platform monitoring and downhole monitoring.

❖ *Civil field*

Structural health monitoring systems based on electrical sensors often face significant environmental challenges. An electrical monitoring system would require the installation of countless wires, a lightning grounding system, periodic external calibration, and the potential maintenance of corroded and/or degrading sensors. With an optical sensing solution, these downfalls are all eliminated. The ability to daisy chain multiple sensors on a single fiber greatly reduces the weight and complexity of the system. Furthermore, optical fiber does not corrode or conduct like copper wire, which increases longevity and reduces the risk of damage due to lightning. Applications of civil FOS devices are large building monitoring, bridge and road monitoring, airport landing strip load monitoring and dam monitoring.

❖ *Transportation field*

To ensure passenger safety, monitoring systems are increasingly deployed to ensure the proper operation of airplanes, railways, ships, and more. However, weight, size, and harsh environmental requirements can pose significant challenges to implementing an electrical monitoring system. FBG optical sensors alleviate these challenges by providing lightweight distributed sensor measurements that are immune to corrosion, high voltage, and EMI-induced noise. Also, because of the

longevity and ease of installation of FBG optical sensors and lack of need for external calibration, these sensing systems can be deployed reliably for decades without needing any maintenance; this is especially beneficial for long-term railway and ship hull monitoring. The ability to have multiple sensors on a single, very thin fiber dramatically reduces the weight of the monitoring system, which is especially important in aerospace applications. Applications of transportation FOS devices are railway monitoring, fuel tank monitoring, airplane wing monitoring, and ship hull monitoring [102].

2.4.2 Mode control in few-mode fibers

❖ *Mode selective excitation and extraction*

In mode-selective launches, only a subset of propagating modes is excited, in order to mitigate MD. Experiments on selective mode excitation include laser driving schemes [103-104], masks for spatially filtering [57, 105] and prism coupling [106-107].

Recent holographic optimization experiments demonstrate the agility of SLMs in mitigating the mode switching limitations of the static computer generated masks [105] and the pierced plates [57]. The incident electric field at the MMF input endface may be swiftly customized by changing the hologram using a computer. Furthermore, the rapid reconfiguration speed of the SLM allows for adaptive updating of the incident field on the MMF [108].

❖ *Mode stability*

Over the past years, several MUX/DEMUX techniques have been reported. These techniques include physically stressed fiber [109-110], spot couplers [111], photonic lanterns [52], 3D-waveguides [112], and spatial phase shaping of the optical profile with glass plates [113]. Alternatively to the above static mode shaping techniques, dynamic and adaptive SLMs, such as reflective LCoS devices can also be used for mode shaping [32–33]. Regarding the latter, mode multiplexers that shape the phase

but not the amplitude of the spatial optical profile to be coupled into the FMF have so far been used.

Some work also [114] investigates and experimentally demonstrates beam shaping of both phase and amplitude using LCoS modulator and discusses its relevance for coupling into higher-order modes of few-mode fibers. A practical approach is to use a phase-only modulator in combination with a spatial filter, consisting in its simplest form of a two-lens system with a pinhole located in between. The spatial filter converts spatial phase-modulation (PM) to spatial amplitude-modulation (AM) and thus generates complex light modulation if an adequate phase profile is used.

❖ *Mode amplifier*

SDM in principle allows up scaling of the capacity per fiber by a factor proportional to the number of cores or modes. However, operation of such schemes in existing long haul networks requires the development of suitable high performance in-line optical amplifiers. Recently a multi-core EDFA has been demonstrated with 4dB of gain variation between the cores at a net signal gain of 25dB [115].

Use of MMF is another attractive option, where each guided mode can in principle be used as an independent channel. Neng et. al. [84] have recently studied numerically the performance of a two-mode amplifier based on a uniformly doped step-index EDFA. They have shown that controlling the modal shape of the pump provides a means of tailoring the overall inter-modal gain. Besides experimentally studying the impact of using different modal pump fields, [82] also investigates the effect of tailoring the spatial refractive index in the EDFA. Using an optimized active fiber profile, over 22 dB of small signal gain for both LP_{01} and LP_{11} modes and a relatively flat gain profile with a maximum gain variation of 3 dB across the full C-band for LP_{01} is realized.

2.4.3 In-Line fiber optic sensors in few-mode fibers

Fiber-optic interferometric sensors that measure strain, but are insensitive to temperature fluctuations, have been developed, and other application-specific sensors can be similarly designed [116-117]. The optimal use of a single-fiber sensor can be obtained if simultaneous measurement of strain and temperature is possible. A versatile FOS should be capable of performing more than one task simultaneously or different tasks at different times, with a single fiber. For example, a fiber sensor embedded in a composite laminate could be used as a temperature sensor during the cure of the composite and could act as a strain sensor during the lifetime of the composite structure. This would lead to a reduction in sensor size and a decrease in the number of components, as well as to the cost-effective implementation of fiber-optic sensors.

Two-core fiber sensors operated at two different wavelengths have been proposed to solve this problem [118]. In such a scheme, the variation of light intensity in each core is a function of strain and temperature and the operation at two wavelengths may allow, in principle, the discrimination between strain and temperature effects. The practical implementation, however, requires development of specialized two-core fibers with specific wavelength sensitivities. The use of two different wavelengths in a simple polarimetric sensing system can also be considered. However, the sensitivity of the sensor to strain and temperature at two close wavelengths does not differ by a significant amount. Also, the fiber should operate within its single-mode regime at both the wavelengths in consideration. Hence, the use of two distant wavelengths makes the fiber weakly guiding at the higher wavelength of operation.

To address above concerns, theoretical feasibility of a three mode fiber sensor using interference of LP_{11} and LP_{02} with fundamental mode LP_{01} has been demonstrated in [119]. The results obtained by fringe counting show that temperature influence could be eliminated by simultaneous detection of LP_{11}/LP_{01} and LP_{02}/LP_{01} interference. Spatial mode separation by matched filters would allow phase measurement techniques such as heterodyne or phase-shift interferometry [124], and then enhance the accuracy. If common fibers are used, some limitation is assigned to such a multimode interferometric sensor by birefringence: the

polarization variations must be slower than the phase variations, and fading elimination requires three times more channels in the data recording system than with a constant polarization state. Besides, a complete analysis of interference requires decomposition of LP modes on EH and HE modes.

Recently, Huang et al. have proposed a scheme that uses two orthogonally polarized differential interferometers operated within a two-mode, elliptical-core fiber [11]. Farahi et al. have considered the effects of heating and straining a common section of a birefringent fiber [122]. They have proposed a Fabry-Perot cavity-based sensor that can measure strain and temperature and have formalized a theory that includes cross-sensitivity considerations. Once a single-parameter sensor has been characterized in terms of its sensitivity and dynamic range, and calibrated for a specific application, it is relatively easy to implement the sensor and extract strain or temperature information from a real-life system.

Since the solution of simultaneous equations is critically dependent on the accuracy of the measured parameters of the sensing system, it is necessary to take one extra step in the analysis before a sensor is implemented. This step is that of determining whether a given sensor transfer function in a multi-parameter measurement scheme is robust enough to tolerate small measurement inaccuracies [122].

2.5 Conclusions

In this chapter, we review the receiver for optical communication systems, including coherent detection receiver and direct detection receiver. Principle and system architecture for each scheme is reviewed respectively. The motivation of the frequency response characterization is also illustrated. We also review the principle, the system configuration and the development of SDM for ultra-high-capacity optical transmission. Finally, we review recent development in FOS technology and the potential to use FMFs as in-line FOSs.

3 Characterization of Frequency Response for Optical Receivers with Laser Phase Noise Robustness

3.1 Introduction

In the past few years, DD based optical communication system has attracted attentions because of its low cost and simple implementation. In DD, it is important to separate the optical channel from RF channel. Consequently, calibration of the response for each optoelectronic component is necessary under such circumstance. In this chapter, we propose a novel DSP algorithm for photodiode characterization probed by three wavelengths. The DSP algorithm has low computational complexity. The required number of measurements increases logarithmically with the number of the spectral points. For the first time, the phase response of photodiode is characterized up to 20 GHz.

The arrangements of this chapter are as the following. Firstly the motivations and fundamentals to characterize the frequency response of the optical receivers are introduced. Then the principles of 2 - λ approach for amplitude response and 3 - λ approach for phase response are illustrated, which include theoretical fundamentals, algorithm deductions, and calibration arrangements of the approach. After that, we verify our proposed 3 - λ approach by comparing the phase response of an electrical filter calibrated through the proposed 3 - λ approach and that calibrated through conventional back-to-back electrical signal. For the experiment, we demonstrate the frequency response calibration of a high-speed optical receiver with 30-GHz bandwidth photodiode, and a low-speed optical receiver with 14-GHz bandwidth photodiode, respectively.

3.2 Fundamentals of frequency response characterization for optical receivers

The Internet traffic continues to grow unabated and the demand for high-speed transport is across every level of optical networks [123-125]. In fibre-optic communications, coherent detection has recently attracted many interests from the

optical communication community because of its high SE and robustness against impairments such as CD and PMD. One example is coherent optical OFDM (CO-OFDM. The advantage of CO-OFDM is prominent. It has the highest performance in receiver sensitivity, SE and robustness against linear channel impairments. By appropriately choosing the length of CP and insert training symbols at the transmitter, both inline CD and PMD can be fully compensated via DSP. However, the disadvantages of CO-OFDM also cannot be ignored. It requires a LO at the receiver, and is more sensitive to phase noise. CO-OFDM receiver also needs two pairs of balanced receivers therefore it is more costly and complex than. In addition, CO-OFDM also suffers from high peak-to-average-power ratio (PAPR) that leads to inferior nonlinearity tolerance than single-carrier system. Subsequently, for cost-sensitive short-reach high-speed communication, such as inter-cabinet communication, DM/DD is a more desirable option and has been actively explored [126-132].

One example of DM/DD is direct detection optical OFDM (DDO-OFDM). As well as compensating for CD, OFDM can correct for linear distortions in the electrical components, including the optical modulator and photodiode. This means DD-OOFDM systems are tolerant of linear imperfections and the experimental systems were implemented using commercial-off-the-shelf components. Another advantage is DD uses a single photodiode direct detection photoreceiver, which simplifies implementation and reduce application cost.

By using coherent detection, the channel response can be compensated by the DSP; however, characterization of each individual optoelectronic component is still critically important, especially for direct detection. In direct detection, the channel is nonlinear, and thus separation of the optical channel and RF channel is essential to remove the photodiode nonlinearity arising from its square-law detection [133]. Consequently, it is necessary to calibrate both amplitude and phase response of individual optoelectronic components, in the case of this report, the photodiode.

The response of the receiver system (photodiode plus subsequent RF components) includes the amplitude and phase response. The conventional method

to calibrate the response of a receiver system is to input two lasers with different wavelengths (called 2 - λ) and measure the output power from the photodiode [134]. By keeping the wavelength of one laser constant while sweeping the other, the frequency-dependent response of the photodiode can be obtained. However, this method is only applicable to obtaining amplitude response, incapable of detecting phase response.

In this section, we propose a novel method of calibrating the phase response of the receiver system by using 3 wavelengths (called 3 - λ approach in this section) and a novel DSP algorithm. The DSP algorithm has low computational complexity. The required number of measurements increases logarithmically with the number of the spectral points.

3.3 Principle of 2 - λ approach for amplitude response and 3 - λ approach for phase response

The response of a receiver system, H, is given by $H = Ae^{-j\Phi}$, where A and Φ are respectively the amplitude and phase response of the receiver system. The method of calibrating amplitude and phase response is described as follows:

❖ *2 – λ approach for amplitude response*

Two lasers at different wavelengths are coupled into a photodiode and the frequency difference between the two lasers is adjusted. The amplitude of the beating signals is measured. This amplitude is then calibrated against the laser output power at each frequency. The calibrated amplitude gives the amplitude response. This approach is commonly known and practiced in the telecom community [135].

❖ *3 - λ approach for phase response*

The main contribution of this chapter is our proposed 3 - λ approach for phase response measurement. The idea behind the 3 - λ approach is to use 3 lasers to eliminate the phase noise of each individual laser that exists in 2 - λ approach. In what follows, we describe the detailed principle of 3 - λ approach.

3.3.1 Theoretical fundamentals of 3 - λ approach

The optical field of the 3 lasers A_i is denoted as

$$A_i = a_i e^{j\Omega_i t + j\Phi_i(t)} \qquad (1 \le i \le 3) \tag{3.1}$$

where a_i, Ω_i and Φ_i are respectively the amplitude, angular frequency, and phase of each laser. After photo detection, 3 mixed RF signals are generated given by,

$$A_{ij} = a_i a_j R_{ij} e^{j(\Omega_j - \Omega_i)t} e^{j\Phi_j(t) - j\Phi_i(t)} e^{j\Phi_{ij}} \qquad (1 \le i \le 3, 1 \le j \le 3) \tag{3.2}$$

where A_{ij}, R_{ij} and Φ_{ij} are respectively the field, the amplitude response and the phase response of the mixed RF signal at the frequency of $\Omega_j - \Omega_i$. As shown in Eq. (3.2), this phase response of the photodiode is contaminated by phase noise of the lasers. To eliminate laser phase noise Φ_1, Φ_2 and Φ_3, we calculate the phase of $A_{13}/(A_{12} * A_{23})$. Using Eq. (3.2), we have

$$\begin{aligned} \Delta &\equiv angle(A_{13}/(A_{12} * A_{23})) \\ &= (\Omega_3 - \Omega_1)t + \Phi_3(t) - \Phi_1(t) + \Phi_{13} - ((\Omega_2 - \Omega_1)t + \Phi_2(t) - \Phi_1(t) + \Phi_{12} \\ &\quad + (\Omega_3 - \Omega_2)t + \Phi_3(t) - \Phi_2(t) + \Phi_{23}) \\ &= \Phi_{13} - \Phi_{23} - \Phi_{12} \end{aligned} \tag{3.3}$$

It follows from Eq. (3.3) that Ω_1, Ω_2, Ω_3, Φ_1, Φ_2 and Φ_3, have all been canceled, and thus laser phase noise Φ_1, Φ_2 and Φ_3, has been eliminated from Δ, leaving only the terms of phase responses of photodiode. For simplicity, we use abbreviated notations for the qualities related to the mixed RF signals including the phase of $\varphi_1 \equiv \Phi_{12}$, $\varphi_2 \equiv \Phi_{23}$, $\varphi_3 \equiv \Phi_{13}$, and frequency of $\omega_1 \equiv \Omega_2 - \Omega_1$, $\omega_2 \equiv \Omega_3 - \Omega_2$, $\omega_3 \equiv \Omega_3 - \Omega_1$. Using the abbreviated notations and after simple rearrangement, Eq. (3.3) becomes

$$\varphi_3 = \varphi_1 + \varphi_2 + \Delta \tag{3.4}$$

It can be seen from Eq. (3.4) that the phase response at high frequency can be computed by the summation of the phase response at two lower frequencies. Therefore, the novelty of $3-\lambda$ approach lies in the fact that even the 3 lasers is

noisy and uncorrelated, their phase noises can be completely removed without affecting the phase response measurement. By applying Eq. (3.4) iteratively, phase response at each frequency can be obtained.

3.3.2 Calibration Arrangements of 3 - λ approach

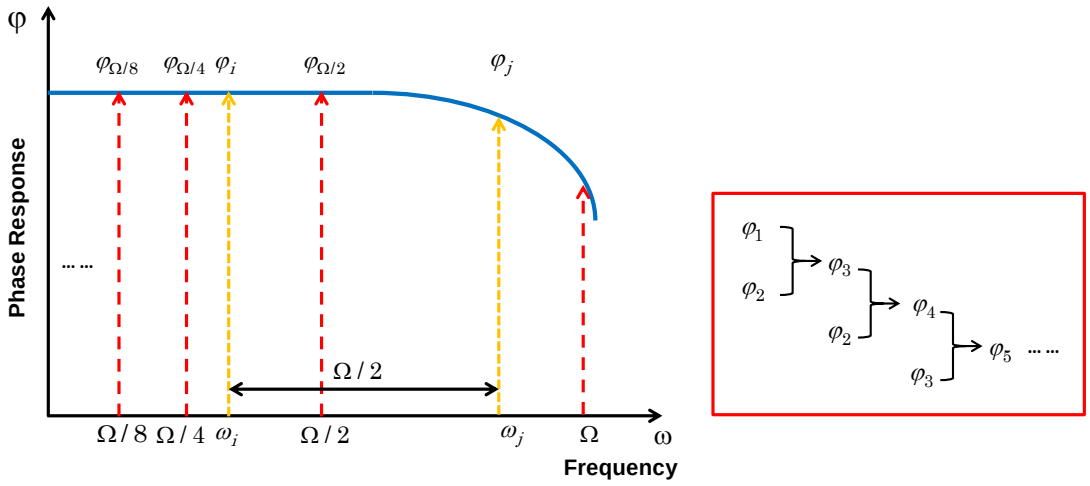

Fig. 3.1. Principle of dichotomization to minimize number of measurement iterations.

The iterative procedure is laid out as follows:

(i) In step (i), φ_1 and φ_2, which are respectively the phase responses of ω_1 and ω_2, are assumed as known values. It can be also easily shown that $\omega_3 = \omega_2 + \omega_1$. We then compute the phase difference Δ among the three beating signals by applying Eq. (3.3). The phase response of ω_3, φ_3 can be obtained by using Eq. (3.4).

(ii) Similar to step (i), in step (ii), we generate 3 tones ω_i, ω_{i+1}, ω_{i+2} (where $\omega_{i+2} = \omega_{i+1} + \omega_i$). φ_i and φ_{i+1}, which are respectively phase responses of ω_i and ω_{i+1} are assumed known in the previous steps. The phase difference of Δ_i is computed and we can calculate the phase response of ω_{i+2} using $\omega_{i+2} = \omega_{i+1} + \omega_i + \Delta_i$. We repeat step (ii) until ω_{i+2} reaches the maximum frequency.

Note that every step generates measurement inaccuracy error. To minimize the accumulated measurement error, we minimize the number of iterations at each frequency. One powerful approach is dichotomization, which is shown in Fig. 3.1, depicting phase response from 0 to Ω. If we want to calibrate the phase response at an arbitrary frequency ω_j within the range of $\Omega/2$ to Ω, we can obtain its phase based on the known phase response at the frequency $\omega_i = \omega_j - \Omega/2$, which is in the range of 0 to $\Omega/2$. Namely, we generate three beating signals at the frequency of ω_i, ω_j and $\Omega/2$, from Eq. (3.4) the phases at these frequencies are related by

$$\varphi_j = \varphi_i + \varphi_{\Omega/2} + \Delta_j \tag{3.5}$$

where φ_i, φ_j and $\varphi_{\Omega/2}$ are the phase responses at the frequency ω_i, ω_j, and $\Omega/2$ respectively, while Δ_j is the phase difference among the three beating signals by applying Eq. (3.3). Similarly, if we want to calibrate the phase response in the range between 0 to $\Omega/2$, then we could use the known value in the range between 0 to $\Omega/4$. In this way, the maximum number of iterations to compute the phase response is proportional to $\log_2(\Omega/\Omega_{\min})$ where $\Omega_{\min}$ is the minimum frequency of the calibration.

Following the above procedures, the last task is to obtain two initial values of the phase response whose frequencies are close to 0 Hz. Theoretically, phase response of 0 Hz is 0 rad (the photodiode polarity can generate additional phase of π which can be corrected easily in the program). In this way, phase responses of the whole frequency range could be characterized given that two initial values are 0 rad. In this report, the initial two frequencies we used are 50 MHz and 100 MHz.

3.3.3 Verification of 3 - λ approach

To verify the phase response of the photodiode (DSC-R409) at the frequency close to zero, we generate one beating signal ω_1 at the range of 20 MHz to 200 MHz. The resolution is 10 MHz, and another two beating signals $\omega_2 = 5\ GHz - \omega_1$,

$\omega_3 = 5\ GHz + \omega_1$. Then we calculate the phase difference of the three beating signals using Eq. (3.4). Since ω_1 is very close to 0 Hz, the phase response φ_2 (at the frequency ω_2) should also be close to φ_3 (at the frequency ω_3) in the phase response curve. Consequently, the phase difference Δ should be approximately equal to 0 rad if the phase response φ_1 (at the frequency of ω_1) is close to 0 rad. The curve of phase difference Δ against beating signal ω_1 is shown in Fig. 3.2. From Fig. 3.2, we can see that Δ at every frequency is in the neighborhood of 0, with maximum difference value 0.05 rad (approximately 3.1 degree), which is consistent with the assumption. Thus, we can tell that phase responses at the frequency close to 0 Hz are close to 0 rad. In this report, we use 50 MHz and 100 MHz as two initial frequencies given that their phase responses are 0 rad.

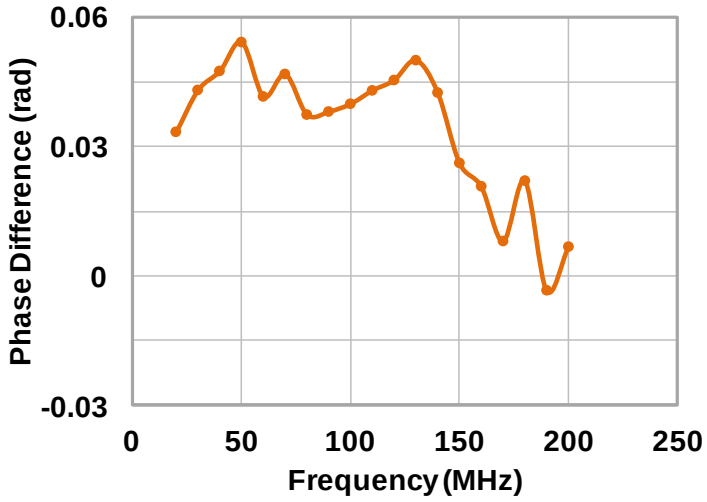

Fig. 3.2. Phase difference of the photodiode (DSC-R409) at the frequencies close to zero.

To verify our proposed 3-λ approach for phase response, we calibrated an electrical filter using the 3-λ method. First we add an electrical filter (Mini Circuit VLF- 3000+) whose nominal bandwidth is 3-GHz after the DSC-R409 photodiode and calibrate the combined phase response of the photodiode and the filter. Then we calibrate the phase response of the DSC-R409 photodiode alone. As a result, if we subtract the phase response of the photodiode from the combined phase response, we can have the phase response of the 3-GHz filter, which is shown in Fig. 3.3. Also,

we directly calibrate the phase response of the electrical filter using the conventional approaching of back-to-back electrical signal without electrical-optical (O/E) and optical-electrical (E/O) conversion as reference. In Fig. 3.3, both responses are flat from 100 MHz to 2.5 GHz, and then roll off 0.5 rad (approximately 28.7 degree) in the vicinity of 3 GHz, and 2.5 rad (approximately 143.3 degree) in the vicinity of 4 GHz, which are consistent with the actual phase response of the filter. We can see that patterns of both curves are similar, with average difference 0.01 rad (approximately 0.6 degree) between the two curves within 4 GHz. Thus, we can tell that our 3-λ method is valid for phase calibration.

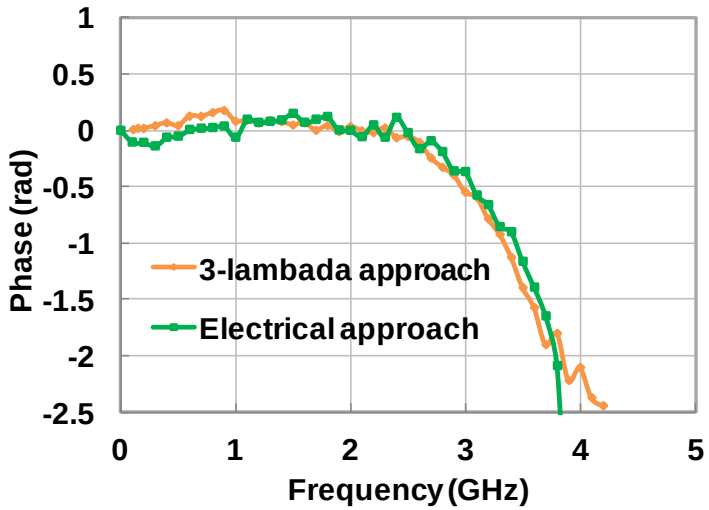

Fig. 3.3. Phase response of the 3 GHz filter calibrated using the 3-λ approach compared with that using electrical approach.

3.4 Calibration of frequency response of a low-speed (14 GHz) and a high-speed (30 GHz) optical receiver

3.4.1 System configuration

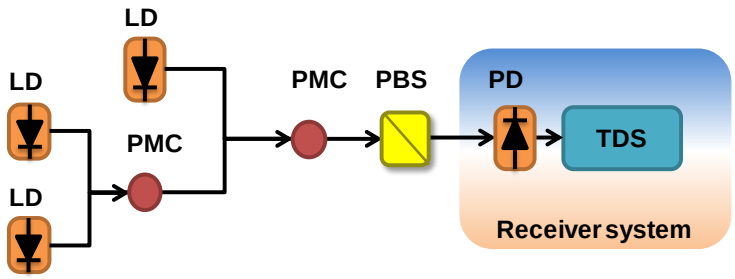

Fig. 3.4. System configuration I for phase response calibration: using three lasers. PD: Photo diode, PBS: Polarization beam splitter, LD: Laser diode, PMC: Polarization-maintaining coupler, TDS: Time-domain sampling scope.

System configuration for 3-λ phase response characterization is shown in Fig. 3.4 and Fig. 3.5. There are two methods employed. In Method I, as shown in Fig. 3.4, 3 external cavity lasers (ECLs) coupled with two polarization maintaining couplers (PMC) are fed into a polarization beam splitter (PBS). The reason to use a PBS is to align 3 lasers into one polarization so that signal beating is constrained within one polarization. The optical signal is then fed into a receiver system which consists of a photodiode (Discovery Semiconductors DSC-R409 or DSC-R405) and an oscilloscope (Tektronix DPO72004B). The sampling rate of the oscilloscope is 50 GSa/s, and the bandwidth of the oscilloscope is 20 GHz.

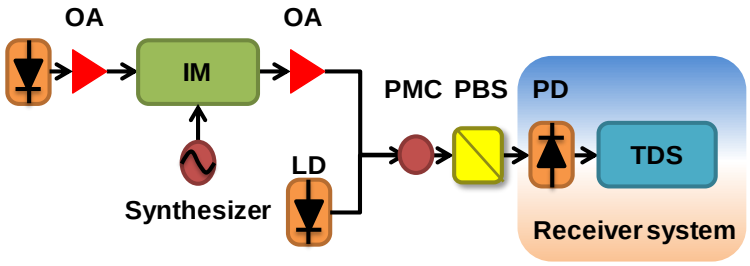

Fig. 3.5. System configuration II for phase response calibration: using two lasers and a modulator. IM: Intensity modulator, OA: Optical amplifier.

In Method II, instead of using 3 lasers to generate 3 wavelengths as illustrated in Fig. 3.5, we can also use an intensity modulator to generate two tones from one laser, and therefore only two lasers are needed, as shown in Fig. 3.5.

3.4.2 Experimental demonstration

3.4.2.1 Experimental demonstration of frequency response calibration of a high-speed optical receiver with 30-GHz bandwidth photodiode

The response of the receiver system with DSC-R409 photodiode is shown in Fig. 3.6 and Fig. 3.7. The nominal bandwidth of the DSC-R409 photodiode is 30 GHz. In Fig. 3.6 the amplitude response declines 9 dB at 20 GHz. The roll-off of the amplitude curve calibrated is due to the limited bandwidth of the oscilloscope since the bandwidth is less than 20 GHz.

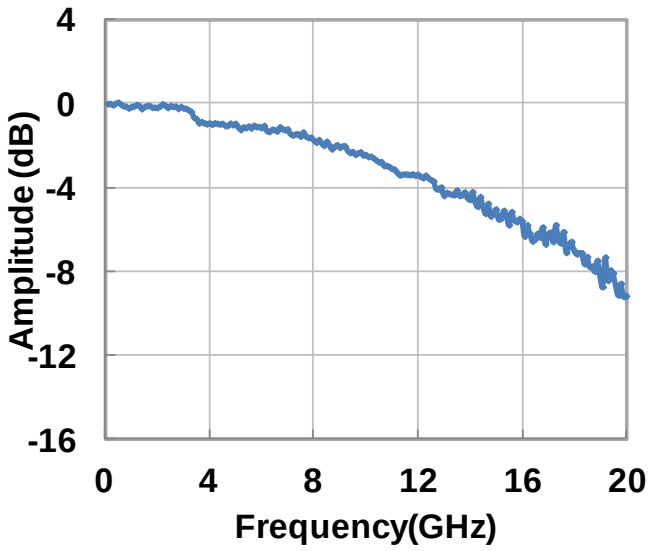

Fig. 3.6. Amplitude response of the receiver system with DSC-R409 photodiode.

Fig. 3.7 shows the phase response of the receiver system calibrated by Method I and Method II. The fluctuation and patterns of both curves are similar. Average phase difference between two methods from 0 GHz to 15 GHz is 0.018 rad (approximately 1.0 degree); average phase difference in the whole band between the two calibration results is 0.03 rad (approximately 1.7 degree). The increase in average difference could be resulted from the decline of the amplitude response which enlarges the calibration error. It can be seen from Fig. 3.7 that the phase response of the photodiode is flat and fluctuates in the range of ± 0.2 rad (approximately 11.4 degree), as the calibration bandwidth is within the bandwidth of

DSC-R409. Also, the phase fluctuation is not from the intrinsic photo-detection but from the trans-impedance amplifier integrated in the photodiode.

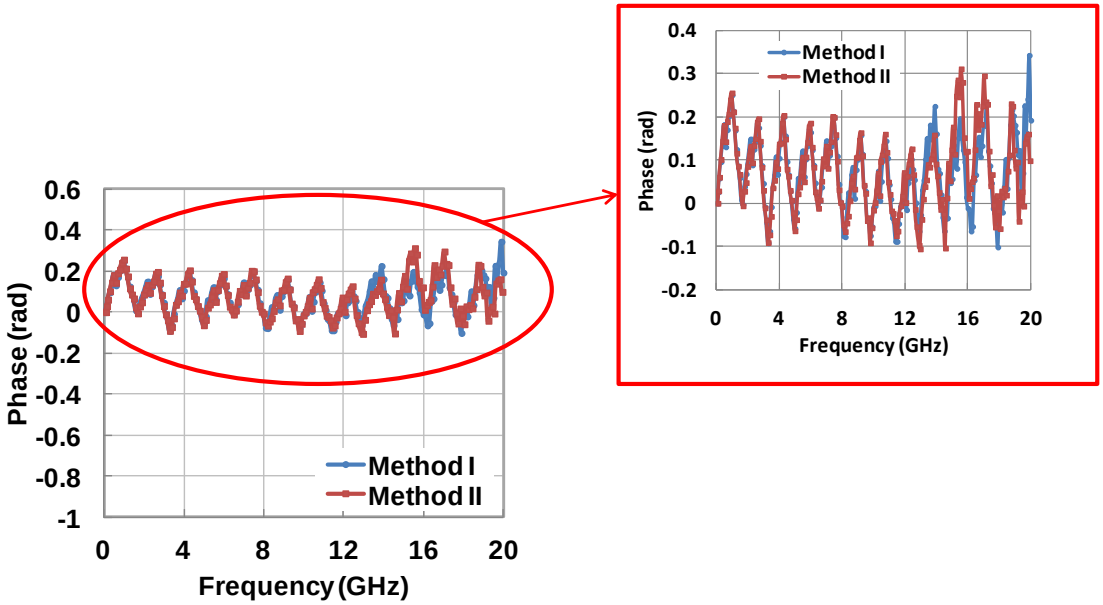

Fig. 3.7. Phase response of the receiver system with DSC-R409 photodiode.

3.4.2.2 Experimental demonstration of frequency response calibration of a low-speed optical receiver with 14-GHz bandwidth photodiode

The response of the receiver system with DSC-R405 photodiode is shown in Fig. 3.8 and Fig. 3.9 to show different response compared to DSC-409. The nominal bandwidth of the DSC-R405 photodiode is 14 GHz. The amplitude response gradually declines 3 dB in the vicinity of 10 GHz, and rapidly declines up to 10 dB from 10 to 16 GHz.

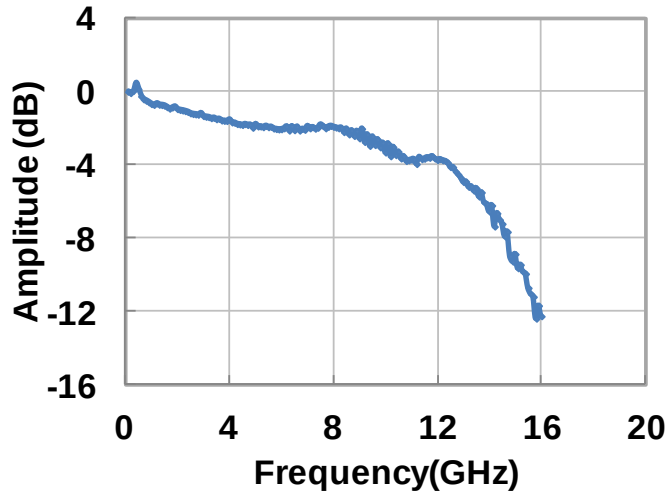

Fig. 3.8. Amplitude response of the receiver system with DSC-R405 photodiode.

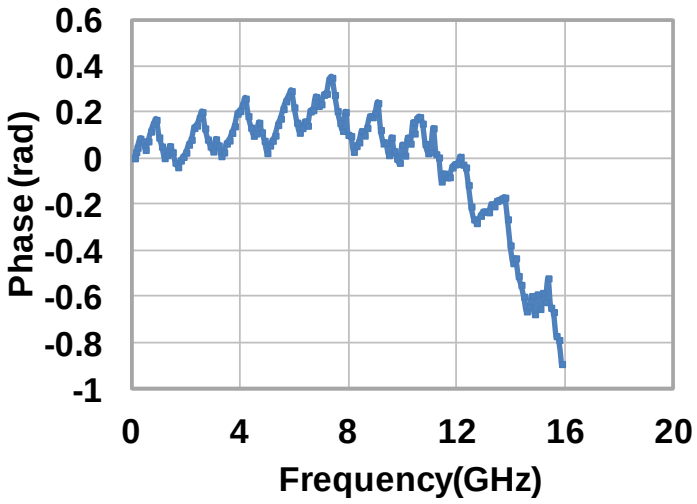

Fig. 3.9. Phase response of the receiver system with DSC-R405 photodiode using Method I.

Fig. 3.9 shows the phase response measurement results. The response is flat and fluctuates in the range of 0.3 rad (approximately 17.2 degree) from 100 MHz to 10 GHz, and rolls off significantly from 10 to 16 GHz, with the maximum phase shift of 1 rad (approximately 57.3 degree) within 16 GHz. The pattern of phase response is consistent with that of amplitude response, which is flat within the range of the bandwidth and drops rapidly out of the range. Due to its narrower bandwidth compared to DSC-R409, DSC-R405 photodiode has larger phase response. Since

power received after 16 GHz is less than -10 dB, the phase response calibrated may not be valid.

3.4.3 Results and discussions

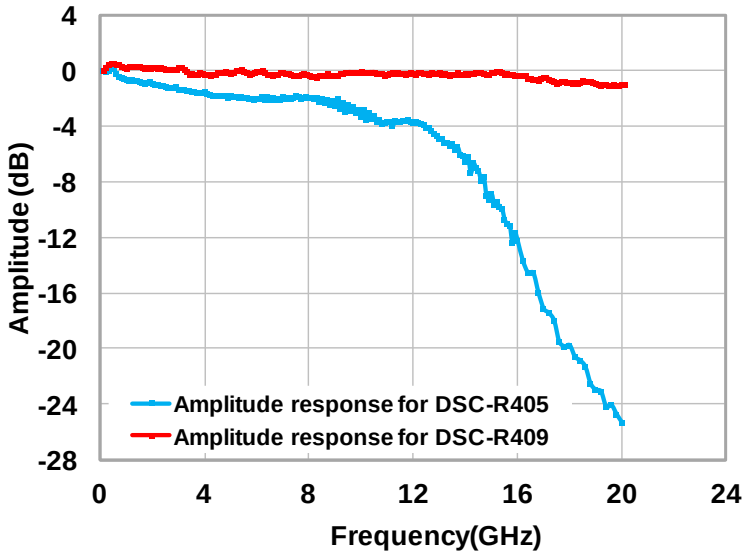

Fig. 3.10. Amplitude response of DSC-R409 up to 26 GHz compared to that of DSC-R405.

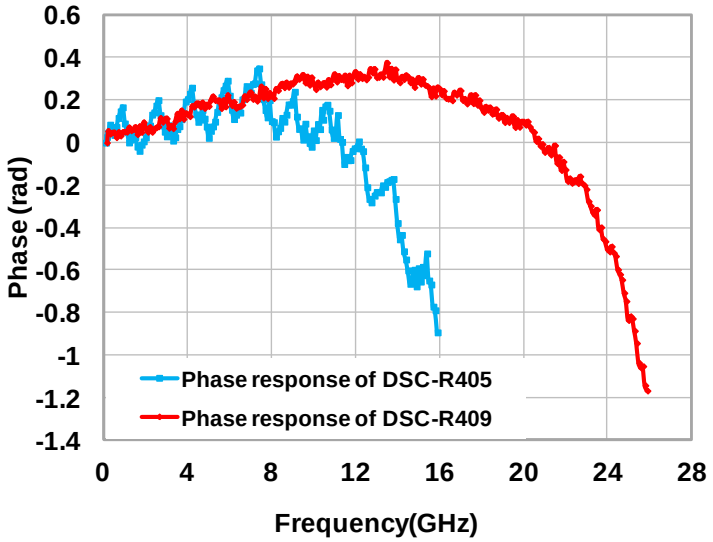

Fig. 3.11. Phase response of DSC-R409 up to 26 GHz compared to that of DSC-R405 using Method I.

To compare the performance differences between the two receivers, both curves are shown in Fig. 3.10 and Fig. 3.11. The response curve of DSC_R409 is very similar to that of DSC_R405, with only difference lies in that the range of fluctuation extend to 20 GHz, and the range of decline is from 20 to 26 GHz due to its high nominal bandwidth of the PD DSC-R409. Both patterns of phase response are consistent with that of amplitude response, which is relatively flat within the range of the bandwidth and drops rapidly out of the range.

We also note that, for every RF frequency ω, the phase response φ is the function of ω and can be denoted as Taylor expansion with respect to ω, that is, $\varphi = f(\omega) = \sum_i^n S_i \omega^i = S_0 + S_1\omega + R_1(\omega)$, where S_0 is common phase of the system, $S_1\omega$ is time delay, and $R_1(\omega)$ is high-order dispersion. As the first two terms represents the DC phase offset and a common time delay, which does not reflect the true dispersion of the photo-diode, and thus we have removed the DC term S_0 and linear term $S_1\omega$ from the measured data in all the figures.

3.5 Conclusions

In this chapter, we first introduce the motivations and fundamentals to characterize the frequency response of the optical receivers. Then the chapter introduces the principle of 2 - λ approach for amplitude response and 3 - λ approach for phase response chracterization, which includes theoretical fundamentals, algorithm deductions, and calibration arrangements of the approach. After that, we verify our proposed 3 - λ approach by comparing the phase response of an electrical filter calibrated through the proposed 3 - λ approach and that calibrated through conventional back-to-back electrical signal. For the experiment, we demonstrate the frequency response calibration of a high-speed optical receiver with 30-GHz bandwidth photodiode, and a low-speed optical receiver with 14-GHz bandwidth photodiode, respectively.

4 Few-Mode Fiber Based Optical Sensors

4.1 Introduction

FMFs have found applications in optical communications and sensors with attractive features that standard single mode fibers (SSMF) do not possess. In this chapter, we review our recent progress in the design and fabrication of FMF based optical sensors. The organization of this section is as follows: In Section 4.3, we report two FMF based discrete sensors, one is a fiber Sangac loop sensor based on polarimetric interference, and the other is a few-mode interferometer sensor based on intermodal interference. The system configurations of both sensors are illustrated and their sensitivities to temperature and strain are shown and compared. In Section 4.4, we introduce the concept of FMF based distributed sensors. We reviewed the basic concept of Stimulated Brillouin scattering (SBS), and demonstrate characterization of SBS in a FMF based on BOTDA technique. Furthermore, we propose two Brillouin optical time domain analysis (BOTDA) methods for the FMF, the first one is based on the characterization of Brillouin gain spectra (BGS) with a two-wave pump-probe configuration, and the second one is based on characterization of the Brillouin dynamic grating (BDG) with a three-wave pump-probe configuration. The proposed setup can also be used as a Brillouin distributed sensor. In detail, we launch a pump and a probe signal through specific LP modes into a FMF, and monitor the Brillouin frequency shift (BFS) in each mode. By analyzing the temperature and strain coefficients of the BFS of the two lowest order (LP_{01}, LP_{11}) modes, discrimination of temperature and strain are successfully demonstrated. For few-mode fiber based discrete optical sensors (section 4.3), the thesis author is the main contributor; for few-mode fiber based distributed optical sensors (section 4.4), the thesis author is the co-contributor.

4.2 Fundamentals of fiber based optical sensors

Optical fiber sensors have been widely studied over the last few decades owing to their advantages of compactness, high reliability, high sensitivity and low fabrication cost [136-145]. In such sensors, optical fiber is the most critical sensing element. The

sensing ability of optical fibers has been realized through fiber-optic technologies such as FBG [137-140], fiber interferometers [136-142], scattering effects [143-145], fiber couplers, nanowires, etc. Nowadays, optical fiber sensors can be used to measure various parameters including temperature, strain, pressure, bending, ultrasound, and so on, thanks to the above innovative technologies. SMFs are widely used in optical fiber sensors, which can be SSMF, polarization-maintain fiber (PMF), or photonic crystal fiber (PCF). For example, Sagnac loop interferometer (SLIs) that based on the polarimetric interference uses conventional PMF [1] or polarization-maintaining PCF (PM-PCF) as the sensing element [15].

Early study has shown that the performance of optical fiber sensor (e.g, sensitivity, reach, etc.) depends not only on the sensing technique but also on the parameters of the sensing element - optical fiber. However, the sensor performance is not the only consideration in fiber and sensor design because the cost and commercial availability of the fiber are also important. Therefore, it is necessary to develop a fiber with high sensing performance while keeping the fabrication cost at low level. In recent years, FMF has attracted much research interest because it has the potential to overcome the capacity limit of SSMF [1, 16]. By exploring the fifth dimension - the spatial dimension in addition to the four dimensions of time, wavelength, polarization and phase that have been well studied in SMFs, FMFs can provide more capacities and flexibilities than the SSMF. With the powerful technique of SDM, the spatial modes in a FMF can be deemed as independent signal channels [146-147]. The advance into space dimension has benefited not only the optical communications but also many other fields like optical sensors. FMF based optical fiber sensors emerges as an interesting topic which was studied by Kim *et al.* [9] since 1980s. Compared with SMF based fiber sensors, FMF based fiber sensors have many unique advantages such as cost effectiveness, high sensitivity, and discrimination of perturbation effects [122]. Furthermore, because there is almost no difference between SMF and FMF except the small change in core refractive index (RI) and/or core diameter [146-147], the fabrication process of FMF can be as simple and the cost can be as low as the SSMF, which is much lower than the conventional PMF or specially-designed PM-PCF [142].

The optical fiber sensors can be classified into two major categories, (1) discrete sensors, and (2) distributed sensors. Discrete fiber sensors are mostly based on an interferometer structure [136-142]. The advantage of interferometric sensors is that the perturbation effects can be conveniently translated into a phase change in the interferometer. On the other hand, distributed fiber sensors are very popular because they can offer continuous and non-disruptive sensing along a fiber over tens of kilometers [148]. The spatial resolution of distributed sensors can reach millimeter-order whilst still have good accuracy and sensitivity to the perturbation effects [149]. Distributed fiber sensors can be realized through utilization of the scattering effects in a fiber such as Rayleigh scattering [143], Brillouin scattering [144], and Raman scattering [145]. Among all these scattering effects, the Brillouin scattering - especially the SBS, is very attractive because it is very sensitive to the RI change in a fiber, which can be affected by the external perturbations such as temperature, strain and pressure. Distributed Brillouin sensing has been efficiently achieved over SMFs or PMFs using powerful techniques such as the well-known Brillouin optical time-domain reflectometry (BOTDR) [150] and BOTDA [151]. For FMFs, the SBS effect is not very well understood because many spatial modes can be involved. Most reported early work focuses on the generation of inter-modal SBS in a FMF, e.g., Russell, *et al.* demonstrated the forward SBS between co-propagating LP_{01} and LP_{11} modes in a dual-mode fiber [151], Song, *et al.* [152] reported the SBS between the counter-propagated LP_{01} and LP_{11} modes in an elliptical-core two-mode fiber (e-TMF), Li, *et al.* [153] demonstrated all-optical generation of BDG in a FMF, and Kim, *et al.* [154] also measured the intermodal beat length distribution in an e-TMF based on BDG. All these experiments touch the interesting topic of SBS effect in a FMF, yet the distributed sensing capability of FMFs are not revealed or fully understand. Therefore it remains an interesting question that whether FMFs are suitable sensing element for the distributed sensors.

In this chapter, we report our recent progress on FMF based optical sensors with a few proof-of-principle experiments to demonstrate the potential of utilizing the additional dimension of spatial mode in the optical sensing field.

4.3 Few-mode fiber based discrete optical sensors

Discrete sensing in SMFs can be realized by interferometric sensors which have been widely studied for years. There are many types of interferometric sensors including the Michelson interferometer (MI), Fabry-Perot interferometer (FPI), Sagnac loop interferometer (SLI), Mach-Zehnder interferometer (MZI), etc. The interference pattern in an interferometric sensor can be generated from signal in same polarization but different paths, or signal in two orthogonal polarizations with birefringence, e.g., using a high bifringence (Hi-Bi) single mode PMF. For a polarization-maintaining FMF (PM-FMF), the interference could happen between both the polarizations and spatial modes, known as the polarimetric and intermodal interference [155]. Similar as the SMF (or PMF), a FMF (or PM-FMF) is also sensitive to external perturbations such as the temperature, pressure and strain. The responses of polarimetric and intermodal interference to the external perturbations in a PM-FMF are normally very different [156], which could potentially improve the fiber sensitivity. The additional information from spatial dimension could also be utilized to discriminate different perturbation effects. In the following subsections, we will demonstrate the polarimetric and intermodal interference and their response to the temperature and strain in a PM-FMF and a circular-core FMF (c-FMF).

4.3.1 Definition of Strain

Strain is the amount of deformation of a body due to an applied force. More specifically, strain (ε) is defined as the fractional change in length, as shown in Fig. 4.1 below.

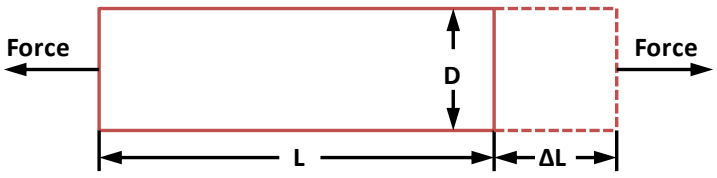

Fig. 4.1. Definition of Strain

Strain can be positive (tensile) or negative (compressive). Although dimensionless, strain is sometimes expressed in units such as in./in. or mm/mm. In

practice, the magnitude of measured strain is very small. Therefore, strain is often expressed as microstrain (με), which is ε × 10–6.

When a bar is strained with a uniaxial force, as in Fig. 4.1**,** a phenomenon known as Poisson Strain causes the girth of the bar, D, to contract in the transverse, or perpendicular direction. The magnitude of this transverse contraction is a material property indicated by its Poisson's Ratio. Poisson's Ratio for steel, for example, ranges from 0.25 to 0.3, while

$$\varepsilon = \Delta L / L . \tag{4.1}$$

4.3.2 Polarimetric interferometer sensor

4.3.2.1 Theoretical fundamentals

The polarimetric interference in a single-mode PMF can be simply generated by a SLI, which has attracted a lot of interest recently due to its simple structure and environmental robustness. To demonstrate the feasibility of using PM-FMF for the polarimetric interferometer sensor, we build a PM-FMF based SLI sensor and the experimental setup is introduced in next Section. Similar as in the PMF or PM-PCF case [141-142], from the transfer matrix of the proposed PM-FMF SLI sensor device, we can simply get the interfered pattern between the two polarizations of LP_{01} mode in the PM-FMF as

$$t = \sin^2\left(\frac{\pi}{\lambda} B_{xy} L\right) = \frac{1-\cos\phi}{2} \tag{4.2}$$

where t is the optical intensity transmission, L is the length of PM-FMF, B_{xy} is the birefringence between x- and y- polarizations of LP_{01} mode in the PM-FMF, $B_{xy} = \Delta n_{xy} = n_{01x} - n_{01y}$, and ϕ is the phase difference between the two polarizations of LP_{01} mode in the PM-FMF, $\phi = (2\pi / \lambda) B_{xy} L$. As can be seen, the transmission peaks occur when $\phi = m \cdot 2\pi$ where m is an integer. The wavelength spacing of the transmission peaks $\Delta\lambda$ in the vicinity of λ can thus be obtained, given by

$$\Delta\lambda = \frac{\lambda^2}{B_{xy}L} \tag{4.3}$$

If both the birefringence B_{xy} and fiber length L are temperature dependent, the phase-shift sensitivity of the SLI can be written as

$$\frac{d\phi}{dT} = \frac{2\pi}{\lambda}(L\frac{dB_{xy}}{dT} + B_{xy}\frac{dL}{dT}) \ . \tag{4.4}$$

Assuming there is no fiber elongation effect ($dL/dT = 0$), with the calculation $d\phi = (2\pi/\lambda^2)B_{xy}Ld\lambda$ the wavelength shift of the transmission peak (or minimum) will be given by

$$\frac{d\lambda}{dT} = \frac{\Delta\lambda L}{\lambda}\frac{dB_{xy}}{dT} = \frac{\lambda}{B_{xy}}\frac{dB_{xy}}{dT} \ . \tag{4.5}$$

Similarly, assuming strain change is ε, the phase-shift sensitivity can be written as

$$\frac{d\phi}{d\varepsilon} = \frac{2\pi}{\lambda}(L\frac{dB_{xy}}{d\varepsilon} + B_{xy}\frac{dL}{d\varepsilon}) \tag{4.6}$$

and the wavelength shift of the transmission peak (or minimum) will be given by

$$\frac{d\lambda}{d\varepsilon} = \frac{\lambda}{B_{xy}L}(L\frac{dB_{xy}}{d\varepsilon} + B_{xy}\frac{dL}{d\varepsilon}) = \lambda\left(1 + \frac{1}{B_{xy}}\frac{dB_{xy}}{d\varepsilon}\right), \varepsilon = \Delta L / L \tag{4.7}$$

where L is fiber length, ΔL is the elongation. It can be seen that the spectral shift is also linearly proportional to the strain change.

4.3.2.2 System configuration

As mentioned in Section above, Fig. 4.2 shows the experimental setup of the Sagnac loop polarimetric interferometer sensor. The light source is a broadband amplified spontaneous emission (ASE) source generated from an EDFA. The broadband light passes through an isolator to remove the influence of back-reflection to the EDFA, and is split into two paths by a conventional 3-dB SMF coupler. The upper and lower paths of the 3-dB SMF coupler are connected with the fiber under test (FUT, here we

use the PM-FMF as the FUT) using center launch technique so as to generate only the fundamental (LP_{01}) mode. The output of the interferometer is connected to a high resolution (0.16 pm) optical spectrum analyzer (OSA).

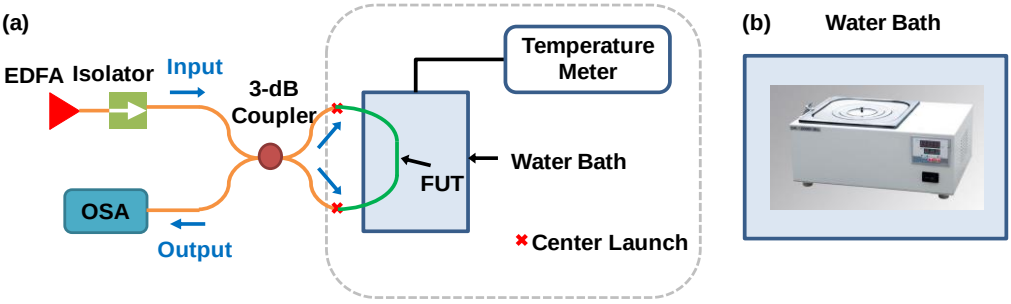

Fig. 4.2. (a) Schematic diagram of a fiber SLI sensor based on a PM-FMF with a temperature chamber. (b) Photo of the actual water bath employed in the experiment. FUT: fiber under test.

To measure the temperature dependence of the PM-FMF SLI sensor, the PM-FMF is placed in a water bath with digital proportional-integral-derivative (PID) control and liquid crystal display (LCD).

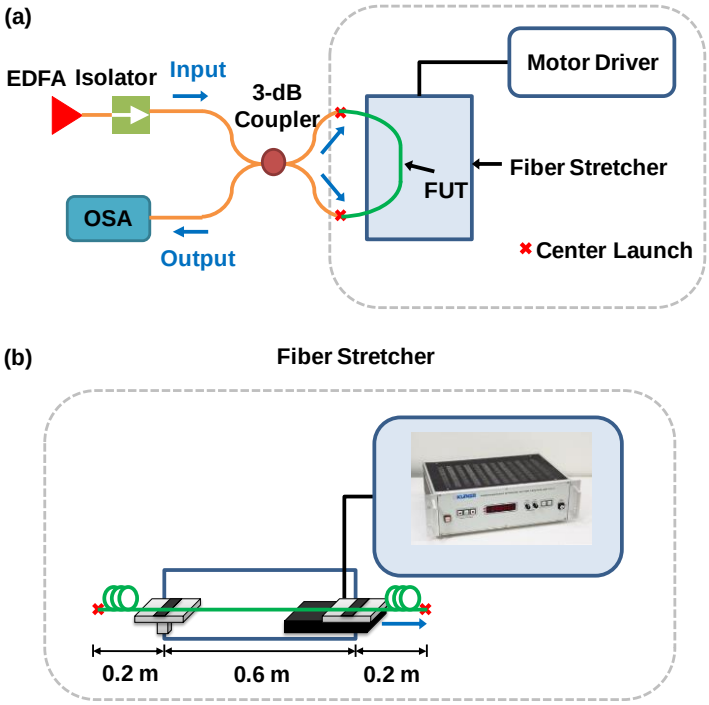

Fig. 4.3. (a) Schematic diagram of a fiber SLI sensor based on a PM-FMF with a strain controller. (b) Structure of the fiber stretcher employed in the experiment.

For strain characterization, bare fibers are used with one end of the fiber fastened to a fixed stage and the other end glued to a metal plate mounted on a motorized linear stage (Klinger Programmable Stepper Motor Driver). By tuning the position of the linear stage, we can elongate the test fiber and control the applied strain which is shown in Fig. 4.3.

4.3.2.3 Experimental demonstration

To characterize the performance of polarimetric interferometer sensor, the FUT is a PANDA fiber (PM2000, THORLABS) which has a core diameter of 7.0 µm and cladding diameter of 125 µm. The second mode cut-off wavelength is at 1720 ± 80 nm. The beating length is 5.2 mm and the attenuation is < 11.5 dB/km @ 1950 nm. When operating at 1550 nm window, it becomes a bi-modal PM-FMF that supports two spatial modes: LP_{01} and LP_{11} even mode (LP_{11e}), while the LP_{11} odd mode (LP_{11o}) is intentionally cut-off. In this experiment, the ASE noise from EDFA spans from 1526 nm - 1566 nm; the insertion losses of the free space coupler is 0.7 dB; the output of the interferometer is connected to a high resolution (= 0.16 pm) optical spectrum analyzer (OSA).

We first measure the temperature dependence of a 10-meter PM-FMF sensor and some of the measured power spectra around 1550 nm are shown in Fig. 4.4(a). The temperature is measured from 30 °C to 70 °C with a step size of 1 ^{o}C. As can be seen, the wavelength spacing between two transmission minima is ~0.667 nm, and the extinction ratio is about 12.1 dB at the transmission minimum located at 1550 nm. From the spectra we calculate the wavelength shift of the minimums as a function of temperature, as shown in Fig. 4.4(b). We then replace the PM-FMF with a typical single-mode PANDA type PMF (AFW Technologies, DGD = 1.3 ps/m) that has a same fiber length (10 meter) and measure again the temperature response of the SLI sensor for comparison. The result is also shown in Fig. 4.4(b). The measured temperature coefficient is -1.25 nm/°C for PMF and -1.72 nm/°C for PM-FMF, respectively. Obviously, PM-FMF based SLI sensor shows better temperature sensitivity as the temperature coefficient is about 1.4 times that of conventional

PMF based SLI sensor. The reason for improved sensitivity of PM-FMF fiber is that it has smaller polarimetric birefringence B_{xy} than conventional PMF.

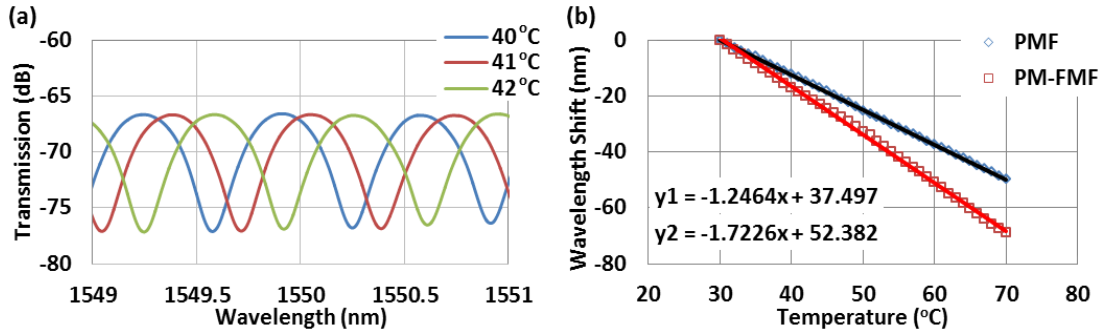

Fig. 4.4. (a) Measured output power spectra (smoothed over 0.1 nm) of the 10-meter PM-FMF SLI under different sensor temperatures, and (b) wavelength shift of the transmission minimum around 1550 nm against temperature. y1 and y2 are the linear curve fittings for the 10-meter PMF and PM-FMF, respectively.

We continue to measure the strain dependence of a 1-meter PM-FMF sensor with 0.6-meter sensing length and some of the measured power spectra around 1550 nm are shown in Fig. 4.5(a). The strain is measured from 0 με to 5000 με with a step size of 500 με. As can be seen, the wavelength spacing between two transmission minima is ~6.299 nm, and the extinction ratio is about 20.5 dB at the transmission minimum located at 1550 nm. From the spectra we calculate the wavelength shift of the minimums as a function of strain, as shown in Fig. 4.5(b). We then replace the PM-FMF with a typical single-mode PANDA type PMF (AFW Technologies, DGD = 1.3 ps/m) that has a same fiber length (1 meter) and sensing length (0.6 meter), and measure again the strain response of the SLI sensor for comparison. The strain is measured from 0 με to 5000 με with a step size of 166.7 με. The result is also shown in Fig. 4.5(b). The measured strain coefficient is 2.0 pm/με for PMF and 24.5 pm/με for PM-FMF, respectively. Obviously, PM-FMF based SLI sensor shows better strain sensitivity as the strain coefficient is about 12.2 times that of conventional PMF based SLI sensor. The reason for greatly improved strain sensitivity of PM-FMF fiber is that it has smaller polarimetric birefringence B_{xy} than conventional PMF.

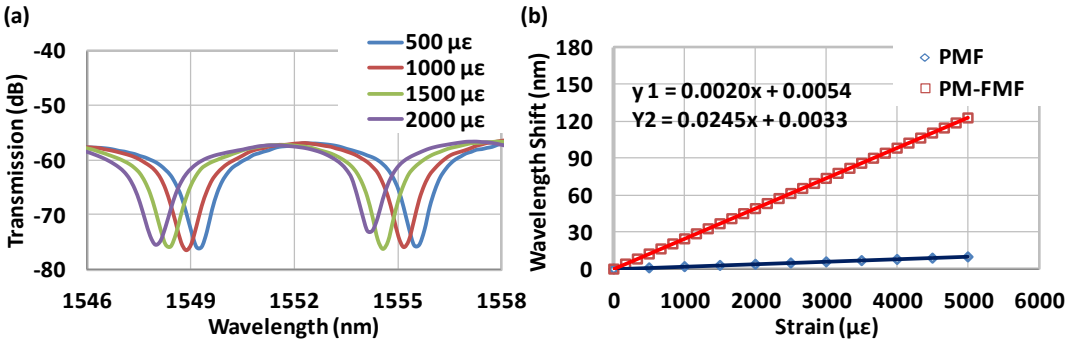

Fig. 4.5. (a) Measured output power spectra (smoothed over 0.1 nm) of the 1-meter PM-FMF SLI under different sensor strains, and (b) wavelength shift of the transmission minimum around 1550 nm against strain. y1 and y2 are the linear curve fittings for the 1-meter PMF and PM-FMF, respectively.

4.3.3 Intermodal interferometer sensor

4.3.3.1 Theoretical fundamentals

As was discussed earlier, intermodal interference could also happen between the spatial modes in a FMF. The intermodal interferometer sensor has the same sensitivity equations (Eqs. (4.2)-(4.7)) as the SLI sensor, except that the birefringence factor B_{xy} now becomes the modal birefringence B_{ij} between two spatial modes *i* and *j* (e.g., LP_{01} and LP_{11} mode), for example, $B_{ij} = n_{01x} - n_{11x}$ or $B_{ij} = n_{01y} - n_{11y}$ if the input light is aligned with x- or y-polarization in the FMF.

4.3.3.2 System configuration

We build an intermodal interferometer temperature sensor to demonstrate the intermodal interference response of the FMF. The experimental setup is shown in Fig. 4.6. Similar as in Fig. 4.2, the light source is the same broadband ASE generated from an EDFA. The SMF that carries the ASE light is coupled to one end of the FMF using free-space fiber coupler and offset launch technique so as to generate both the LP_{01} and LP_{11} mode. The offset axis is aligned with the fast axis of the FMF so as to generate LP_{11} mode. The power distribution between LP_{01} and LP_{11} mode is determined by the offset distance, and we adjust the offset so that LP_{01} and LP_{11} mode has equal power. The other end of the FMF is coupled to another SMF using

free-space fiber coupler that is connected to the high resolution OSA. The offset axis is also aligned with the fast axis of the FMF and the offset distance is adjusted where both LP_{01} and LP_{11} mode can be received and the optical power reaches maximum.

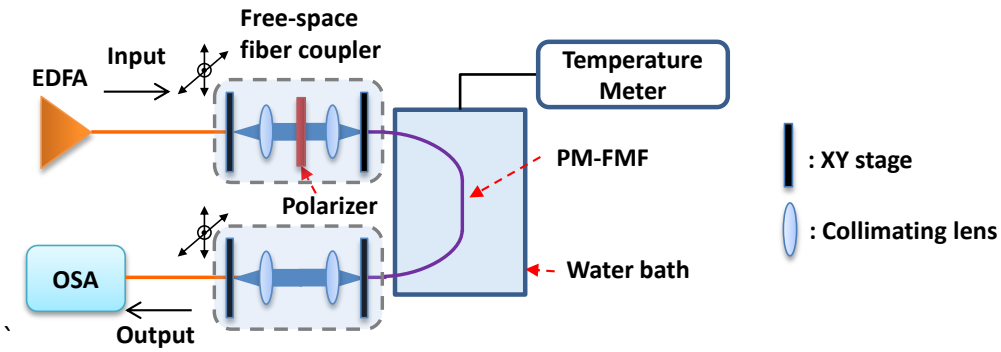

Fig. 4.6. Schematic diagram of a fiber interferometer temperature sensor based on the intermodal interference between LP_{01} and LP_{11e} modes in a PM-FMF. PC: polarization controller.

4.3.3.3 Experimental demonstration

❖ *PM-FMF based sensors*

We first measure the temperature dependence of the 10-meter intermodal PM-FMF sensor. To characterize the performance of intermodal interferometer sensor, we also use the 10-m PANDA fiber (PM2000, THORLABS) as the fiber under test (FUT). With the same temperature range and step as in Section 4.3.2, we measure the transmission spectra of the PM-FMF intermodal interferometer under different temperatures, some of which are as shown in Fig. 4.7(a). The wavelength shift of the minima as a function of temperature is shown in Fig. 4.7(b). The input polarization is aligned with the slow- (x-pol) or fast-axis (y-pol) of the PM-FMF at the input port by a film linear polarizer which is placed between the two collimating lenses in the free-space fiber coupler. The measured temperature coefficient is 0.12 nm/°C for LP_{01x}-LP_{11x} mode and 0.09 nm/°C for LP_{01y}-LP_{11y} mode, respectively. Compared with the polarimetric interferometer based on the same PM-FMF, intermodal interferometer shows less sensitivity whose temperature coefficient is only 7% (LP_{01x}-LP_{11x}) and 5% (LP_{01y}-LP_{11y}) of that of the polarimetric interferometer (LP_{01x}-LP_{01y}). This much reduced sensitivity is because the modal birefringence is much larger than that the

polarimetric birefringence in a PM-FMF, $B_{ij} \gg B_{xy}$. The temperature coefficient also change signs for the polarimetric and intermodal interference. The low temperature sensitivity implies that the PM-FMF based intermodal interferometer may not be attractive for temperature sensing.

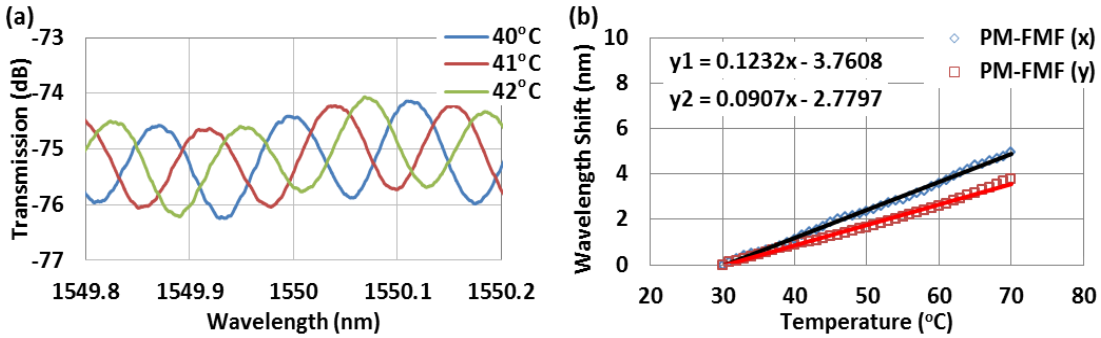

Fig. 4.7. (a) Measured output power spectra (smoothed over 0.02 nm) of the 10-meter PM-FMF intermodal interferometer under different sensor temperatures, and (b) wavelength shift of the transmission minimum around 1550 nm against temperature. y1and y2 are the linear curve fittings for x- and y-polarization, respectively.

We continue to measure the strain dependence of a 1-meter intermodal PM-FMF sensor with 0.6-meter sensing length. With the same strain step as in Section 4.3.2, we measure the transmission spectra of the PM-FMF intermodal interferometer from 0 με to 5000 με with a step size of 500 με, and some of which are as shown in Fig. 4.8(a). The wavelength shift of the minima as a function of strain is shown in Fig. 4.8(b). The input polarization is aligned with the slow- (x-pol) or fast-axis (y-pol) of the PM-FMF at the input port by a film linear polarizer which is placed between the two collimating lenses in the free-space fiber coupler. The measured strain coefficient is 2.0 pm/ με for LP_{01x}-LP_{11x} mode and 1.0 pm/ με for LP_{01y}-LP_{11y} mode, respectively.

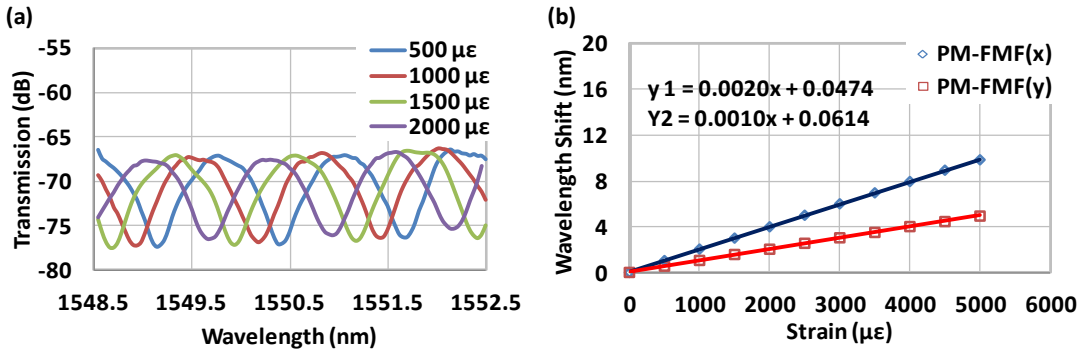

Fig. 4.8. (a) Measured output power spectra (smoothed over 0.1 nm) of the 1-meter PM-FMF intermodal interferometer under different sensor strains, and (b) wavelength shift of the transmission minimum around 1550 nm against strain. $y_1$and y_2 are the linear curve fittings for x- and y-polarization, respectively.

❖ *TMF based sensors*

On the other hand, we replace the PMF with a custom-designed circular-core two-mode fiber (c-2MF) as the FUT. It has a step-index profile between core and cladding and supports five spatial modes, LP_{01}, LP_{11} (including LP_{11a} and LP_{11b}) mode at 1550 nm. To generate the interference between two different modes, we use a mode converter (MC) to convert pure LP_{01} mode into a combination of LP_{01} and LP_{11} modes. The MC is constructed by pressing the TMF against a metallic slab with a surface grating and has a nominal conversion ratio of 50%, exciting both the LP_{01} and LP_{11} mode equally into the TMF.

We first measure the temperature dependence of the 8.6-meter intermodal TMF sensor and some of the measured power spectra around 1550 nm are shown in Fig. 4.9(a). The temperature is measured from 30 °C to 95 °C with a step size of 5 °C. Fig. 4.9(a) shows the transmission spectrums at 25℃ (room temperature), 30 ℃, 35 ℃ and 40 ℃, with spacing between two adjacent transmission minimums is 0.26 nm. Then we obtain the wavelength shift-temperature curve, which is shown in Fig. 4.9(b). The temperature sensitivity is characterized as -0.043 nm/℃, with a good linear correlation coefficient value R^2 of 0.9979. The heating is repeated for 4 times, and for each time the wavelength shift-temperature data is recorded. The similar performance for the several measurements shows good stability of the TMF sensor.

We can therefore tell that the TMF temperature sensitivity is about two times better than that of FBG sensor and almost the same as that of high sensitivity MMF sensor.

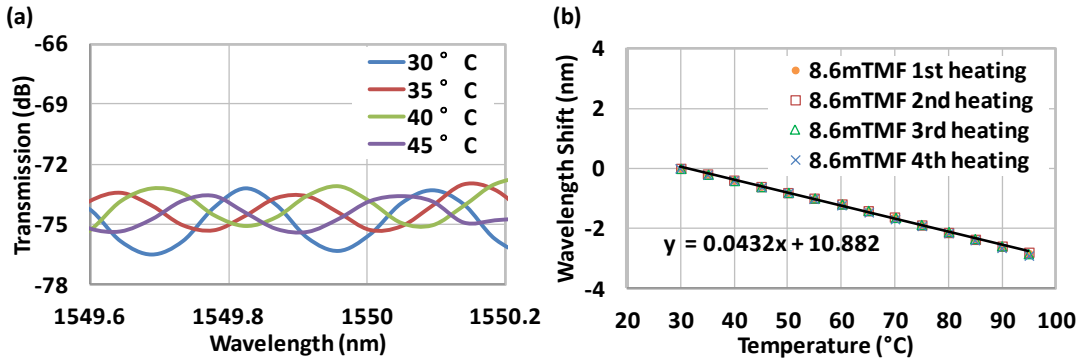

Fig. 4.9. (a) Measured output power spectra (smoothed over 0.02 nm) of the 8.6-meter TMF intermodal interferometer under different sensor temperatures, and (b) wavelength shift of the transmission minimum around 1550 nm against temperature. y is the linear curve fittings for the 8.6-meter TMF.

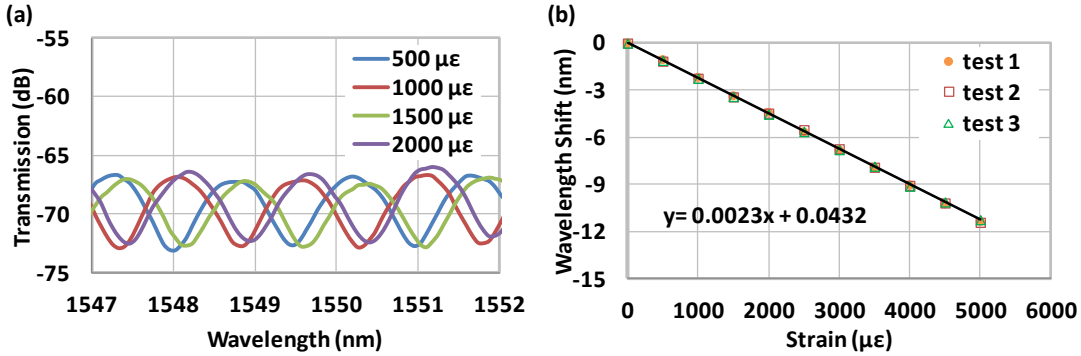

Fig. 4.10. (a) Measured output power spectra (smoothed over 0.1 nm) of the 1.5-meter TMF intermodal interferometer under different sensor strains, and (b) wavelength shift of the transmission minimum around 1550 nm against strain. y is the linear curve fittings for the 1.5-meter TMF.

We continue to measure the strain dependence of a 1.5-meter intermodal TMF sensor with 0.6-meter sensing length. During the measurement, we rotate the polarizer to maintain maximum extinction ratio for the interference spectrum. Fig. 4.10(a) shows transmission spectrums at 500 με, 1000 με, 1500 με and 2000 με. We then apply strain continuously from 0 to 5000 με with a step size of 500 με, and the results are shown in Fig. 4.10(b). The measured TMF wavelength shift-strain coefficient is -0.0023 nm/με, with a good linear correlation coefficient value R^2 of

0.9998. The elongation is repeated for 3 times, and for each time the wavelength shift-strain data is recorded. The similar performance for the several measurements shows good stability of the TMF sensor. TMF strain sensitivity is comparable with that of PM-PCF based high sensitivity interferometer sensor.

4.3.4 Discussions and comparison

To compare the performance and sensitivity for the sensors mentioned above, we put all the temperature curves together and the temperature sensors are shown in Fig. 4.11. For polarimetric sensor, the measured temperature coefficient is -1.25 nm/°C for PM-SMF and -1.72 nm/°C for PM-TMF, respectively. PM-FMF based SLI sensor shows better temperature sensitivity as the temperature coefficient is about 1.4 times that of conventional PMF based SLI sensor. The reason for improved sensitivity of PM-FMF fiber is that it has smaller polarimetric birefringence than conventional PMF. For intermodal sensor, we can see that temperature sensitivity of the TMF is only 3.5% of that of PM-SMF and 35% of that of PM-TMF, which makes TMF based sensor very attractive because of its relatively low sensitivity to temperature perturbation.

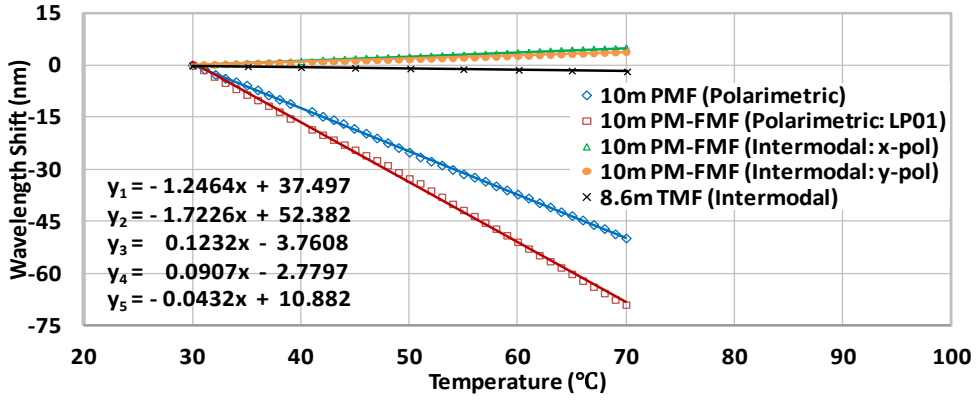

Fig. 4.11. Wavelength shift of the transmission minimum against temperature, y_1, y_2 , y_3, y_4 and y_5 are linear fitting curves for TMF, PM-SMF (polarimetric), PM-TMF (polarimetric:LP01mode), PM-TMF (intermodal: x-polarization), PM-TMF (intermodal: y-polarization), TMF (intermodal), respectively.

Similarly, we put all the strain curves together and the strain sensors are shown in Fig. 4.12. Result shows that TMF has strain sensitivity comparative to PMFs, which

is 2.0 pm/με for both PM-SMF and PM-TMF; meanwhile, TMF is much cheaper than PMFs and also fluctuations of temperature would induce an error as low as 30 με/℃. We note that in Fig. 4.12, PM-FMF is characterized between LP_{01x} and LP_{11bx}, and has highest strain sensitivity among all the combinations (0.36 pm/ με for LP_{01x} /LP_{11ax}, 0.60 pm/ με for LP_{01y}/LP_{11ay} and 1.04 pm/ με for LP_{01y}/LP_{11by}).

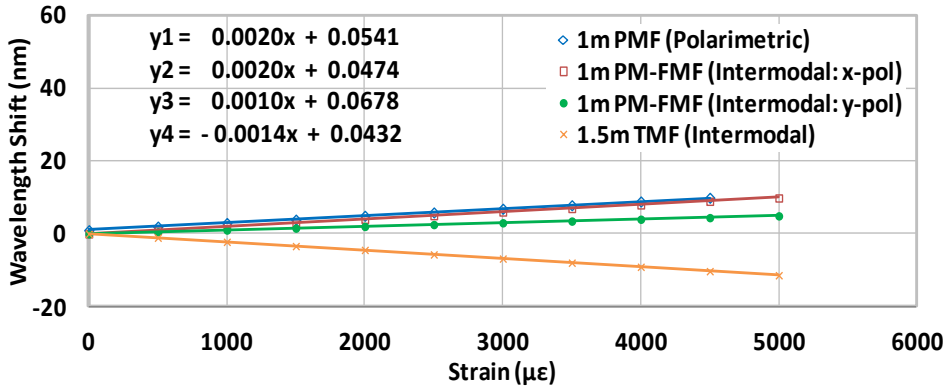

Fig. 4.12. Wavelength shift of the transmission minimum against strain y_1, y_2 , y_3 and y_4 are linear fitting curves for TMF, PM-SMF (polarimetric), PM-TMF (intermodal: x-polarization), PM-TMF (intermodal: y-polarization), TMF (intermodal), respectively.

In Conclusion, compared with the polarimetric interferometer based on the same PM-FMF, intermodal interferometer shows less sensitivity whose temperature coefficient is only 7% (LP_{01x}-LP_{11x}) and 5% (LP_{01y}-LP_{11y}) of that of the polarimetric interferometer (LP_{01x}-LP_{01y}). The low temperature sensitivity implies that the FMF based intermodal interferometer may not be attractive for temperature sensing. On the other side of strain sensing, the result shows that the strain coefficient is as high as 1.4 pm/με for an intermodal interferometer sensor based on TMF, which is comparable with a special-designed high sensitivity PM-PCF based strain sensor (~2.8 pm/με) [157]. Therefore, it is reasonable to expect that FMF based intermodal interferometer can also be a promising solution for highly sensitive strain sensor with low temperature sensitivity.

4.4 Few-mode fiber based distributed optical sensors

4.4.1 Theoretical fundamentals

SBS has been well known and studied for SMFs. For FMFs, because many spatial modes can be involved, the SBS effect can take place not only in a same spatial mode but also between different spatial modes, which is denoted as the intra- and inter-modal SBS. As a generalized form, we define the concept SBS in a FMF as follows, when a (pump) light in wavelength λ_1 and mode i is propagating through a FMF, due to the interaction between the light photons and acoustic phonons, a fraction of the light will be backscattered. The scattering effect can happen spontaneously (known as the spontaneous Brillouin scattering) in which the acoustic phonons are generated from thermal fluctuations. By contrast, as the optical power gets higher, the acoustic phonons are generated mostly from the optical field of the propagating light, leading to a stimulated effect which is known as the SBS. In both cases, the scattered light will experience a frequency downshift (Stokes) due to the Doppler shift associated with the moving grating by the acoustic wave, which depends on the acoustic velocity and is given by [6]

$$\nu_B = \frac{2n_i V_a}{\lambda_1} \sin\left(\frac{\theta}{2}\right) \tag{4.8}$$

where ν_B is the Brillouin frequency shift (BFS), n_i is the effective refractive index (ERI) of mode i, V_a is the effective velocity of the acoustic wave, and θ is the angle between the pump and Stokes fields. For forward direction ($\theta = 0$) the frequency shift ν_B vanishes as $\nu_B = 0$, and for backward direction ($\theta = \pi$) the frequency shift ν_B is maximum,

$$\nu_B = \frac{2n_i V_a}{\lambda_1} \tag{4.9}$$

Since the forward and backward direction are the only relevant directions in a SMF, the SBS only occurs in the backward direction in SMFs, although spontaneous Brillouin scattering can occur in forward direction due to the guided nature of acoustic waves, which is known as the guided-acoustic-wave Brillouin scattering. Furthermore, when another pump light is counter-propagating along the fiber, which is in the same mode *i* and is frequency downshifted from the pump light by ν_B, the

counter-propagated light will be amplified which is called the Brillouin gain, and an acoustic wave (or so-called BDG) is also built up. This effect is commonly known as the intra-modal SBS. If the counter-propagating light with wavelength λ_2 is sent through another mode j, inter-modal SBS may happen. The frequency shift $\nu_{B,ij}$ will be related to the ERIs of both spatial modes based on the phase-matching condition, given by [153]

$$\nu_{B,ij} = V_a\left(\frac{n_i}{\lambda_1}+\frac{n_j}{\lambda_2}\right)\approx\frac{V_a}{\lambda_1}\left(n_i+n_j\right) \tag{4.10}$$

where n_j is the effective refractive index of mode *j*. Time-domain analysis on the gain spectrum can provide information on the distributed ERI. In addition, if we generate intra-modal SBS with two counter-propagating pump waves in mode *i* and send a probe wave of wavelength λ_3 through another mode *k*, it will be reflected by the BDG with the same frequency shift ν_B if the phase matching condition is satisfied, given by [154]

$$\nu_B = \frac{2n_iV_A}{\lambda_1}=\frac{2n_kV_A}{\lambda_3}=\frac{2\left(n_i-\Delta n_{ik}\right)V_A}{\lambda_1-\Delta\lambda_D} \tag{4.11}$$

$$\Delta\lambda_D = \lambda_1-\lambda_3=\frac{n_i-n_k}{n_i}\lambda_1=\frac{B_{ik}}{n_i}\lambda_1 \tag{4.12}$$

where n_k is the effective refractive index of mode *k*, B_{ik} is the modal birefringence between mode *i* and *k*, $B_{ik}=\Delta n_{ik}=n_i-n_k$. Eqs. (4.11)-(4.12) assume that the ERI is constant for all the wavelengths of pump, probe and BDG reflection. More precise derivations considering the wavelength dependence of ERI have been given in [155].

Depending on the content of analysis there are two major schemes of BOTDA, (1) analyzing the BGS by using a counter-propagating two-wave configuration, and (2) analyzing the BDG by using a three-wave configuration [158]. Because the ERI of modes are temperature and strain dependent, we can fabricate a Brillouin temperature or strain sensor based on the BOTDA technique. Using temperature as

an example, we can fabricate a sensor based on the BGS scheme in which the BFS is used as the indicator of temperature. For intra-modal SBS, the temperature dependence of BFS can be derived from Eq. (4.10) and is given by

$$\frac{d\nu_B}{dT} = \frac{2}{\lambda_1}\left(V_a \frac{dn_i}{dT} + n_i \frac{dV_a}{dT}\right) \tag{4.13}$$

and for inter-modal SBS, the temperature dependence of BFS can derived from Eq. (4.11) and is given by

$$\begin{aligned} \frac{d\nu_{B,ij}}{dT} &= \frac{1}{\lambda_1}\left(V_a \frac{dn_i}{dT} + n_i \frac{dV_a}{dT}\right) + \frac{1}{\lambda_2}\left(V_a \frac{dn_j}{dT} + n_j \frac{dV_a}{dT}\right) \\ &\approx \frac{1}{\lambda_1}\left[V_a \frac{d\left(n_i + n_j\right)}{dT} + \left(n_i + n_j\right)\frac{dV_a}{dT}\right] \end{aligned} \tag{4.14}$$

We can also fabricate a temperature sensor based on the BDG scheme, in which the wavelength shift of BDG reflection is used as the indicator. The temperature dependence of wavelength shift can be derived from Eq. (4.12) and is given by

$$\frac{d\Delta\lambda_D}{dT} = \frac{\lambda_1}{n_i^2}\left(n_i \frac{dB_{ik}}{dT} - B_{ik}\frac{dn_i}{dT}\right) = \frac{\lambda_1}{n_i^2}\left(n_k \frac{dn_i}{dT} - n_i \frac{dn_k}{dT}\right) \tag{4.15}$$

From Eqs. (4.13)-(4.15) we can see that the perturbation effects can be translated into a change of the BFS or the wavelength of BDG. Therefore, characterizing the SBS effect (BGS or BDG) in a FMF is a feasible approach to realize distributed fiber sensing.

If the temperature and strain responses are much different for the two spatial modes (i and j), we are able to discriminate both effects by measuring the detuning of BFS in each mode, given by

$$\begin{pmatrix} \Delta\nu_{B,i} \\ \Delta\nu_{B,j} \end{pmatrix} = H\begin{pmatrix} \Delta T \\ \Delta\varepsilon \end{pmatrix}, H = \begin{pmatrix} B_j & -B_i \\ -A_j & A_i \end{pmatrix} \tag{4.16}$$

where H is the sensitivity matrix, $A_{i(j)}$ and $B_{i(j)}$ are the temperature and strain coefficients for mode $i(j)$, respectively. By solving Eq. (4.16), we can obtain the change of temperature ΔT and strain $\Delta\varepsilon$ as

$$\begin{pmatrix}\Delta T\\ \Delta\varepsilon\end{pmatrix}=\begin{pmatrix}A_i & B_i\\ A_j & B_j\end{pmatrix}^{-1}\begin{pmatrix}\Delta\nu_{B,i}\\ \Delta\nu_{B,j}\end{pmatrix}=H^{-1}\begin{pmatrix}\Delta\nu_{B,i}\\ \Delta\nu_{B,j}\end{pmatrix}=\frac{1}{\det(H)}\begin{pmatrix}B_j & -B_i\\ -A_j & A_i\end{pmatrix}\begin{pmatrix}\Delta\nu_{B,i}\\ \Delta\nu_{B,j}\end{pmatrix} \quad (4.17)$$

where 'det' stands for matrix determinant. Denominator $\det(H)$ in Eq. (4.17) must have significant value in order to achieve high discrimination accuracy.

4.4.2 System configuration

❖ *Parameters for fiber under test (FUT)*

As a proof-of-concept trial of Brillouin distributed sensor we experimentally demonstrate characterization of SBS effect in a FMF. We build a reconfigurable few-mode Brillouin optical time domain analyzer (FM-BOTDA) which can characterize SBS in arbitrary combination of mode pairs, including both the intra- and inter-modal SBS. To realize this functionality, we generate and combine all the supported spatial modes before launching into the FUT. The FUT is a 3-km custom-designed circular-core five-mode fiber (c-5MF). It has a step-index profile between core and cladding and supports five spatial modes, LP_{01}, LP_{11a}, LP_{11b}, LP_{21a} and LP_{21b} mode at 1550 nm.

❖ *Free-space mode multiplexer/ de-multiplexer*

In order to generate SBS in arbitrary spatial modes, the pump or probe wave which is sent through the fundamental mode in the SSMF is converted to one of the supported spatial modes and launched into the c-5MF using a free-space mode multiplexer (MMUX), as shown in Fig. 4.13(a). The MMUX can also be a mode de-multiplexer (MDMUX) if the signal is launched through the opposite direction. To maximize the system flexibility and to make the mode conversion reconfigurable, four LCOS based SLMs are used in the MMUX for mode generation. Unique phase patterns can be programmed onto the SLMs, and the relationship between the SLM

phase patterns and the spatial modes as shown in Fig. 4.13(b). The insertion loss of the mode launcher (ML) is about 1.4 dB for LP_{01} mode and 3.9 dB for LP_{11} mode.

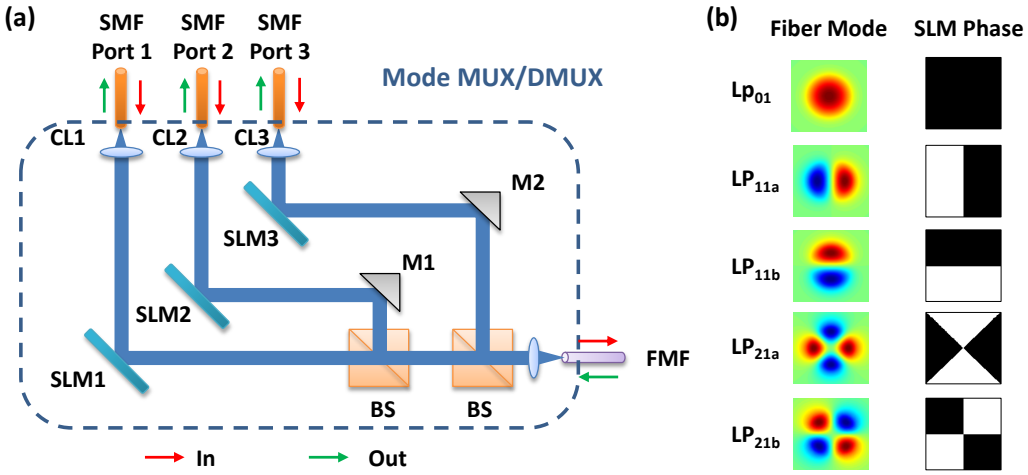

Fig. 4.13. (a) Schematic diagram of a free-space mode multiplexer (MMUX), only one polarization is illustrated (both polarizations are used in experiment). (b) Spatial modes in the 5MF and the corresponding SLM phase patterns. CL1~CL3: collimating lens, M1/M2: turning mirror, BS: non-polarizing beam splitter.

❖ *System configuration of FM-BOTDA*

The setup of our FM-BOTDA is shown in Fig. 4.14. A 1550 nm external-cavity laser (ECL-1) is used as the light source. Continuous-wave (CW) from ECL-1 is divided into three paths by two 3dB single-mode fiber couplers. The signal flow on each path is as follows:

(i) CW light in upper path (pump-1) is modulated by an electro-optic modulator (EOM) driven by a 2-channel arbitrary function generator (AFG), which generates 30 ns Gaussian pulse with 5-kHz repetition rate. After amplification by an EDFA, the pulsed pump wave is then selectively converted to a specific spatial mode, and finally fed into the FUT through a mode multiplexer (MMUX-1).

(ii) CW light in middle path (pump-2) is modulated by an intensity modulator (IM) driven by a RF synthesizer. The IM is biased at null point so that a double-sideband (DSB) signal is obtained (frequency @ $+\nu_F$ and $-\nu_F$). The

DSB signal then passes through a tunable optical band-pass filter (OBPF) to remove lower sideband (ν_F). The single sideband signal is then amplified by an EDFA, selectively converted to a specific spatial mode, and finally fed into the FUT in the opposite direction through another mode multiplexer (MMUX-2). The average launch power into the FUT is 11.7 dBm for pump 1 and 9.6 dBm for pump 2. The launch power of probe wave is 8.2 dBm.

(iii) CW light in lower path (LO1) is used for providing LO to the 6×6 coherent receiver. The measured insertion loss is 3.5 dB for LP01 mode and 6.5 ∕ 7.2 dB for LP11a ∕ LP11b modes, respectively.

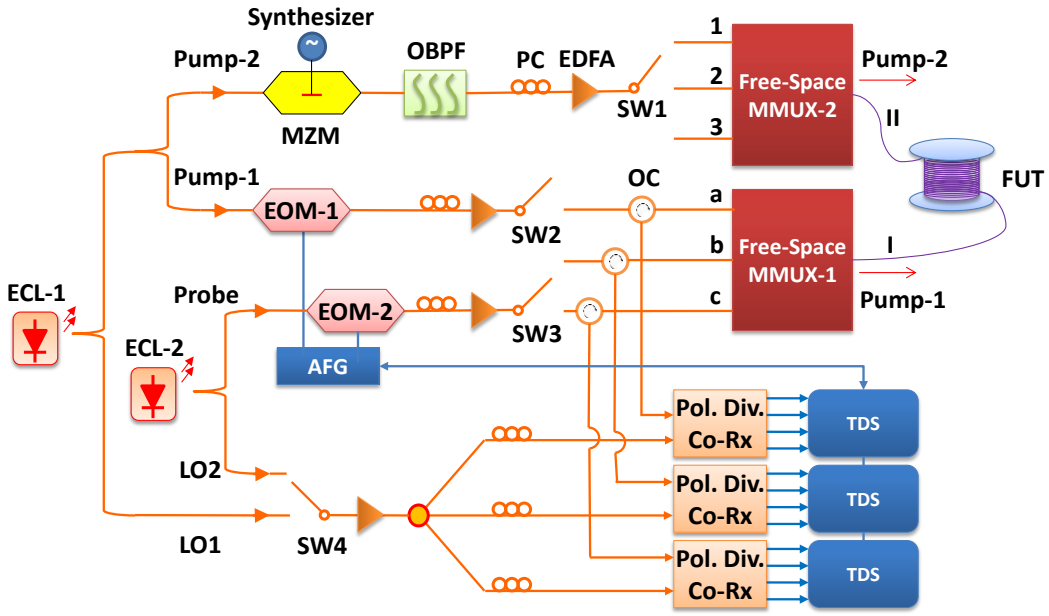

Fig. 4.14. Experimental setup for the proposed few-mode Brillouin optical time-domain analyzer (FM-BOTDA). MZM: Mach-Zehnder modulator; EOM: electro-optic modulator; OBPF: optical band-pass filter; MS: mode stripper; MC: mode converter; TDS: time-domain (sampling) scope.

For BGS measurement, the Brillouin amplified signal in pump-2 is de-multiplexed reciprocally by MMUX-1 onto three paths, and converted back to LP_{01} modes by the subsequent MCs and MSs. The three de-multiplexed optical signals are then directed by three optical circulators (OCs) and fed into a 6×6 coherent receiver. The receiver has 6 optical hybrids and 12 balanced PDs with 3-dB bandwidth of 15 GHz. Finally, the 12 tributaries of electrical signal comprising the in-phase and quadrature

components of all the modes and polarizations are sampled by three Tektronix digital oscilloscopes with sampling rate of 25-GSa/s. The three oscilloscopes are synchronized and triggered by the AFG so that distributed measurement is enabled.

For BDG measurement, we introduce another tunable external-cavity laser (ECL-2) to generate probe wave with wavelength at λ_2. The CW from ECL-2 is divided into two branches: the upper branch is modulated with another EOM driven by the same AFG (30 ns Gaussian pulse, 5-kHz repetition rate) to provide pulsed probe wave. The probe wave is then amplified, converted to LP_{11a} mode, and fed into the FUT in the same direction as pump-1 through MMUX-1. The lower branch (LO2) is used for providing LO to the 6×6 coherent receiver.

The choice of LO depends on which scheme the FM-BOTDA is operating. For BGS scheme LO1 (provided by ECL-1) is used to detect the amplified pump-2 wave, and for BDG scheme LO2 (provided by ECL-2) is used to detect the BDG reflected probe wave. It is also possible to simultaneously detect BGS and BDG providing there are enough coherent receivers. Since the SBS efficiency depends on the state of polarization (SOP) of the two pump waves, we align the SOP of the two pump waves at the input end of pump-1 to maximize the SBS efficiency.

❖ *System configuration of temperature and strain sensing*

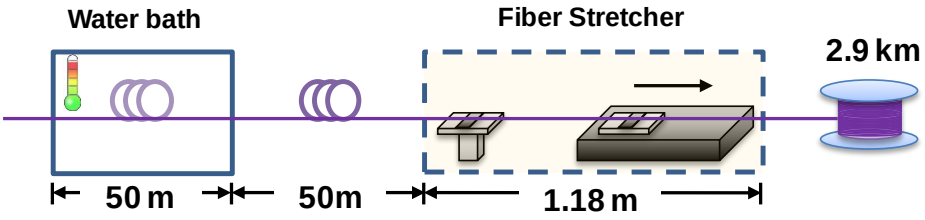

Fig. 4.15. Configuration of the FUT for temperature and strain sensing.

For the experimental setup of the FMF multi-parameter sensor, the FUT is divided into four sections for the simultaneous temperature and strain sensing, as shown in Fig. 4.15. The first section (L_1 = 50 m) is spooled and placed into a water bath with ±0.1 °C tuning accuracy. The second section (L_2 = 50 m) is also spooled but placed outside the water bath for the isolation purpose. The third section (L_3 = 1.18 m) is

pulled straight and fit into a fiber stretcher that can pull the fiber back and forth along a single axis with ±1 μm accuracy, so as to apply proper axial strain. The last section (L_4) contains the remaining part of the FUT, which is spooled together and placed still on the optical bench.

4.4.3 Experimental demonstration

❖ Measurement of Brillouin gain spectra

We first measure the BGS by launching pump-1 and pump-2 (serving as probe) into the FUT. The pump (pump-1) power is 10 mW and the probe (pump-2) power is 1mW. To efficiently generate SBS, we set the center frequency of RF synthesizer v_F at 10.5 GHz ($\approx \nu_B$). The BFS is roughly pre-estimated from spontaneous Brillouin scattering.

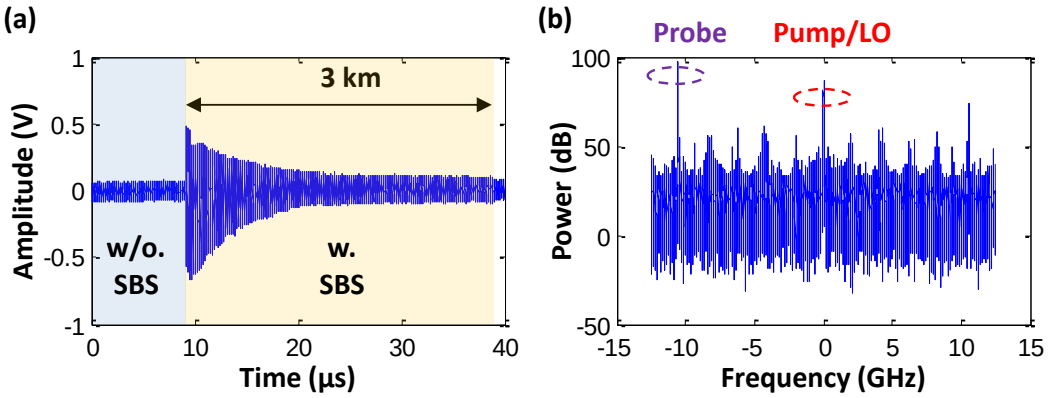

Fig. 4.16. Received signal using heterodyne coherent detection. (a) Time-domain trace of probe signal, (b) Spectrum of probe signal with Brillouin gain (w. SBS). The frequency of probe is offset from pump by -10.52 GHz. Pump power is 10 mW.

In each analysis, we scan over a ± 250 MHz frequency range with a step-size of 2 MHz. The signal trace is recorded twice for each frequency and processed offline with Matlab program. The digital signal processing (DSP) in our program includes the following procedure: (1) IQ imbalance compensation; (2) Fast Fourier Transform (FFT) to get spectrum; (3) Peak search in the vicinity of vF; (4) BGS composition; and (5) Lorentzian curve fitting. The sampling rate of Tektronix oscilloscopes is set at 25GSa/s and the recorded timing length is 40 μs (1 × 106 sample points), which is

equivalent to the roundtrip delay of a 4-km fiber. The spectra of received signal are smoothed over 1MHz (10 points) and averaged 2 times to reduce the noise.

Fig. 4.16(a) shows the timing trace of received probe signal. The peaks in the timing trace are the Fresnel back-reflections of the pump pulse. The first peak is the reflection occurs at the silica-air interface of ML1 (start of FUT), and the last peak is the reflection occurs at the silica-air interface of ML2 (end of FUT). The other minor peaks are the multi-path reflections of the preceding pump pulses. The triangle shape between the two peaks is the amplified probe signal due to the SBS effect. The time trace of probe is then divided into 25-ns segments representing the SBS effect in 2.5-m fiber (5 m roundtrip), which is the maximum achievable spatial resolution limited by the pump pulse width. The spectrum of received signal is shown in Fig. 4.16.(b), where the main peak near $-\nu_F$ (-10.5 GHz) is the probe signal to analyze, the middle peak is the pump/LO, and the other minor peaks are electrical noise and/or harmonics from the oscilloscope. By sweeping the synthesizer frequency and measure the signal power at $-\nu_F$, power spectra in each 2.5-m fiber segment can be composed. The proposed method also makes our analysis immune to most system variations.

Fig. 4.17(a) shows the power spectra without and with Brillouin gain. The two spectra are consecutively measured in a same 40-μs time frame, within which the channel is assumed to be stable. We find that there are noticeable ripples in the composed spectra, which is due to the modal interference caused by the limited modal extinction ratio of the mode launchers (~15 dB). To solve this problem, we subtract the spectrum without Brillouin gain from that with Brillouin gain (w/gain). The proposed differential method provides clean and stable BGS in each fiber segment, as shown in Fig. 4.17(b). The BGS is then fit to a Lorentzian curve, from which the center frequency (= BFS) and width of the gain spectrum are obtained.

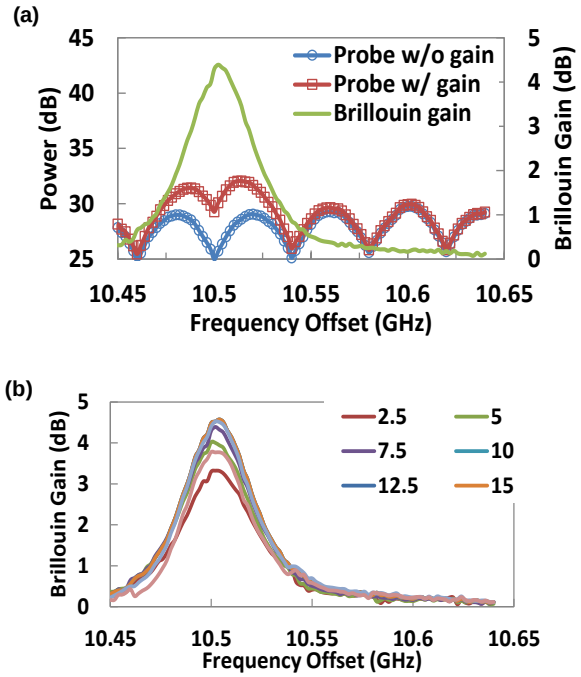

Fig. 4.17 (a) Composed power spectra of the probe signal without (w/o) and with (w/) Brillouin gain, and (b) calculated BGS distribution (before Lorentzian fitting) for 0-20 m FUT.

❖ *Measurement of the FMF multi-parameter sensor based on BOTDA technique*

The experiment is carried out in three steps.

(i) Setp 1: we measure the temperature and strain sensitivity for LP01 mode. Uniform phase pattern is applied onto the SLM. The pump wave has a pulse width of 25 ns with a repetition rate of 2.5 kHz, and is amplified to 5 mW before launching into the FUT. The probe wave is CW and the power is 0.5 mW. In each analysis, the synthesizer frequency is swept from 10.45 to 10.64 GHz with a step-size of 2 MHz for the BGS measurement. For each frequency point, the probe signal is sampled 20 times on the digital oscilloscope and the data is processed offline with MATLAB program. To measure the temperature and strain coefficients, we first benchmark the sensor performance under room temperature (25 °C). We then increase the temperature of water bath from 30 to 90 °C with 10 °C per step, and measure the BGS for the fiber segment in L_2 (in the water bath) on each temperature step using the same

procedure as described above. After that, we apply axial strain to the fiber by gradually moving the linear stage from 0 to 2 mm in the fiber stretcher with 0.25 mm (211.86 με) per step, and measure the BGS again for the fiber segment in L_3 (in the fiber stretcher).

(ii) Setp 2: we measure the temperature and strainsensitivity for LP_{11} mode. Phase pattern with π phase jump is applied onto the SLM. It is known that LP_{11} mode in a circular-core FMF has two-fold degeneracies (LP_{11a} and LP_{11b}).

(iii) Step 3: we investigate the discrimination of temperature and strain using the measured coefficients from the two spatial modes. For a fair comparison we use [159] as reference, and maintain the same accuracy of 0.1 MHz in all the BFS measurements for both spatial modes.

4.4.4 Results and discussions

❖ *Temperature & strain response of BGS*

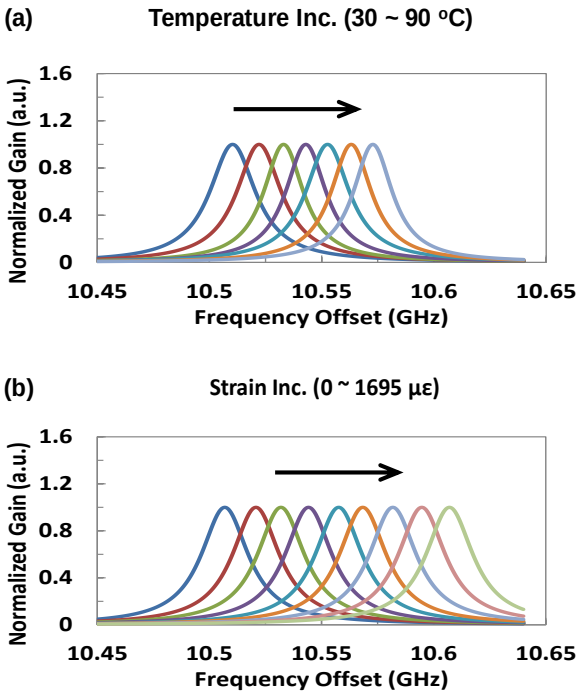

Fig. 4.18. Measured BGS (after Lorentzian fitting) when (a) temperature is increased, or (b) strain is increased. Pump & probe is launched through LP_{01} mode.

Firstly, we measure the temperature and strain sensitivity for LP_{01} mode and the temperature & strain response of BGS (after Lorentzian fitting) for LP_{01} are shown in Fig. 4.18, respectively. As we can see, the BGS moves to the higher frequency as the temperature or strain increases. Since the fiber length in L_3 (1.18 m) is shorter than the spatial resolution (2.5 m), we notice that the BGS measured at L_3 splits to a dual-peak shape as the strain increases. The left peak remains at the same frequency, which is the BGS for the fiber that has no axial strain. The right peak moves to the higher frequency as the strain increases, which is BGS of fiber that has axial strain.

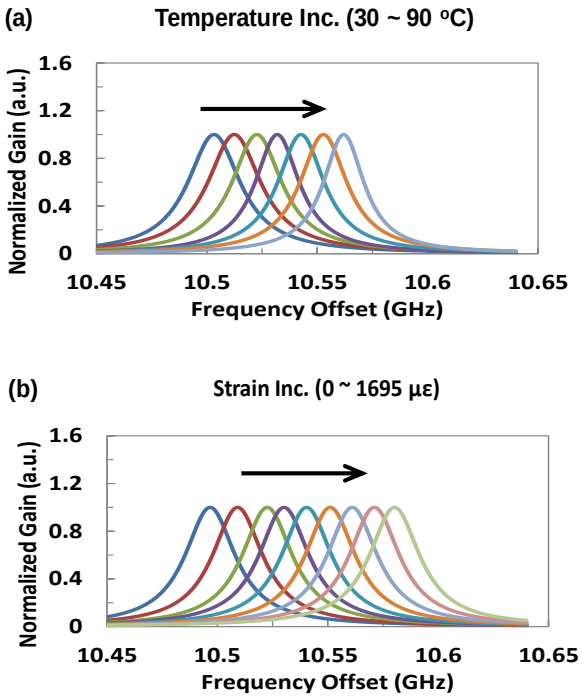

Fig. 4.19. Measured BGS (after Lorentzian fitting) when (a) temperature is increased, or (b) strain is increased. Pump & probe is launched through LP_{11} mode.

Because there is no noticeable difference in the sensing performance, we choose to show only the result of the odd LP_{11} mode (LP_{11a}). Following the same procedure as for LP_{01} mode, we measure the BGS whilst increasing the temperature or strain and the temperature & strain response of BGS (after Lorentzian fitting) for LP_{11} are shown in Fig. 4.19, respectively.

❖ *Temperature & strain response of BFS*

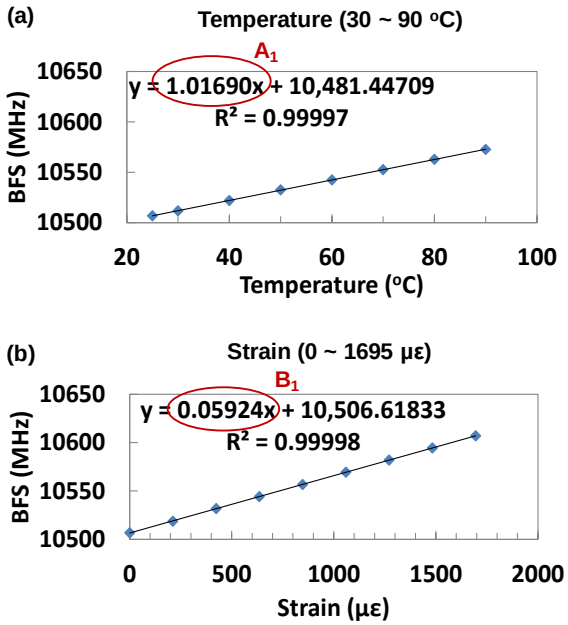

Fig. 4.20. Measured Brillouin frequency shift as a function of (a) temperature and (b) applied strain. Pump/Probe: LP_{01} mode.

By analyzing the center frequency of BGS we obtain the BFS for LP_{01} mode, and its relationship with the temperature and strain is shown in Fig. 4.20(a) and Fig. 4.20(b). By linear fitting the data, we obtain the temperature and strain coefficients for LP_{01} mode, which are A_{01} = 1.01690 MHz/°C and B_{01} = 0.05924 MHz/με, respectively.

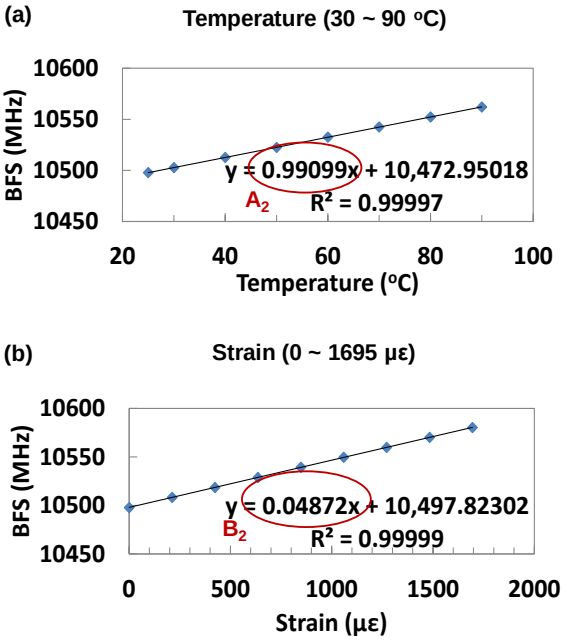

Fig. 4.21. Measured Brillouin frequency shift as a function of (a) temperature and (b) applied strain. Pump/Probe: LP_{11} mode.

Following the same procedure as for LP_{01} mode, we measure the corresponding BFS for LP_{11} mode as a function of temperature and strain is shown in Fig. 4.21(a) and Fig. 4.21(b). Similarly, by linear fitting the experimental data, we obtain the temperature and strain coefficients for LP_{11} mode, which are A_{11} = 0.99099 MHz/°C and B_{11} = 0.04872 MHz/με, respectively.

❖ *Discrimination of temperature and strain*

By putting the standard error ($\Delta\upsilon_B = \pm 0.1MHz$) into to Eq. (4.17), the accuracy of temperature/strain discrimination is 1.2 °C and 21.9 με. Compared with the single-mode PMF [159], the discrimination accuracy for our FMF sensor is slightly worse because of the smaller denominator $\det(H)$, Due to the limitation of our experimental setup, we are not able to generate arbitrary temperature and strain change at the same time. To verify the discrimination capability of the FMF sensor, we choose two temperature and strain settings, (80 °C, 0 με) and (25 °C, 1694.9 με) for analysis. We use the first setting as the origin, so that the second setting can be deemed as with simultaneous temperature and strain change. The measured data of ν_B under the two settings are (10607.0 MHz, 10580.2 MHz) and (10562.9 MHz, 10552.3 MHz) for (LP01, LP11) mode. By putting the value into Eq. (4.17), the estimated temperature and strain changes are ΔT = -54.2 °C and $\Delta\varepsilon$ = 1674.8 με. As can be seen, the estimation error is only (0.8 °C, 20.1 με). The result shows that our proposed FMF sensor has good reliability and accuracy for the discrimination of temperature and strain.

4.5 Conclusions

In this chapter, we review our recent progress in the design and fabrication of few-mode fiber based optical sensors. Firstly, we characterize the performance of discrete optical sensor based on interferometer structure. The first kind is polarimetric interferometer sensor utilizing the mode beating between the polarizations (x and y), and its wavelength shift of the interfering transmission spectrum against temperature and strain (sensitivity against temperature and strain) is characterized as -1.72 nm/°C and 24.5 pm/με in a PM-FMF. The second kind is

intermodal interferometer sensor utilizing the mode beating between the spatial modes (LP_{01} and LP_{11}), and its sensitivity against temperature and strain is characterized as -0.043 nm/℃/ and -0.0023 nm/με in a TMF. The proposed TMF intermodal interferometer sensor exhibits great potential due to good interfering visibility, good linearity, high sensitivity, and low cost.

After that, we continue to introduce the concept of FMF based distributed sensors. We demonstrate efficient generation of BDG in a FMF using two counter propagating pump waves in LP_{01} mode and a probe wave in LP_{11} mode. Combined with coherent detection and optical time-domain analysis, we propose a unique FMF based multi-parameter optical fiber sensor for distributed measurement of temperature and strain. We launch a pump and a probe signal through specific linearly-polarized modes into a FMF, and monitor the BFS in each mode. By analyzing the temperature and strain coefficients of the BFS of the two lowest order (LP_{01}, LP_{11}) modes, discrimination of temperature and strain are successfully demonstrated, with an accuracy of 1.2 °C and 21.9 με.

In conclusions, we have introduced several novel techniques for FMF based optical sensors and reviewed their recent progress. With the availability of high reliability few-mode devices and advance of fiber-optic technology such as SDM and coherent detection, FMF may have great potential in future fiber sensing systems.

5 Complex Imaging via Coherent Detection

5.1 Introduction

Optical fibers supporting multiple spatial modes have recently undergone an abundance of renewed interest, evidenced by the increased use of few-mode and multimode fibers for high-speed telecommunications [76] and the use of highly multimode fibers for endoscopic medical imaging [160]. Meanwhile, the technique of SDM can provide a way to increase the information capacity of a single fiber and the large modal area of these fibers is beneficial in alleviating detrimental nonlinear effects and reducing the chance of fiber damage, respectively. This results in a need to accurately characterize the modal propagation in such fibers. The development of reliable and accurate techniques to investigate in detail the modal content of multimode fibers has thus become a topic of great interest.

In recent years many techniques have been developed to measure the modal content of few mode fibers. For telecommunications applications, this has been achieved in a number of ways including selective mode launch [161-162], modal weight solvers [163] and time of flight [164] based on interferometry. In above cases it is assumed that the underlying propagation modes of the fiber are known, and that minor deviations from these will simply result in mode-coupling or slight variations in time delay. Another technique originally developed by Nicholson et al. [165] is called Spatial and Spectral (S2) imaging technique, which is based on both spatially and spectrally resolving the image of the output of the fiber under test without prior detailed knowledge of the fiber properties. For medical imaging applications, such characterization has been achieved by scanning a diffraction limited Gaussian spot across the input facet of a fiber and then using a reference beam, transported by a separate optical path, to produce interferometric images of the fiber facet on charge-coupled device (CCD) [166] or a single-pixel detector [167]. In [166], a two-dimensional heterodyne detection technique based on the frequency-synchronous detection method is demonstrated for full-field optical coherence tomography, which detects the in-phase and quadrature components of the heterodyne signal simultaneously, offers the advantage of phase-drift

suppression in interferometric measurement. However, the paper only measures amplitude profiles, lacking in phase characterization. In [167], the paper measures amplitude and phase images of a fiber facet in two orthogonal polarizations using a single-pixel detector and a phase-only LCOS SLM without using a separate reference beam or a CCD. The main drawback of this technique is speed, as each 29 × 29 phase image takes about 20 min to capture; also, the quality of the phase image is not ideal [168].

Therefore, we propose and implement a novel method to recover both amplitude and phase images and coherently detect the in-phase and quadrature components of the heterodyne signal simultaneously with a pair of CCD cameras. In this way, both amplitude and phase mode patterns for fundamental and higher-order modes transmitted in optical fibers could be characterized. In this chapter, we first introduce the motivations and review current technologies of complex imaging. In Section 5.2, we give the fundamentals of our proposed complex imaging technique including the principles and theoretical algorithms. In Section 5.3, we introduce the system configuration, digital signal processing procedures of complex imaging, and then demonstrate mode fields in the far-field and near-field of a two-mode fiber using complex imaging technique, including theoretical fundamentals, simulation results for comparison. In Section 5.4, we use our proposed imaging technique for fiber characterizations. We firstly characterize mode patterns of pure fundamental mode and higher-order modes in FMFs as a validation of our imaging method. Next our method is also applied to mode decomposition and modal content analysis of an arbitrary mixed mode pattern. Finally, we sweep the input wavelength and measure differential mode delay (DMD) in FMFs.

5.2 Fundamentals of complex imaging

The detection technique of our proposed complex imaging could be regarded as free-space homodyne detection, which is based on coherent detection technique. Coherent detection technique has already been widely employed in optical fiber transmission for ages that is realized by six-port hybrid devices. Using a six-port 90° hybrid for signal detection and analysis has been practiced in RF domain for decades

[32-33], and its application to single-carrier and OFDM coherent optical systems can be also found in [31, 111]. Correspondingly, we could apply the detection technique to free-space and six-port hybrid device could be replaced by our proposed free-space hybrid-receiver.

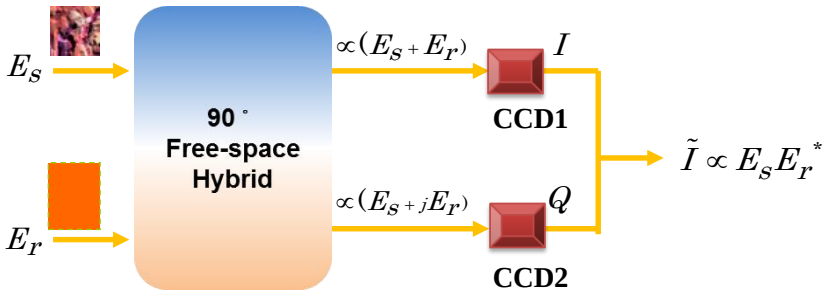

Fig. 5.1. Conceptual diagram of free-space homodyne coherent detection. Es: Incoming Signal; Er: Interfering Reference; CCD: Charge-Coupled Device; I (Q): Inphase (Quadrature) component of the complex signal received from CCD1 (CCD2); $\tilde{I}$: Complex Signal.

As shown in Fig. 5.1, free-space homodyne coherent detection uses a free-space hybrid and a pair of CCDs. The main purposes of coherent detection are (i) to linearly recover I components and Q of the incoming signal, and (ii) to suppress or cancel the common mode noise. In what follows, in order to illustrate its working principle, we will perform an analysis of coherent detection via free-space hybrid receiver assuming ideal condition for each component shown in Fig. 5.1.

The purpose of the two output ports of the 90° optical hybrid is to generate a 90° phase shift between I components and Q. Ignoring imbalance and loss of the optical hybrid, the output signals I and Q can be expressed as

$$I_I=(E_s+E_r)(E_s+E_r)^*=|E_s|^2+|E_r|^2+2\mathrm{Re}\{E_sE_r^*\} \tag{5.1}$$

$$I_Q=(E_s+jE_r)(E_s+jE_r)^*=|E_s|^2+|E_r|^2+2\mathrm{Im}\{E_sE_r^*\} \tag{5.2}$$

where $E_s(x,y,t)=A_s(x,y)e^{j(2\pi ft+\varphi_s(x,y))}$, $E_r(x,y,t)=A_r(x,y)e^{j(2\pi ft+\varphi_r(x,y))}$, 'Re' or 'Im' denotes the real or imaginary part of a complex signal, x and y are denoted as the two spatial dimensions of CCD, t is denoted as time, $A_s(x,y)$ and $A_r(x,y)$ are

spatially dependent amplitudes for signal and reference respectively, $\varphi_s(x,y)$ and $\varphi_r(x,y)$ are spatially dependent phases for signal and reference respectively. For simplicity, the CCD detection responsivity is set to unity. If we average I and Q over time, $\overline{I_I} = \frac{1}{4}\left\{A_s{}^2 + A_r{}^2\right\}$, $\overline{I_Q} = \frac{1}{4}\left\{A_s{}^2 + A_r{}^2\right\}$, and the two components from the pair of CCDs can be derived as

$$I_I - \overline{I_I} = 2\mathrm{Re}\left\{E_s E_r{}^*\right\} \tag{5.3}$$

$$I_Q - \overline{I_Q} = 2\mathrm{Im}\left\{E_s E_r{}^*\right\} \tag{5.4}$$

Using the results of Eq. (5.3)and Eq. (5.4), the complex detected signal I consisting of both I components and Q becomes

$$\tilde{I} = I_I + jI_Q = 2E_s E_r{}^* = A_s(x,y)A_r^*(x,y)e^{j\left(\varphi_s(x,y)-\varphi_r(x,y)\right)}. \tag{5.5}$$

From Eq. (5.5), the linear down-conversion process via coherent detection becomes quite clear; the complex product I is in essence a linear replica of the incoming complex signals that is frequency down-converted by a local oscillator frequency. Thus with linear coherent detection as receiver, we obtain the two-dimensional (2-D) complex signals with relative amplitude and phase to the reference. Therefore, the reference beam should be ideally a perfect reference with flat intensity and phase within the interfering area.

5.3 Complex imaging for waveguide laser mode patterns in the near-field and far-field

5.3.1 System configuration

The complex imaging conceptual configuration is shown in Fig. 5.2(a) and experimental setup is shown in Fig. 5.2(b). The laser source is an ECL, amplified by an EDFA. A 2-by-2 coupler is then connected to split the lightwave into two paths: the signal under test and the reference.

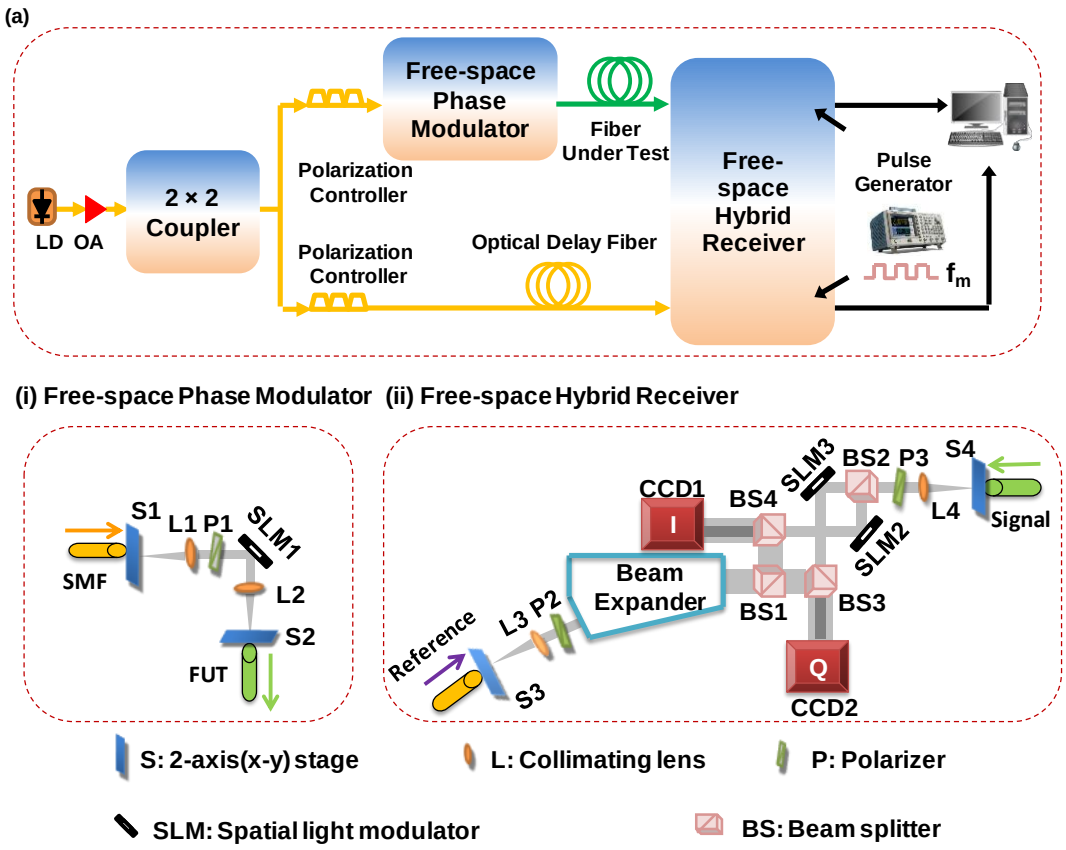

Fig. 5.2. (a) Conceptual diagram of the complex imaging setup. (b) Schematic of the complex imaging setup. (i) Schematic diagram of a Free-space Phase Modulator (FSPM). (ii) Schematic diagram of a Free-space Hybrid Receiver (FSHR). LD: Laser diode; OA: Optical amplifier; CCD: Charge-coupled device.

For the reference path, the beam goes directly to the Free-space Hybrid Receiver (FSHR) through a SSMF, which functions as compensation for different optical path lengths between signal and reference. For the signal path, the optical beam is then coupled into a Free-space Phase Modulator, which is consisted of a 4F system with a SLM operating in reflection mode.The modulated signal is then coupled back into the FUT to generate and transmit the modes we would like to test (Please refer to Section 2.3.2.2 for detailed introduction of SLM).

At the exit of the FUT, the beam goes to the Free-space Hybrid Receiver (FSHR) and is split into two paths: In-phase path (I) and Quadrature path (Q). The signal in the two paths is then combined with the reference separately and fed into two far-field CCDs (Xeneth, Bobcat-320) as I and Q individually. The intensity of the

interfering patterns detected on CCD1 and CCD2 is then collected and recorded for further DSP.

To be noted, (1) the two SLMs (SLM2 and SLM3) in the Free-space Hybrid Receiver (FSHR) are programmed to adjust and generate a 90° phase shift between I and Q components; (2) the two CCDs are synchronized with a frame rate of 20Hz ($f_m = 20Hz$) using a pulse generator; (3) a beam expander (Thorlabs, BE06R/M, 6×) is added to expand the reference beam so that the beam could be regarded as a perfect reference with flat intensity and phase within the interfering area, which is done by using LP_{01} mode in SSMF as reference during the experiment; (4) lengths of the light path for both reference and signal are relatively equal by adjusting the length of the optical delay fiber; (5) lengths of the light path for I and Q are also made equal to achieve stable interference pattern.

5.3.2 Digital signal processing procedures

Conceptual diagram for Digital Signal Processing (DSP) procedures is shown in Fig. 5.3. The intensity of the interference pattern detected on CCD1 is denoted as I, the other one detected on CCD2 is denoted as Q. We collect 400 frames (20 seconds) in succession for better accuracy. The complex imaging signal processing involves (1) compensation for spatial imbalance between I and Q; (2) compensation for power imbalance between I and Q; (3) averaging with time to remove summation intensity of signal and reference; (4) orthogonalization and compensation for the 90° hybrid imperfection following the Gram–Schmidt orthogonalization procedure (GSOP) [169]; (5) phase estimation and recovery for the 2-D complex far-field; (6) performing two-dimensional Fourier Transformation on the 2-D far-field to achieve near-field on the basis of Near-to-Far-Field Transformation.

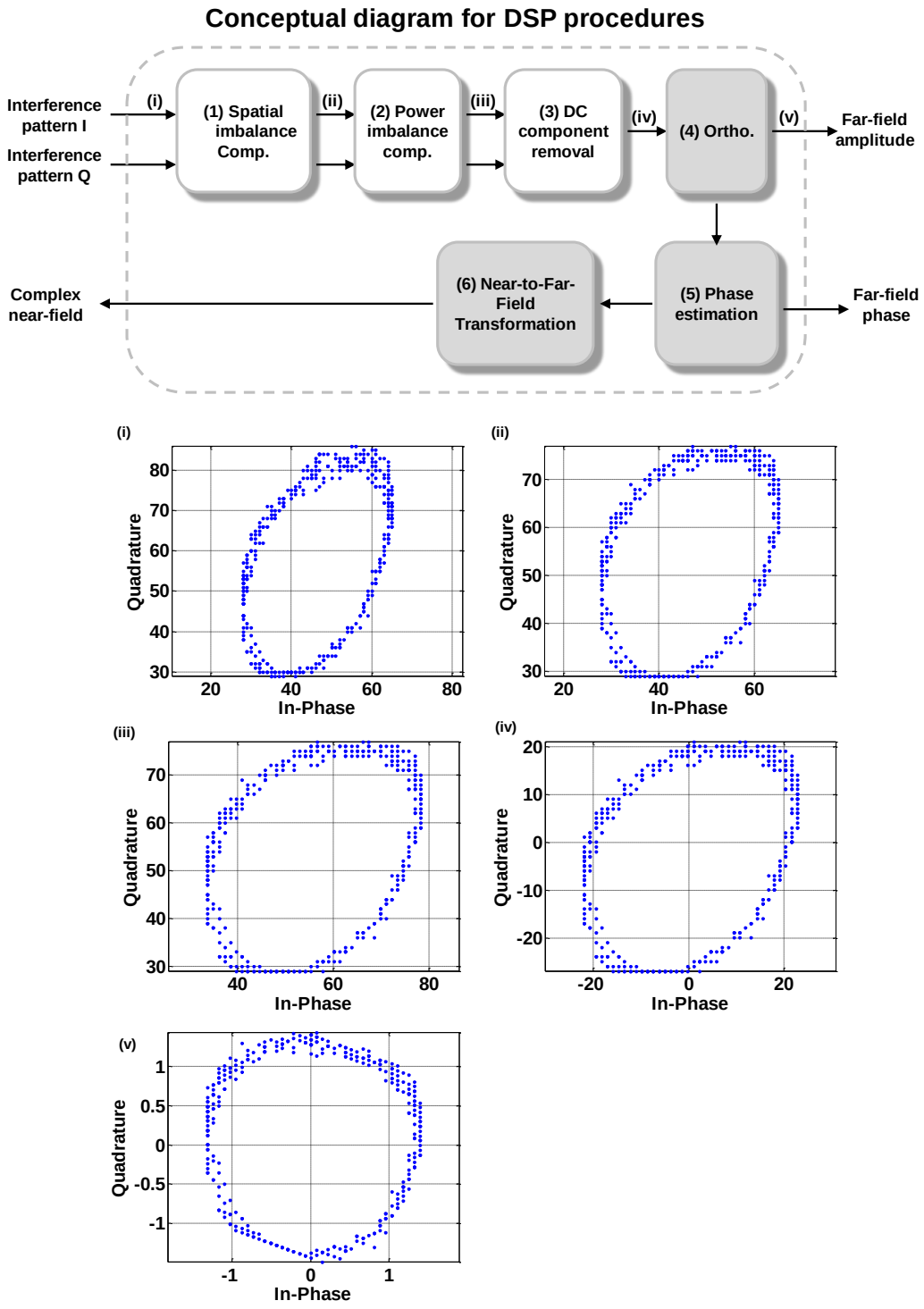

Fig. 5.3. Conceptual diagram for Digital Signal Processing (DSP) procedures, for (i) ~ (v), the experimental constellation diagrams for one single pixel at each step are plotted. Comp.: Compensation; Ortho.: Orthogonalization.

A constellation diagram displays the signal as a two-dimensional X-Y plane diagram in the complex plane at symbol sampling instants, which can be used to recognize the type of interference and distortion in a signal. To better illustrate the

function of each step in the DSP procedures, we plot the constellation diagrams of I and Q at each step, which are denoted as (i) ~ (v) as shown in Fig. 5.3. For the experiment, we generate pure LP01 mode and the FUT is a 10-meter SSMF. The beam profiles typically span at least a 128 x 128 pixel area in far-field, and for the illustration, one single pixel is selected and its constellation diagrams are plotted. We collect 400 frames (the colleting time frame is 20 seconds) in succession for one measurement. From the constellation diagrams (i) ~ (v), we can see that steps (1) ~ (4) correct the main optical impairments and hardware imperfections; transform the ellipse into a circle. The orthogonality for received signals with quadrature imbalance can thus be restored with the amplitudes of the recovered signals normalized correctly [169].

5.3.3 Experimental demonstration

Table 5.1. Parameters for custom-designed c-2MF

Parameter	Unit	Value
Core Diameter	μm	11.9
Cladding Diameter	μm	109
Refractive Index (Core)		1.4519
Refractive Index (Cladding)		1.4440
Effective Refractive Index (LP_{01})		1.4498
Effective Refractive Index (LP_{11})		1.4468
Chromatic Dispersion (LP_{01})	ps/(nm*km)	22.1
Chromatic Dispersion (LP_{11})	ps/(nm*km)	17
Effective Area(LP_{01})	μm^2	94.7
Effective Area (LP_{11})	μm^2	99.9
DMD LP_{01} - LP_{11}	ps/m	3.0
LP_{11} Cut-off Wavelength	μm	2.323
Fiber Loss(LP_{01}, LP_{11})	dB/km	0.26

Following the system configurations in Section 5.3.1 and experimental procedures illustrated in Section 5.3.2, we perform the experiments and obtain complex coherent imaging for waveguide laser mode patterns in the near-field and far-field. The FUT is a custom-designed circular-core TMF (c-2MF). The fiber parameters are summarized in Table 5.1.

5.3.3.1 Mode fields in the near-field

5.3.3.1.1 Theoretical fundamentals

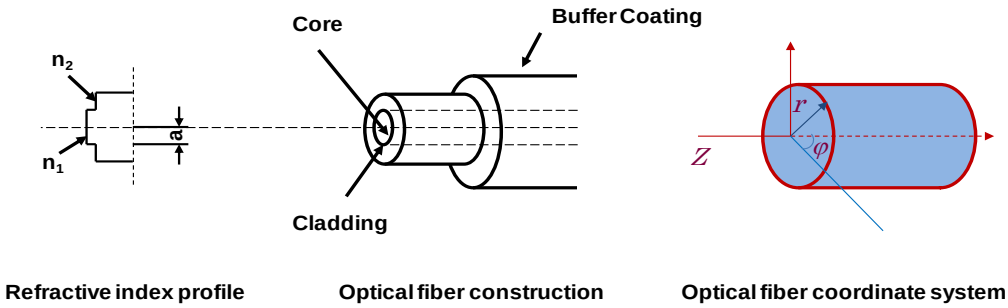

Fig. 5.4. Schematic for a typical step-index optical fiber structure

In homogeneous isotropic medium where the refractive index is n, the propagation constant is β, the wavenumber in vacuum is k_0, and the wave equations could be written as

$$\begin{cases} \nabla^2 E - k_0^2 n^2 E = 0 \\ \nabla^2 H - k_0^2 n^2 H = 0 \end{cases} \text{(Vector Equations)} \qquad (5.6)$$

For a simplification, the cylindrical geometry (homogeneous in the z direction) suggests a formal decomposition of the vector operators into spatial *z*- (longitudinal) and *T*- (transversal) operators and vectors.

A typical step-index optical fiber construction and its refractive index profile are plotted in Fig. 5.4, n_1 and n_2 are denoted as the refractive index of the core and cladding, respectively, and a is denoted as radius of the core. And finally, the solutions for the spatial components are derived by using the method of separation of variables as

$$\begin{cases} E_Z = A_1 J_m(k_c r)\begin{pmatrix} \sin m\varphi \\ \cos m\varphi \end{pmatrix} e^{-j\beta z} \\ H_Z = B_1 J_m(k_c r)\begin{pmatrix} \cos m\varphi \\ \sin m\varphi \end{pmatrix} e^{-j\beta z} \end{cases} \text{(Within the core region)} \qquad (5.7)$$

$$\begin{cases} E_Z = A_2 K_m(a_c r)\begin{pmatrix} \sin m\varphi \\ \cos m\varphi \end{pmatrix} e^{-j\beta z} \\ H_Z = B_2 K_m(a_c r)\begin{pmatrix} \cos m\varphi \\ \sin m\varphi \end{pmatrix} e^{-j\beta z} \end{cases} \text{(Within the cladding region)} \qquad (5.8)$$

, where $k_c^2 = k_0^2 n_1^2 - \beta^2$, $a_c^2 = k_0^2 n_2^2 - \beta^2$; $m = 0,1,2,\ldots$; $J_m(k_c r)$ is Bessel function of the first kind, and the order of the Bessel function is m; $K_m(a_c r)$ is the modified Bessel function of the second kind, and the order of the modified Bessel function is m; A_1, B_1, A_2 and B_2 are unknown constants to be determined by boundary conditions.

The refractive-index difference of practical fiber is of the order of 1%. Moreover index differences of the most important single-mode fibers for optical communication are about 0 .3 ~ 0 .8%. Then we can approximate as $n_2 / n_1 \approx 1$. Since an LP mode is derived by the approximation of $n_2 / n_1 \approx 1$, these LP modes, designated as LP_{lm}, are good approximations formed by exact modes TE, TM, HE and EH. The mode subscripts l and m describe the electric field intensity profile. There are *2l* field maxima around the fiber core circumference and *m* field maxima along the fiber core radial direction [59, 170].

5.3.3.1.2 Simulation results

Based on the theoretical fundamentals in Section above, we perform the simulations of mode fields for the near-field with MATLAB®. In the simulations, the FUT is the c-2MF, with its parameters already given in Table 5.1. The wavelength λ is set at 1550 nm and all the field energies are normalized to 1. For the simulation results, the transverse (x, y) field patterns propagated in the z-direction for the three spatial modes are displayed in Cartesian coordinate system.

Fig. 5.5 shows the electric field amplitude profiles of the guided modes of the c-2MF, and Fig. 5.6 shows the electric field phase profiles of the guided modes of the c-2MF. The total electric field distribution anywhere in a multimode fiber or a few-mode fiber is a superposition of contributions from the different modes. The complex profile depends not only on the optical powers in all the modes, but also on the relative phases, and there can be constructive or destructive interference of different modes at particular locations in the fiber. Both the powers and optical phases are initially determined by the launching conditions, and the relative phases

(and thus the interference conditions) evolve further due to the mode-dependent propagation constants. Therefore, the more or less complicated complex pattern changes all the time, typically with significant changes occurring within a propagation length of well below 1 mm. Also, the relative phases changes with any modifications of the launching conditions, bending or stretching of the fiber, changes of the wavelength or temperature, etc.

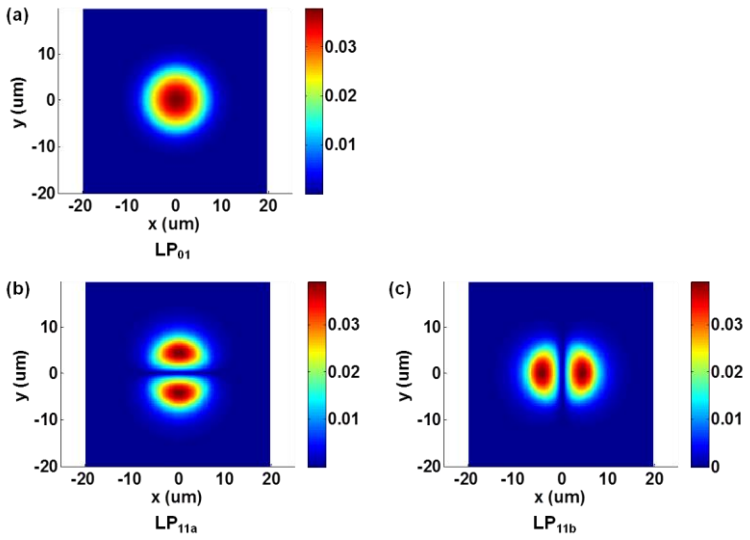

Fig. 5.5. Electric field amplitude profiles for all the guided modes of the c-2MF.

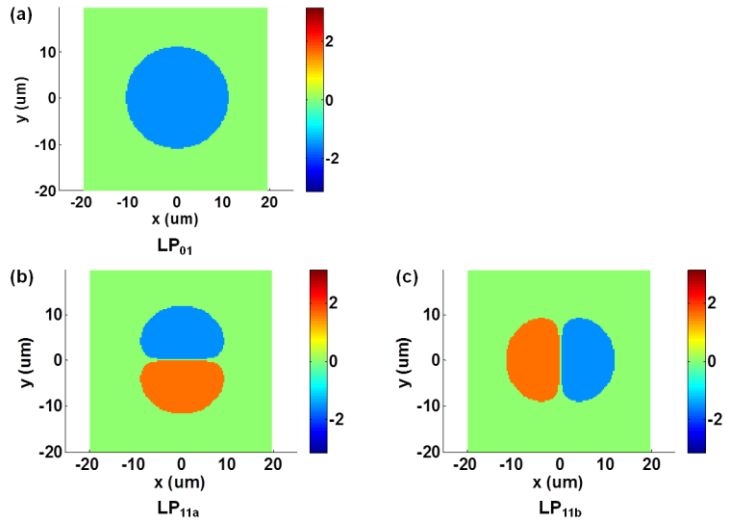

Fig. 5.6. Electric field phase profiles for all the guided modes of the c-2MF. Light green areas in the phase graphs indicate regions where the field intensity is below 5% of the peak field amplitude.

5.3.3.1.3 Experimental results

After we obtain complex mode field in the far-field, we perform the two-dimensional Fourier Transformation on the 2D far-field to achieve near-field on the basis of Near-to-Far-Field Transformation.

Complex mode pattern imaging for the guided modes of the c-2MF (LP_{01} mode and LP_{11} mode) in the near-field are shown in Fig. 5.7. For the experiment, we (1) generate pure LP_{01} mode of the c-2MF with the extinction ratio of 27.1 dB, and the electric amplitude image and phase image of the LP_{01} mode in the near-field are shown in Fig. 5.7(a) and (b), respectively. (2) Generate pure LP_{11} mode of the c-2MF with the extinction ratio of 20.5 dB, and the electric amplitude image and phase image of the LP_{11} mode in the near-field are shown in Fig. 5.7(c) and (d), respectively. The experimental results are consistent with the simulation results in the Section above.

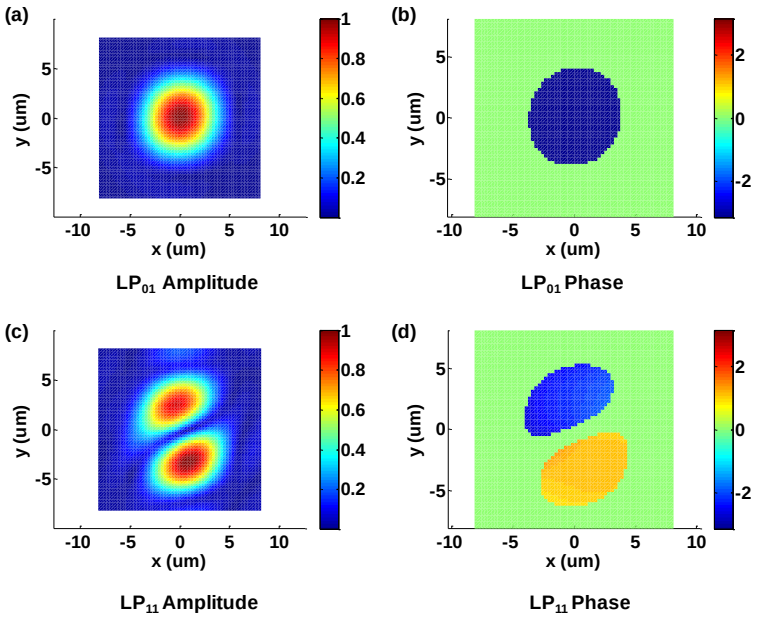

Fig. 5.7. (a) Electric near-field amplitude image for LP01 of the c-2MF. (b) Electric near-field phase image for LP01 of the c-2MF. (c) Electric near-field amplitude image for LP11 of the c-2MF. (d) Electric near-field phase image for LP11 of the c-2MF. Light green areas in the phase graphs indicate regions where the field intensity is below 10% of the peak field power.

5.3.3.2 Mode fields in the far-field

5.3.3.2.1 Theoretical fundamentals

Most of the power of a guided wave is radiated from the fiber end in the form of a free diverging wave beam. Essentially, the fundamental fiber mode is transformed into the fundamental Gaussian beam mode and the second order fiber mode into the second order Gaussian beam mode. The fiber end acts as transmitting dielectric antenna, transforming a guided electromagnetic wave into a freely propagating wave [Neumann 1967a].

❖ ***Far-field radiation pattern***

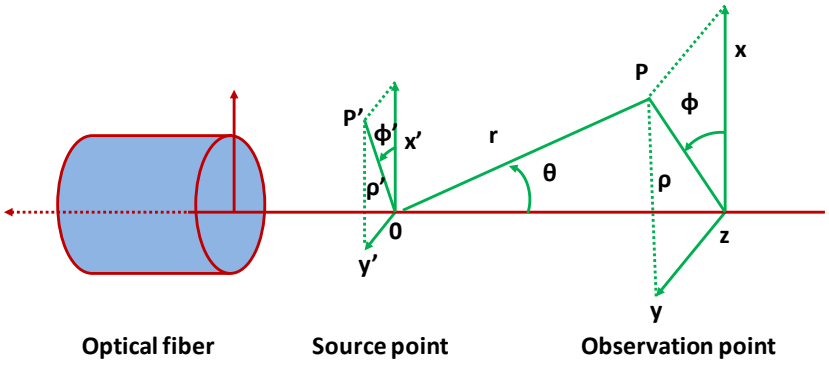

Fig. 5.8. Cylindrical polar coordinates (ρ', Φ', 0) of the source point in the fiber end face and cylindrical polar coordinates (ρ, Φ, z) and spherical coordinates (r, θ, Φ) of the observation point in the field radiated from the fiber end.

We assume the fiber end to be planar and normal to the fiber axis. The fiber endface is assumed to lie in the plane $z = 0$, as shown in Fig. 5.8. The half-space $z > 0$ is filled with air. A LP_{lm} mode is assumed to be incident from $z = -\infty$. We are interested in the radiation field in a point of observation P with Cartesian coordinates (x, y, z) and spherical polar coordinates (r, θ, φ).

Moreover, the transverse field extent in the radiating aperture is assumed to be large as compared to the wavelength. There is then no radiation for polar angles θ much larger than about 10°. In order to get a simple formula for the radiation field,

the distance r of the observation point P from the center of the radiating fiber endface is assumed to be much larger than the Rayleigh distance Z_R of the radiated beam:

$$r \gg Z_R = \pi\omega_G^{\,2} / \lambda \qquad (5.9)$$

where ω_G is the spot size of the fundamental fiber mode. The observation point is then said to be located in the ''far field".

❖ *Relations between the near-field and far-field functions*

With these assumptions, one may apply the simpler scalar diffraction theory for calculating the electric field $E_f(x,y,z)$ at the observation point; this is the so-called far-field radiation pattern

$$E_f(x,y,z) = \frac{j}{\lambda z}\exp(-jkr)\iint E(x',y')\exp[j2\pi(\frac{xx'}{\lambda z}+\frac{yy'}{\lambda z})]dx'dy' \qquad (5.10)$$

where $r = \sqrt{x^2+y^2+z^2}$ is the distance of the observation point from the center of the radiating fiber endface.

Conversely, the near field $E(x',y')$ can be calculated from the far field $E_f(x,y,z)$ by solving Eq. (5.10) for $E_F(f_x,f_y)$:

$$E_F(f_x,f_y) = -j\lambda z\exp(jkr)E_f(x,y,z) \qquad (5.11)$$

with $x = \lambda z f_x \quad y = \lambda z f_y$, and by inserting $E_F(f_x,f_y)$ into the formula for the two-dimensional Fourier transform:

$$E(x',y') = \iint E_F(f_x,f_y)\exp[-j2\pi(f_x x' + f_y y')]df_x f_y \ . \qquad (5.12)$$

5.3.3.2.2 Simulation results

Based on near-filed calculation and theoretical functions in Sections above, Fig. 5.9 shows the electric far-field amplitude profiles of the guided modes of the c-2MF, and Fig. 5.10 shows the electric far-field phase profiles of the guided modes of the c-2MF.

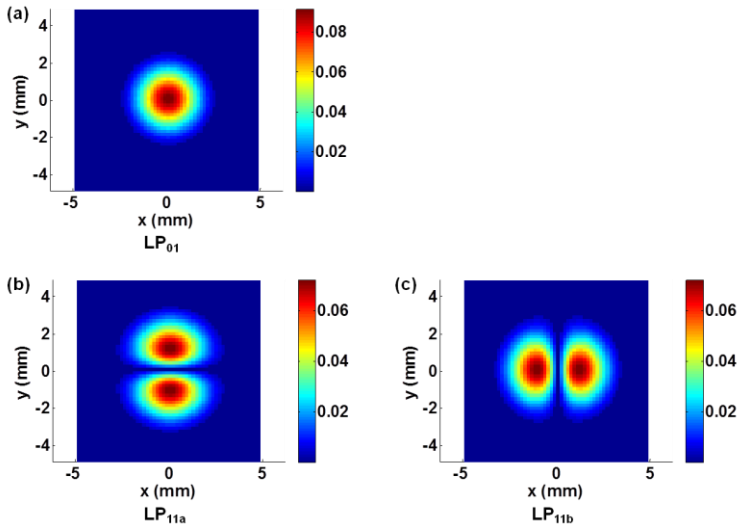

Fig. 5.9. Electric far-field amplitude profiles for all the guided modes of the c-2MF.

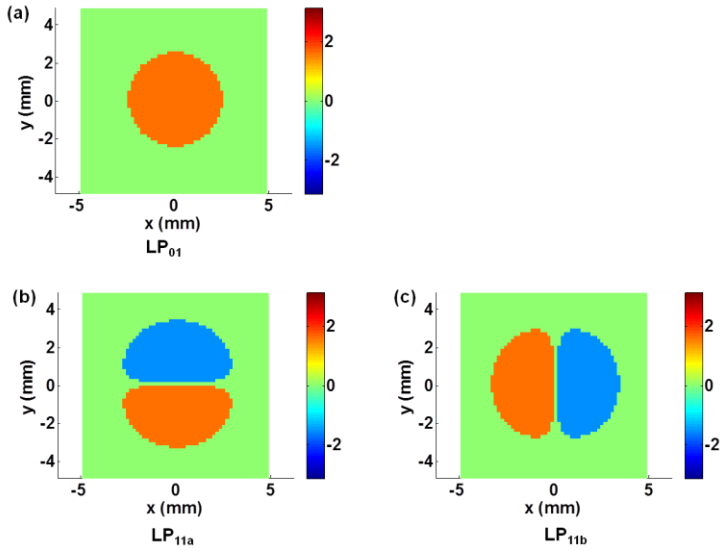

Fig. 5.10. Electric far-field phase profiles for all the guided modes of the c-2MF. Light green areas in the phase graphs indicate regions where the field intensity is below 5% of the peak field amplitude.

5.3.3.2.3 Experimental results

Complex mode pattern imaging for the guided modes of the c-2MF (LP_{01} mode and LP_{11} mode) in the far-field are shown in Fig. 5.11. Fig. 5.11(a) and (b) shows the electric amplitude image and phase image of LP_{01} mode in the far-field; Fig. 5.11(c) and (d) shows the electric amplitude image and phase image of LP_{11} mode in the near-field. The experimental results are consistent with the simulation results in previous Section.

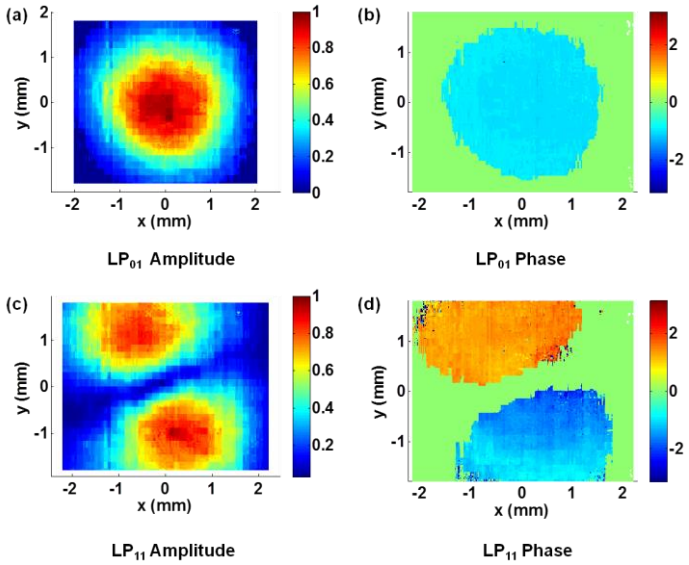

Fig. 5.11. (a) Electric far-field amplitude image for LP01 of the c-2MF. (b) Electric far-field phase image for LP01 of the c-2MF. (c) Electric far-field amplitude image for LP11 of the c-2MF. (d) Electric far-field phase image for LP11 of the c-2MF. Light green areas in the phase graphs indicate regions where the field intensity is below 10% of the peak field power.

5.4 Applications of complex imaging to fiber characterization

5.4.1 Mode pattern imaging for pure modes in FMFs

In the past decade, interest has increased in the use of MMFs and higher-order modes in many fields including A_{eff} scaling in high power fiber lasers [171-172], dispersion compensation [173], grating devices [174], and nonlinear optics [175] to name a few. These applications require a high degree of control in mode excitation and purity, thus necessitating accurate means to measure modal content. It would

be particularly useful to monitor modal content in real time, so that parameters like beam quality, thermal stability, etc., can be measured and adjusted dynamically by controlling parameters such as coiling radii, alignment, pump/signal power, etc. In many cases, the fundamental mode operation of a fiber is of particular interest due to the high beam quality.

5.4.1.1 Theoretical fundamentals

To validate the proposed complex imaging technique, we conduct the following tests: (1) generate pure LP_{01} mode when the FUT is a 10-meter SSMF; (2) generate pure LP_{01} mode when the FUT is the custom-designed 10-meter c-2MF, which supports two spatial modes, LP_{01}, LP_{11} at 1550 nm ; (3) generate pure LP_{11} mode when the FUT is the c-2MF (4) generate pure LP_{01} mode when the FUT is a custom-designed 10-meter c-5MF, which supports five spatial modes, LP_{01}, LP_{11a}, $LP_{11b,}$ LP_{21a} and LP_{21b} mode at 1550 nm. In each of the above situations, we calculate the overlapping integral η of the recovered (experimental) complex field E_r and the theoretical transverse mode field E_{th}

$$\eta = \frac{\left|\int E_r E^*_{th}\right|^2}{\int |E_r|^2 \int |E_{th}|^2} \tag{5.13}$$

The extinct ratio of each mode is then given by $C_{ExtinctionRatio} = 10\log_{10}(\frac{\eta}{1-\eta})$. It is noted that we use a 10-meter fiber only because the length is long enough to filter out cladding modes in few-mode fibers.

5.4.1.2 System configuration

The experimental setup for complex imaging has been illustrated in detail in Section 5.3. To generate pure fundamental and higher-order modes, the optical beam is coupled into a free space phase modulator, which is consisted of a 4F system with a SLM operating in reflection mode, as shown in Fig. 5.12(a). The modulated signal is then coupled back into the FUT to generate and transmit the modes we would like to

test. The relationship between the SLM phase patterns and the spatial modes are shown in Fig. 5.12(b).

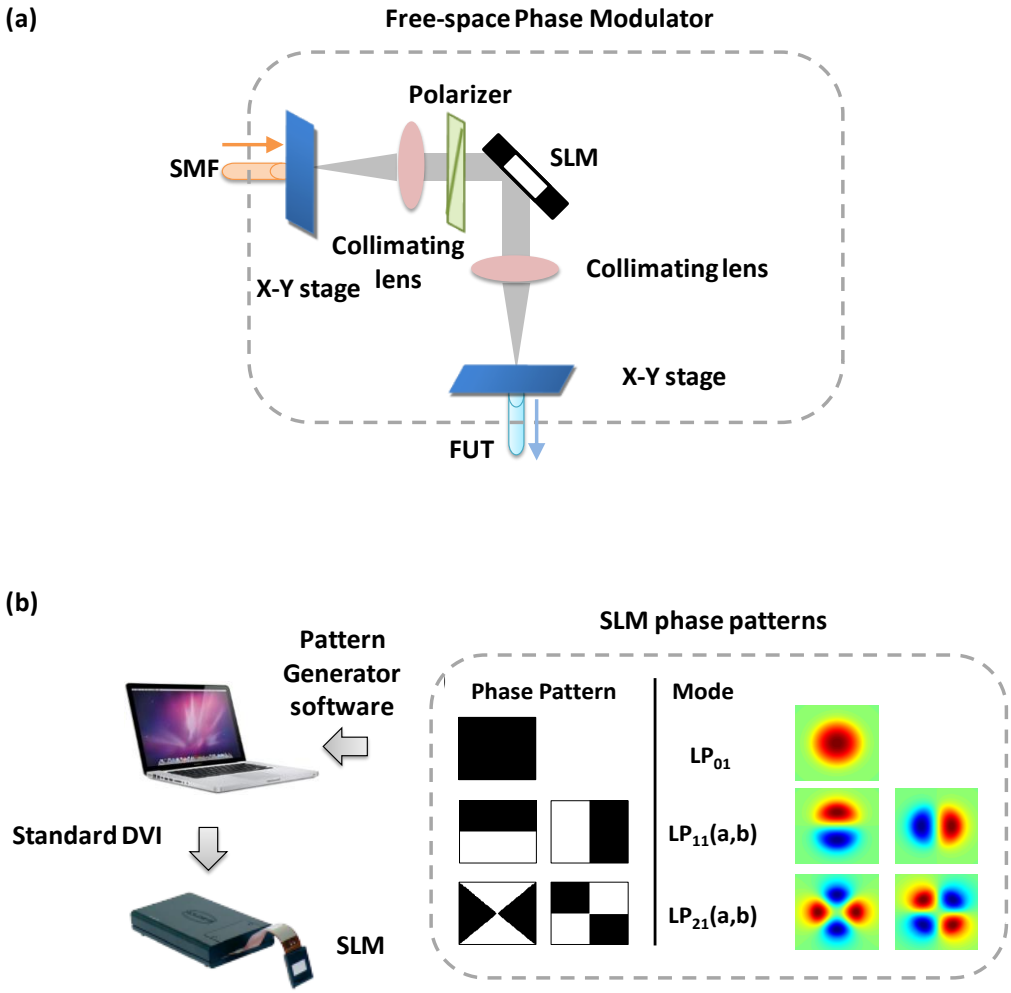

Fig. 5.12. (a) Schematic configuration of Free-space Phase Modulator. (b) Spatial modes in the FMF and the corresponding SLM phase patterns.

5.4.1.3 Results and discussions

We first show the measured and reconstructed field for each situation in Fig. 5.13(a) and (b). The calculated extinction ratios for these modes are shown in Fig. 5.13(c). Multiple tests are carried out for validation. We can observe from Fig. 5.13(c), for LP_{01} mode in SSMF the extinction ratio is all above 23 dB, for LP_{01} mode in c-2MF the extinction ratio is all above 25 dB, for LP_{11} mode in c-2MF the extinction ratio is above 17 dB, and for LP_{01} mode in c-5MF the extinction ratio all above 27 dB. These results with high extinction-ratio of > 17 dB show that the proposed complex

imaging technique achieves an excellent performance, which is reliable and accurate for further experiments such as mode decomposition and DMD (differential mode delay) characterization.

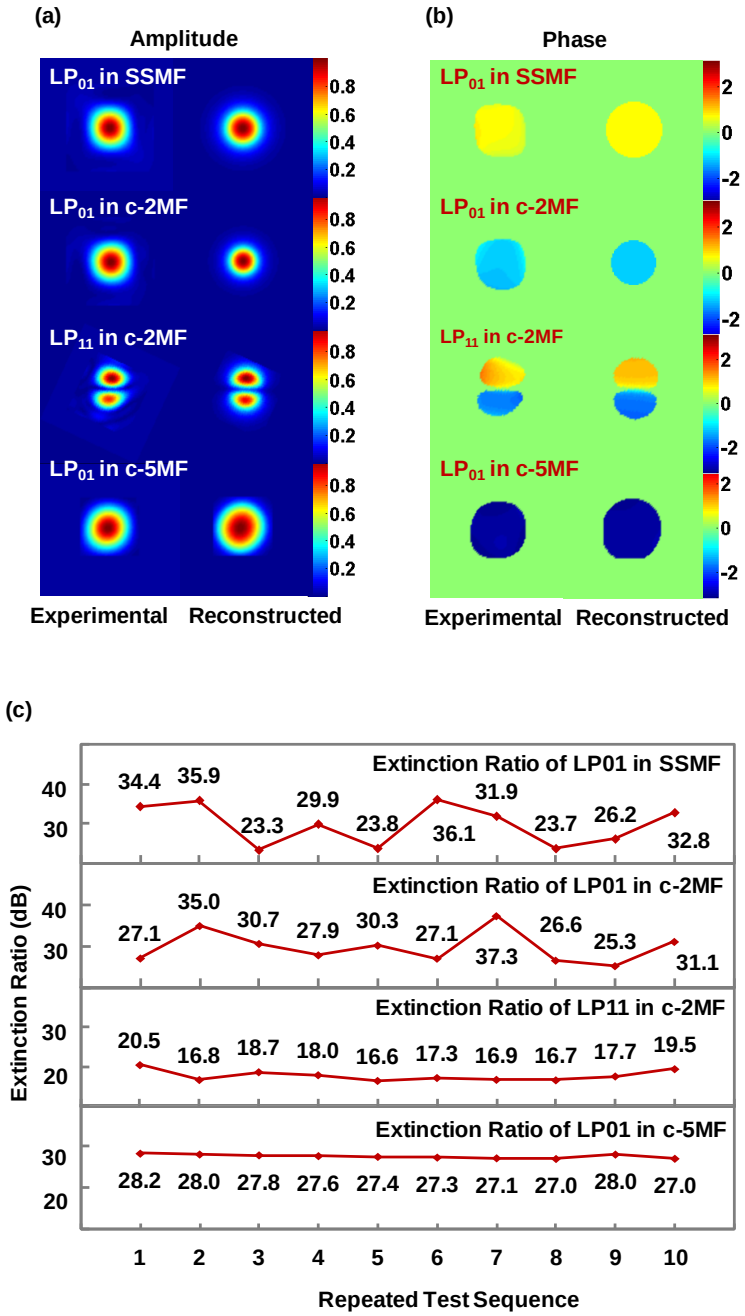

Fig. 5.13 (a) Experimental (left) and reconstructed (right) intensities of the input. (b) Experimental (left) and reconstructed (right) phases of the input. Light green areas in the phase graphs indicate regions where the field intensity is below 10% of the peak field amplitude. Expt.: Experimental; Recon: Reconstructed. (c) Measured extinction ratio of pure fundamental and higher-order modes using complex imaging.

Fluctuation observed in Fig. 5.13(c) is due to the stability limitation of the devices used, such as fiber movement or optical table vibration. The fluctuation is more apparent where the mode is purer and the extinction ratio is higher. The extinction ratio is mainly limited by the imperfection of our measurement devices and sub-systems Moreover, spatial or power imbalance between I and Q, non-functional pixels of the CCDs also add up to the computation error and thus decrease the extinction ratio.

5.4.2 Complete mode decomposition in FMFs

Table 5.2. Parameters for custom-designed c-5MF

Parameter	Unit	Value
Spool Length	m	3,000
Core Diameter	µm	14.4
Cladding Diameter	µm	125
Refractive Index (Core)		1.4519
Refractive Index (Cladding)		1.4440
Effective Refractive Index (LP_{01})		1.4503
Effective Refractive Index (LP_{11})		1.4481
Effective Refractive Index (LP_{21})		1.4453
Chromatic Dispersion (LP_{01})	ps/(nm*km)	22.56
Chromatic Dispersion (LP_{11})	ps/(nm*km)	22.66
Chromatic Dispersion (LP_{21})	ps/(nm*km)	9.3
Group Delay(LP_{01})	ps/km	4908132.3
Group Delay(LP_{11})	ps/km	4911851.2
Group Delay(LP_{21})	ps/km	4913677.8
LP_{21} Cut-off Wavelength	µm	2.825
LP_{11} Cut-off Wavelength	µm	1.777
Fiber Loss	dB/km	0.3

On the other hand, high-performance, high-power fiber-lasers [171, 176] demand excellent output beam-qualities. The design of novel fiber platforms to achieve this requires the propagation of only one mode in fibers that are not strictly single-moded [177-181], putting a high premium on modal discrimination. Therefore, it is essential to develop experimental methods that reveal the modal content and modal weights. Specifically, techniques that make no assumptions about the fiber under test are of interest.

The fundamental difficulty in modal decomposition is that the phase information could not be derived directly. Here we use our two dimensional complex mode field

to realize modal decomposition for the field at the output end of a generic waveguide structure. In this work, we have analyzed c-5MF. The fiber parameters are summarized in Table 5.2.

5.4.2.1 Theoretical fundamentals

The beam profiles typically span at least a 128 x 128 pixel area in far field, and after Fourier transformed back to nearfield, there are at least a 35 x 35 pixel area in near field. The calculation is demonstrated below.

The spatial resolution (or the so-called pixel pitch) of the far-field is 20 μm (which is dependent on the resolution of the CCD), and the relationship between the spatial resolution of the near-field d_n and the far-field d_f is $d_n = \frac{1}{d_f L}\lambda f$, where λ is the wavelength, f is the focal length of the collimator, L is the FFT size. After putting in all the terms, we get the value of d_n which is 0.3406 μm. On the other hand, the mode field radius (or diameter) was defined as for Gaussian beams. For step-index single-mode fibers, the mode radius (or diameter) could be estimated from the core radius and the V-number, using Marcuse's equation [59]. With the specifications of the c-5MF listed in Table 5.2, the near-field mode diameter is calculated as 11.9 μm. As a result, the pixel number for one dimension is calculated as 11.9 μm / 0.3406 μm ≈ 35, and we could say after Fourier transformed back to nearfield the mode span at least a 35 x 35 pixel area in near field.

Since the field is determined over several hundreds of pixels ($35 \times 35 = 1225$), we can perform a least squares fit of the amplitudes and phases of the 5 modes using the Moore-Penrose pseudoinverse analysis. This pseudoinverse technique is ideally suited for over determined problems such as our case in which the image is completely determined by a small number of coefficients. It conducts a least-squares fit of the amplitudes and phases given the data over hundreds of pixels. This matrix manipulation is fast, and the pseudoinverse gives the modal coefficients of the chosen basis.

In detail, the propagating field of a step-index fiber can be projected on the Eigen modes of the fiber. It can be mathematically expressed at wavelength λ as

$$E(x,y)=\sum_{n=1}^{N}\rho_n e^{j\theta_n}\mathrm{I}_n(x,y) \tag{5.14}$$

where $E(x,y)$ is an arbitrary propagating filed and $\mathrm{I}_n(x,y)$ is the nth Eigen mode of the fiber with modal amplitude ρ_n and modal phase θ_n ($\rho_n^{\,2}$ is called modal weight/ power). The total number of the Eigen modes is N and all of them form an orthogonal basis set. Normally, the fields mentioned above are normalized unit thus leading to $\sum_{n=1}^{N}\rho_n^{\,2}=1$, x and y is the horizontal and vertical coordinates. In fact, the principle of the MD method is to achieve the modal amplitude and phase of individual Eigen mode. It should be noted that this paper assumes the case of few-mode step-index (SI) fiber whose Eigen modes can be described in terms of LP mode [59]. Given fiber specifications and experimental parameters, the nth LP mode field $\mathrm{I}_n(x,y)$ could be calculated. Through our complex imaging method demonstrated in Section 5.3, the arbitrary propagating filed $E(x,y)$ could be measured. If we select M spatial pixels out, we have M equations in the form of Eq. (5.14), with N unknown modal coefficients ($C_n=\rho_n e^{j\theta_n},\ \ n=1,2,\ldots N$), which could be written in the form of the following matrices

$$\begin{bmatrix} E(1)\\ E(2)\\ \bullet\\ \bullet\\ \bullet\\ E(M)\end{bmatrix}=\begin{bmatrix} I_1(1) & I_2(1) & \bullet & \bullet & \bullet & I_N(1)\\ I_1(2) & I_2(2) & \bullet & \bullet & \bullet & I_N(2)\\ \bullet & \bullet & & & & \bullet\\ \bullet & \bullet & & & & \bullet\\ \bullet & \bullet & & & & \bullet\\ I_1(M) & I_2(M) & \bullet & \bullet & \bullet & I_N(M)\end{bmatrix}\begin{bmatrix} C_1\\ C_2\\ \bullet\\ \bullet\\ \bullet\\ C_N\end{bmatrix} \tag{5.15}$$

when the value of M outnumbers that of N, we could use the Moore-Penrose pseudoinverse analysis to determine these unknown modal coefficients, and in this way, the modal decomposition is performed.

Prior to MD, one should firstly calculate the theoretical LP modes according to the parameters of FUT and the scaled parameters. In addition, the coordinate

systems of the measured and reconstructed intensities should share the same origin [182]. The alignment is vital for the accuracy of the MD. For calibration, the beam centers are determined from signal beams with symmetric profiles. Then, the decomposition algorithm optimizes this location by minimizing error as a function of beam center. Since only the relative phases between the modes are important and also we are not able to measure the absolute phase, we choose the phase of one of the modes to be 0. In our case, we assume the phase of the fundamental mode $\theta_1 = 0$ and or other phases are relative to θ_1 .

5.4.2.2 System configuration

For the experiment, we excite different mode combinations into the FUT. After obtaining the 2-D complex mode fields by complex imaging, we perform Moore–Penrose pseudoinverse analysis to achieve modal coefficient for each guiding mode.

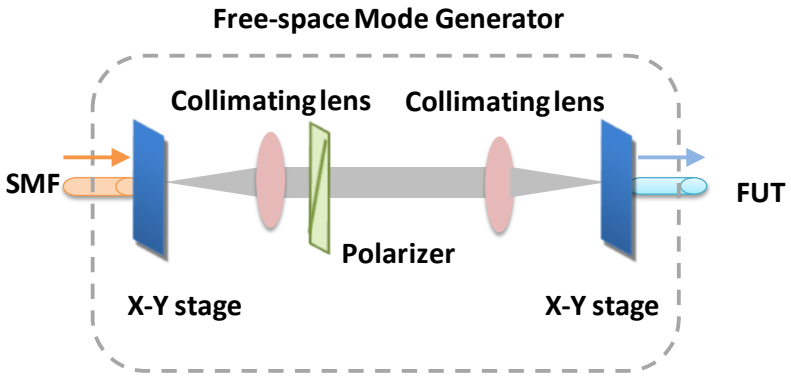

Fig. 5.14. Schematic configuration of Free-space Mode Generator.

The experimental setup for complete mode decomposition using complex imaging is the same as explained in the Section 5.3. To excite different mixed-mode combinations into the FUT, we could either modulate different phase patterns onto the input beam by using SLM, or simpler, use offset launch technique. The offset launch is implemented by projecting a small circular spot onto the fiber end at a position radially offset from the fiber core center. The offset launch allows the excitation of a well defined subset of predominately higher-order mode groups to be generated. The modal composition is determined by the offset, and we adjust the offset so that different mixed-mode combinations could be exited into the FUT. We

replace the Free-space Phase Modulator for the experimental setup (as shown in Fig. 5.2) with the Free-space Mode Generator (as shown in Fig. 5.14). The offset adjustment could be realized by adjust the X-Y stage at the fiber end of the FUT.

The DSP procedures after we achieve the 2-D complex near-field through complex imaging are summarized here: (1) mode decomposition using the Moore–Penrose pseudoinverse analysis to perform a least-squares fit of the calculated 2-D complex near-field; (2) mode reconstruction using modal amplitude (or power) coefficients and modal phase coefficients obtained by step (1); (3) performance evaluations with the 2-D cross correlation coefficient of the two fields (the recovered complex near-field and the reconstructed near-field from step (2)).

5.4.2.3 Results and discussions

We first excite one mixed-mode combination (Combination I) into the FUT, and the modal power (weight) and modal phase for each degenerate mode are shown in Fig. 5.15(a). Repeated tests are carried out which display similar results. The experimental and reconstructed field amplitude and field phase for the input mixed-mode field are shown in Fig. 5.15(b), and in Table 5.3, the final cross-correlation coefficients between the experimental fields and reconstructed fields are displayed. All the results are ~0.99, which leads to the conclusion that our proposed mode decomposition technique shows excellent performance.

To demonstrate the repeatability and stability of our technique, we change the composition of the input mixed-mode (Combination II) and plot the same figures, shown in Fig. 5.16. Table 5.4 also shows good correlation between the experimental fields and reconstructed fields as all the cross-correlation coefficients are above 0.99.

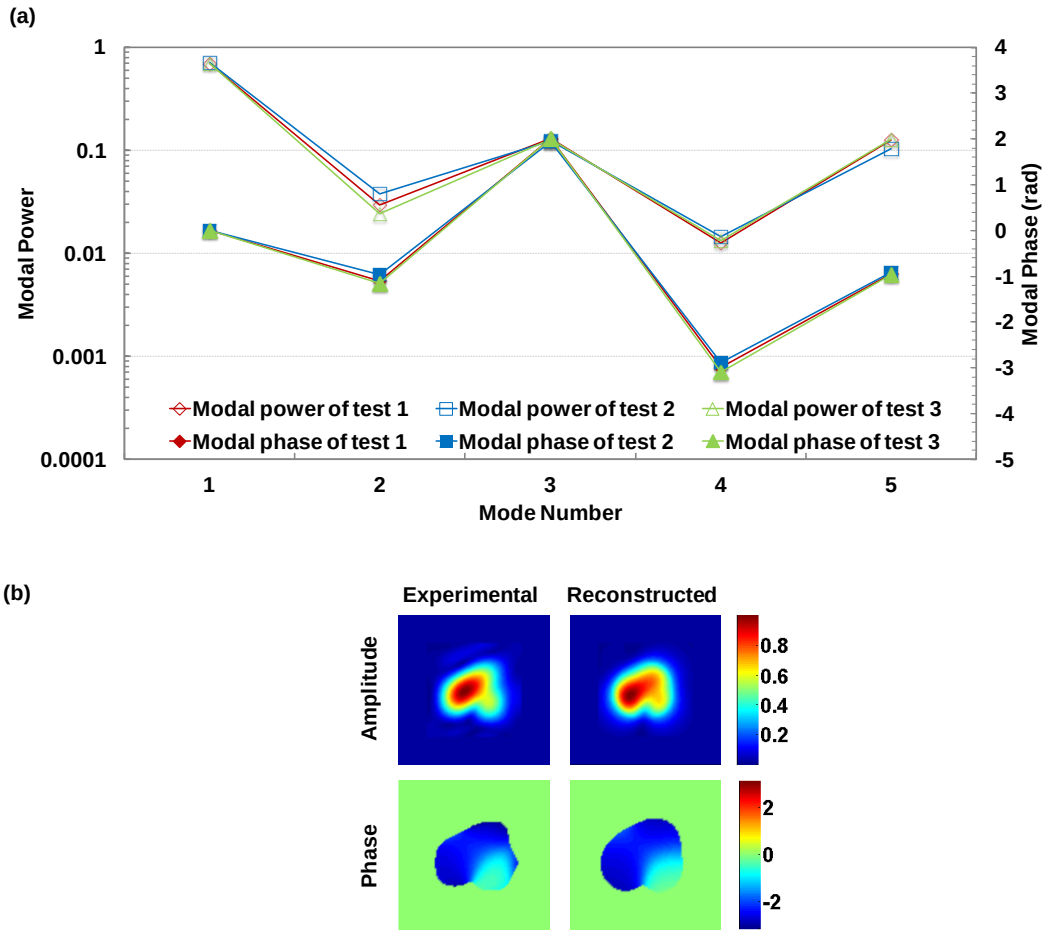

Fig. 5.15. (a) The recovered modal power and modal phase for each degenerate mode, repeated for 3 times. (b) Experimental (left) and reconstructed (right) field amplitude (top) of the input; experimental (left) and reconstructed (right) field phase (below) of the input. Light green areas in the phase graphs indicate regions where the field amplitude is below 10% of the peak field amplitude.

Table 5.3. Cross correlation coefficients

	Correlation coefficient for field amplitude	Correlation coefficient for field phase
Test 1	0.992	0.996
Test 2	0.991	0.996
Test 3	0.992	0.997

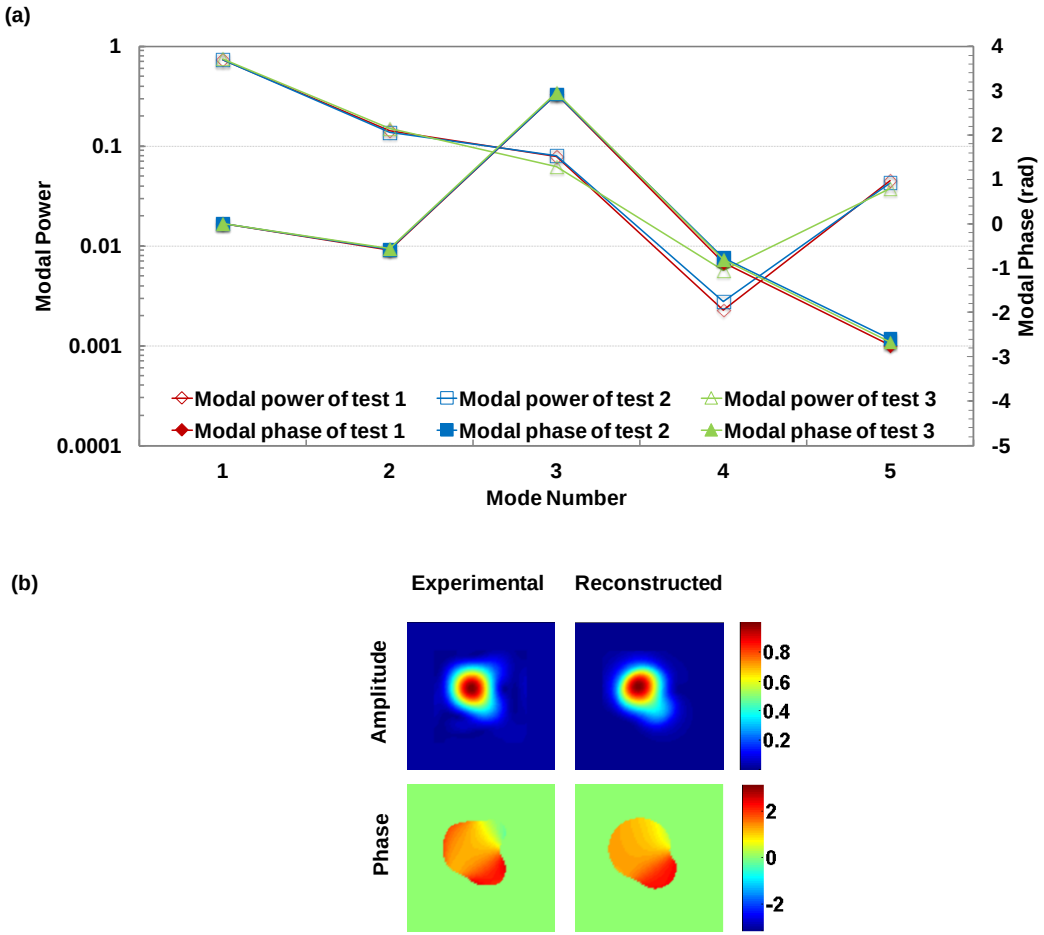

Fig. 5.16. (a) The recovered modal power and modal phase for each degenerate mode, repeated for 3 times. (b) Experimental (left) and reconstructed (right) field amplitude (top) of the input; experimental (left) and reconstructed (right) field phase (below) of the input. Light green areas in the phase graphs indicate regions where the field amplitude is below 10% of the peak field amplitude.

Table 5.4 Cross correlation coefficients

	Correlation coefficient for field amplitude	Correlation coefficient for field phase
Test 1	0.996	0.995
Test 2	0.996	0.992
Test 3	0.996	0.996

5.4.3 Characterization of DMD for FMFs

Apart from 2-D full-field imaging and mode decomposition, the proposed complex imaging could also be used to characterize differential group delay (DGD) for communication systems.

5.4.3.1 Theoretical fundamentals

Modal dispersion is a distortion mechanism occurring in multimode fibers and other waveguides, in which the signal is spread in time because the propagation velocity of the optical signal is not the same for all modes. Dispersion could be measured with group delay or mode delay T_g in the case of modal dispersion. The group delay (T_g) of an optical element (e.g. a dielectric mirror or a piece of optical fiber) is defined as the derivative of the change in spectral phase with respect to the angular frequency:

$$T_g = \frac{\partial \varphi}{\partial \omega} \tag{5.16}$$

It has the units of a time and generally (in dispersive media) depends on the optical frequency and optical mode. It is noted that for FMF characterizations, DGD here is also known as differential mode delay (DMD).

5.4.3.2 System configuration

The experimental setup for characterization of DMD for FMFs using complex imaging is the same as explained in Section 5.3. To excite one arbitrary propagating mode into the FUT, we could either use the Free-space Phase Modulator as introduced in Section 5.4.1, or use the offset launch technique as introduced in Section 5.4.2. The principles and the procedures for DMD characterization are illustrated as below:

(i) Sweep the wavelength of signal source (LD) within a small range. In our case, since we would like to characterize the DMD around the wavelength 1550 nm, the sweeping range is then from 1549.98 nm to 1550.025 nm with the step size equals to 0.005 nm.

(ii) Input an arbitrary propagating mode and collect mode pattern images at corresponding wavelengths.

(iii) Recover the complex field with collected mode pattern images from last step and perform mode decomposition to achieve the modal phases at different wavelengths.

(iv) Calculate inter-modal differential phase between higher-order modes and fundamental modes (inter-modal differential phase could also be called differential mode phase) so that all the phases are referenced to the fundamental mode and the differential mode phase is related to DMD.

(v) Draw the curve of differential mode phase with change of wavelength. Differential mode phase is linear to wavelength and the linear coefficient is equal to $\frac{d\varphi}{d\lambda}$ while the DMD per unit length $\tau_g = \frac{d\varphi}{d\omega} = \frac{d\varphi}{d\lambda}\frac{\lambda^2}{2\pi c}$, and φ is differential mode phase. In this way, the DMD per unit length around the wavelength 1550 nm is characterized.

(vi) We continue the characterization within C-band by repeating all the above steps at the wavelength around 1530 nm, 1540 nm and 1560 nm. As a result, the DMDs within the C-band could be characterized.

5.4.3.3 Results and discussions

The experimental result for c-2MF is shown in Fig. 5.17. The recovered modal power for each degenerate mode (LP_{01}, LP_{11a} and LP_{11b}) versus wavelength is shown in Fig. 5.17(a). With modal phase data for each degenerate mode, differential mode phases between LP_{11a} and LP_{01}, LP_{11b} and LP_{01} versus wavelength are shown in Fig. 5.17(b), and the average of the two and its linear fit curve are also displayed in Fig. 5.17(b). The linear fit curve shows good linearity. And thus, DMD between LP_{11} and LP_{01} is calculated as 3.10 ps/m.

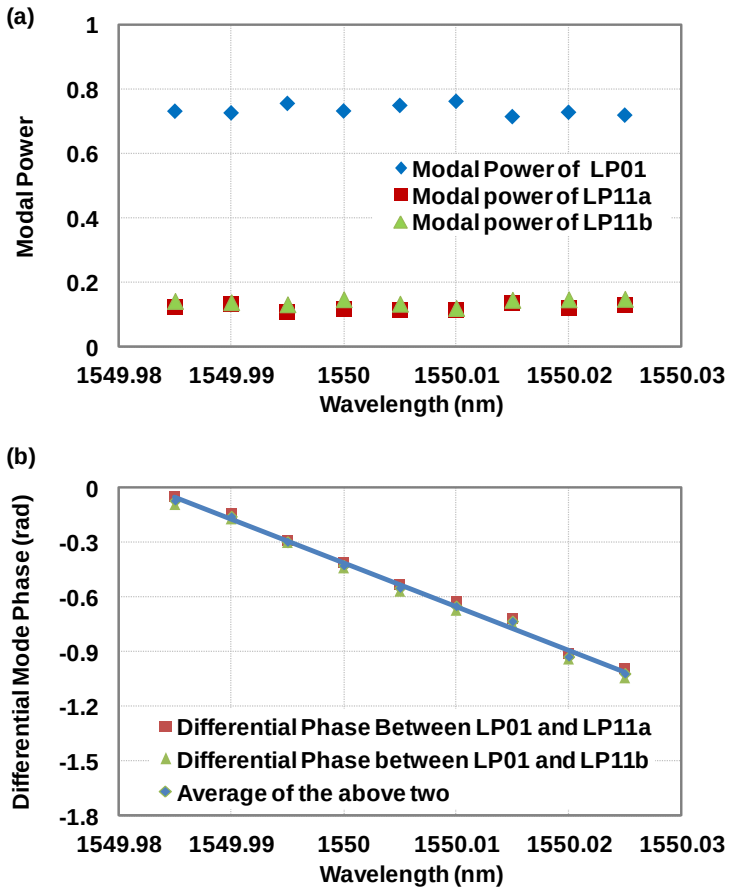

Fig. 5.17. (a) The recovered modal powers for the 3 modes, versus wavelength around the wavelength of 1550 nm. (b) Differential mode phase curve versus wavelength around the wavelength of 1550 nm.

We continue the characterization within C-band by repeating the above procedures at the wavelength around 1530 nm, 1540 nm, 1550 nm and1560 nm and the results are shown in Fig. 5.18(a) - (d) are the average of the differential phases between LP_{11a} and LP_{01}, LP_{11b} and LP_{01}, following the same procedures mentioned above. The linear fit curve is plotted for each figure and with the data of the slope; DMD between LP_{11} and LP_{01} is calculated at each wavelength point. The final calculated DMDs within the C-band are displayed in Fig. 5.18(e), and the theoretical DMDs are also plotted for comparison. The figure shows that our experimental results are consistent with the theoretical data.

We also measure the DMDs around the wavelength 1550 nm for the 10-meter c-5MF. The experimental result is shown in Fig. 5.18(f). Both of the two differential

mode phases show good linearity while different slopes of the curves indicate different DMDs for LP_{11} and LP_{21}. In Fig. 5.18(f), the DMD between LP_{11} and LP_{01} is calculated as 3.7269 ps/m, and the DMD between LP_{21} and LP_{01} is calculated as 5.3872 ps/m. This agrees extremely well with the theoretical value for the DMD between LP_{11} and LP_{01} of 3.7189 ps/m and DMD between LP_{21} and LP_{01} of 5.5455 ps/m, which is provided by the manufacturer.

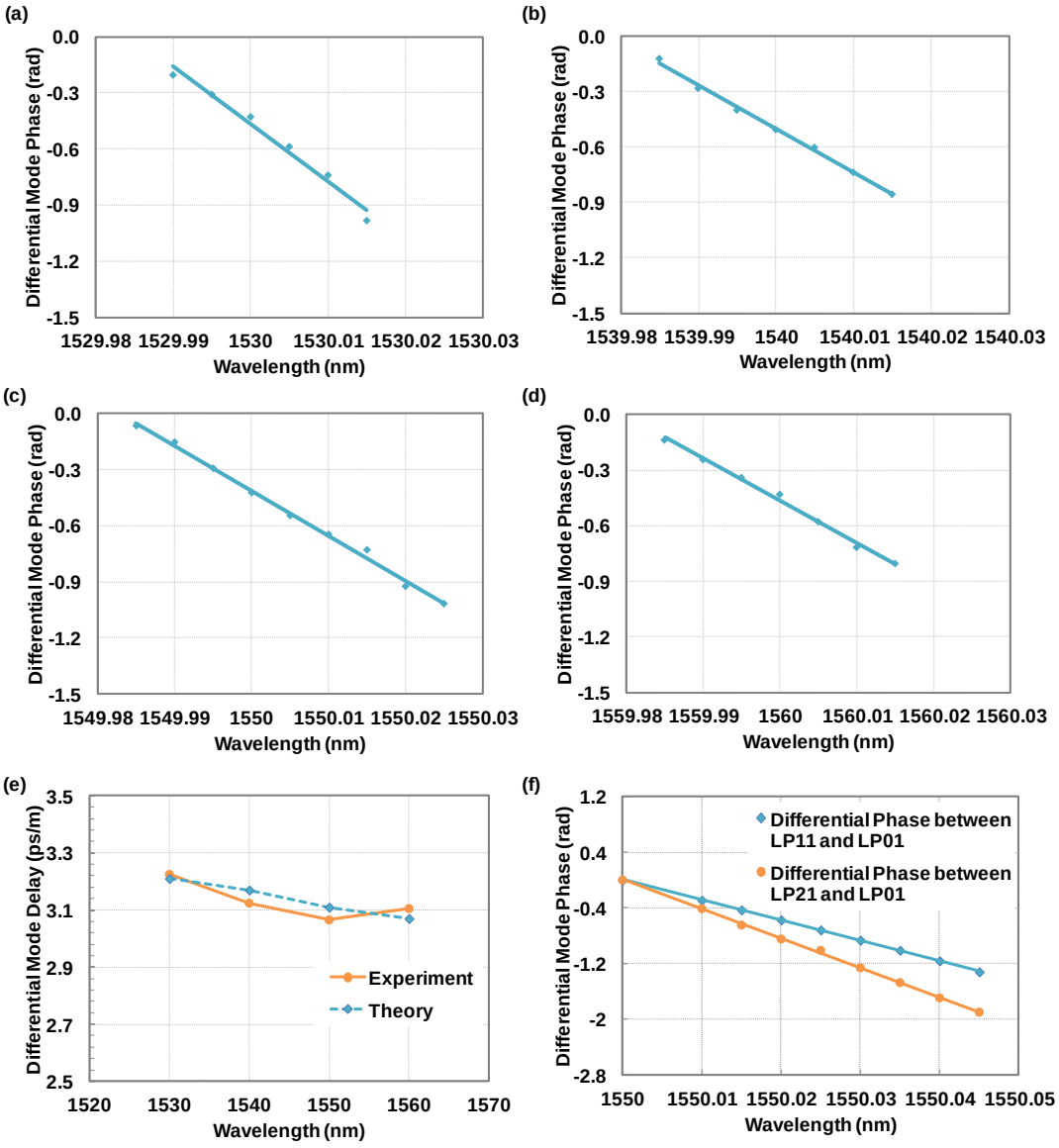

Fig. 5.18. (a)-(d) The average of the differential phases between LP11a and LP01, LP11b and LP01 at wavelength around 1530 nm, 1540 nm, 1550 nm and 1560 nm for c-2MF. (e) Calculated DMDs within the C-band for c-2MF. (f) The differential phases between LP11 and LP01, LP21 and LP01 at wavelength around 1550 nm for c-5MF.

Regarding the DGD measurement technique, we are able to measure DGD at any wavelength by sweeping several steps within a small range around the wavelength. Therefore, the whole measurement along the C-band could be carried out through one routing. For the measurement accuracy, we compare the experimental and theoretical values of DMD for both c-5MF and c-2MF and find the error is below 3%. For the measurement range, the only limitation is that we need to make sure that the phase shift $\Delta\varphi$ is less than 2π since the range of phase characterization is within 2π. Due to the fact that the sweep step of the laser source in our lab is above 0.0008 nm, the length of fiber is limited to less than 3000 meters.

5.5 Conclusions

In this chapter, we propose and implement a novel method to recover both amplitude and phase images and coherently detect the in-phase and quadrature components of the heterodyne signal simultaneously with a pair of CCD cameras. We first propose the concept of complex imaging via coherent detection for acquiring two-dimensional optical image that recovers amplitude and phase simultaneously. We then illustrate the system configurations and digital signal processing procedures for our novel imaging technique, and also demonstrate the experimental results of mode fields in the far-field and near-field in a TMF.

Then we continue our research by demonstrating its telecommunications applications. Firstly, we experimentally demonstrate the technique by characterizing mode patterns of pure fundamental mode and higher-order modes in FMFs with high extinction-ratio of > 17 dB. The experiment not only verifies our technique, but also shows that the technique achieves good systematic performance and high DSP accuracy, which is the foundation of further applications such as mode decomposition and DMD characterization. We also perform complete mode decomposition using complex imaging in FMF, and cross-correlation coefficients between the experimental complex fields and reconstructed complex fields are above 0.99. The advantage of our technique is that both amplitude and phase information could be used directly for modal content analysis, which simplifies the process and increases the accuracy as well. Finally we characterize the DMD in the

FMFs which agrees well with the theoretical predication. The advantage of our technique is that there is no limitation of the fiber length and the existence of mode coupling. The measurement error in our experiment is below 3%. In the future, the complex imaging via coherent detection may have great potential for telecommunications and biomedical applications where complex field can provide additional information.

6 Conclusions

6.1 Summary of this work

6.1.1 Characterization of frequency response for optical receivers with laser phase noise robustness

In the past few years, DD based optical communication systems have attracted significant attentions because of its low cost and simple implementation. In DD, it is important to separate the optical channel from RF channel. Consequently, calibration of the response for each optoelectronic component is necessary under such circumstances.

In this thesis, we propose a novel DSP algorithm for photodiode characterization probed by three wavelengths. The DSP algorithm has low computational complexity and scales only with logarithmic of number of the spectral points. We verify our proposed algorithm by measuring the phase response of an electrical filter. For the experiment, we demonstrate the frequency response calibration of a high-speed optical receiver with 30-GHz bandwidth photodiode, and a low-speed optical receiver with 14-GHz bandwidth photodiode, respectively. For the first time, the phase response of photodiode is characterized up to 20 GHz.

6.1.2 Few-mode fiber based optical sensors

With their high reliability, compactness and low fabrication cost, optical fiber sensors based on interferometer structure and Brillouin scattering have attracted great interest for use in assessing the performance of civil and geotechnical structures. In this thesis, we review our recent progress in the design and fabrication of FMF based optical sensors. Firstly, we characterize the performance of discrete optical sensor based on interferometer structure. The first kind is polarimetric interferometer sensor utilizing the mode beating between the polarizations (x and y), and its sensitivity against temperature and strain is characterized as -1.72 nm/°C and 24.5 pm/με in a PM-FMF. Increased temperature and strain sensitivity of PM-FMF is observed compared to that of conventional PMF. The second kind is intermodal

interferometer sensor utilizing the mode beating between the spatial modes (LP_{01} and LP_{11}), and its sensitivity against temperature and strain is characterized as -0.043 nm/℃/ and -0.0023 nm/με in a TMF. The proposed TMF intermodal interferometer sensor exhibits great potential due to good interfering visibility, good linearity, high sensitivity, and low cost. After that, we move onto the FMF based distributed sensors. We propose a unique FMF based multi-parameter optical fiber sensor for distributed measurement of temperature and strain. We launch a pump and a probe signal through specific linearly-polarized modes into a FMF, and monitor the BDG and BGS in each mode. By analyzing the temperature and strain coefficients of the BFS of the two lowest order (LP_{01}, LP_{11}) modes, discrimination of temperature and strain are successfully demonstrated, with an accuracy of 1.2 °C and 21.9 με

In summary, we have introduced several novel techniques for FMF based optical sensors and reviewed their recent progress. With the availability of high reliability few-mode devices and advance of fiber-optic technology such as SDM and coherent detection, FMF may have great potential in future fiber sensing systems.

6.1.3 Complex imaging via coherent detection

Optical fibers supporting multiple spatial modes have recently undergone an abundance of renewed interest, evidenced by the increased use of few-mode and multimode fibers for high-speed telecommunications and the use of highly multimode fibers for endoscopic medical imaging. Meanwhile, the technique of SDM can provide a way to increase the information capacity of a single fiber and the large modal area of these fibers is beneficial in alleviating detrimental nonlinear effects and reducing the chance of fiber damage, respectively. This results in a need for accurately characterizing the modal propagation in such fibers. The development of reliable and accurate techniques to investigate in detail the modal content of multimode fibers has thus become a topic of great interest.

In this thesis, we first propose the concept of complex imaging via coherent detection for acquiring 2-D nearfield optical image that recovers amplitude and phase simultaneously. We then illustrate the system configurations and digital signal

processing procedures for our novel imaging technique, and also demonstrate the experimental results of mode fields in both the near- and far-field regime for a two-mode fiber. We continue our research on our proposed nearfield coherent complex imaging by demonstrating its telecommunications applications. We firstly characterize mode patterns of pure fundamental mode and higher-order modes in FMFs as a validation of our imaging method. Next our method could also be applied to mode decomposition and mode content analysis for an arbitrary mixed mode pattern. Additionally, we sweep the input wavelength and measure DMD in FMFs. We experimentally demonstrate the technique using FMF modes with high extinction-ratio of > 17 dB. We also perform complete mode decomposition using coherent complex imaging in FMF, and cross-correlation coefficients between the experimental complex fields and reconstructed complex fields are above 0.99. Furthermore, we also characterize the FMF differential-group-delay which agrees well with the theoretical predication. The complex imaging via coherent detection may have great potential for telecommunications and biomedical applications where complex field can provide additional information.

6.2 Future work and perspectives

The success of SDM technique will depend on the highly integrated and cost-efficient components which can exploit the potentials to transmit and process parallel spatial modes simultaneously. Such components include the low MD, low loss FMFs, the high-efficiency mode converter, the high extinction ratio multiplexing/de-multiplexing devices, the few-mode amplifier, the few-mode fiber compatible coupler, switch, filter, and ROADM. In the future, SDM technologies can be potentially used for either communications and sensing.

For the sensing area, FMF sensor exhibits the advantages of high strain and temperature sensitivity compared with that of SSMF sensor. Although the sensitivity of specially designed SMF or MMF is comparable with that of FMF, FMF-based sensor is more cost-effective than the conventional PMF and PM-PCF. Also, by supporting only few modes, FMF sensor is more easily to be controlled and has better interfering visibility than MMF one. Thus, FMF based sensor shows its

potential in the future. Meanwhile, by exploring the fifth dimension - the spatial dimension in addition to the other four dimensions of time, wavelength, polarization and phase in SMFs, the significant difference in the coefficients for different spatial modes implies that FMF can be utilized for discriminative multi-parameter sensing.

For the complex imaging, our propose technique could be a powerful tool for mode imaging and fiber characterization. In the future, we will continue our research by using the complex imaging technique for measurement of mode coupling, characterization of transfer matrix, etc. The complex imaging via coherent detection also has great potential for biomedical applications where complex field can provide additional information.

Bibliography

1. A. Li, A. A. Amin, X. Chen, and W. Shieh, "Transmission of 107-Gb/s mode and polarization multiplexed CO-OFDM signal over a two-mode fiber," Opt. Express 19, 8808-8814 (2011).

2. H. Takara, A. Sano, T. Kobayashi, H. Kubota, H. Kawakami, A. Matsuura, Y. Miyamoto, Y. Abe, H. Ono, K. Shikama, Y. Goto, K. Tsujikawa, Y. Sasaki, I. Ishida, K. Takenaga, S. Matsuo, K. Saitoh, M. Koshiba, and T. Morioka, "1.01-Pb/s (12 SDM/222 WDM/456 Gb/s) crosstalk-managed transmission with 91.4-b/s/Hz aggregate spectral efficiency," in European Conference and Exhibition on Optical Communication, OSA Tech. Digest (online) (Optical Society of America, 2012), paper Th.3.C.1.

3. K. Igarashi, T. Tsuritani, I. Morita, Y. Tsuchida, K. Maeda, M. Tadakuma, T. Saito, K. Watanabe, K. Imamura, R. Sugizaki, and M. Suzuki, "1.03-Exabit/skm super-Nyquist-WDM transmission over 7,326-km seven-core fiber," in 39th European Conference and Exhibition on Optical Communication (ECOC) (2013).

4. R. Ryf, R. Essiambre, A. Gnauck, S. Randel, M. A. Mestre, C. Schmidt, P. Winzer, R. Delbue, P. Pupalaikis, A. Sureka, T. Hayashi, T. Taru, and T. Sasaki, "Space-division multiplexed transmission over 4200 km 3-core microstructured fiber," in Optical Fiber Communication Conference, OSA Tech. Digest (Optical Society of America, 2012), paper PDP5C.2.

5. E. Ip, M.-J. Li, C. Montero, and Y. Yano, "6×28-Gbaud few-mode recirculating loop transmission with gain-equalized inline few-mode fiber amplifier," in Optical Fiber Communication Conference/National Fiber Optic Engineers Conference, OSA Tech. Digest (online) (Optical Society of America, 2013), paper OW4F.3.

6. G. P. Agrawal, Nonlinear Fiber Optics, Third Edition, Academic Press, San Diego, CA, USA (2001).

7. K. Okamoto, Fundamentals of Optical Waveguides, Second Edition, Academic Press, San Diego, CA, USA (2000).

8. ITU-T Recommendation G.652, "Transmission Media Characteristics: Characteristics of a Single-Mode Optical Fiber Cable," (2005).

9. ITU-T Recommendation G.651, “Transmission Media Characteristics: Characteristics of a 50/125 M Multimode Graded Index Optical Fiber Cable,” (1993).

10. B. Y. Kim, J. N. Blake, S. Y. Huang, and H. J. Shaw, “Use of highly elliptical core fibers for two-mode fiber devices,” Opt. Lett. vol. 12, pp. 729–731 (1987).

11. S. Y. Huang, J. N. Blake, and B. Y. Kim, “Perturbation effects on mode propagation in highly elliptical core two-mode fibers,” J. Lightwave Technol., vol. 8, no. 1, pp. 23–33 (1990).

12. J. N. Blake, B. Y. Kim, and H. J. Shaw, “Fiber-optic modal coupler using periodic microbending,” Opt. Lett., vol. 11, pp. 177–179 (1986).

13. J. N. Blake, S. Y. Huang, B. Y. Kim, and H. J. Shaw, “Strain effects on highly elliptical core two-mode fibers,” Opt. Lett., vol. 12, pp. 732–734 (1987).

14. T. Morioka, Y. Awaji, R. Ryf, P. Winzer, D. Richardson, and F. Poletti, “Enhancing optical communications with brand new fibers,” Communications Magazine, vol. 50, no. 2, pp. s31–s42 (2012).

15. A. Li, A. A. Amin, X. Chen, S. Chen, G. Gao, and W. Shieh, “Reception of Dual-Spatial-Mode CO-OFDM Signal Over a Two-Mode Fiber,” J. Lightwave Technol., vol. 30, pp. 634–640 (2012).

16. A. A. Amin, A. Li, S. Chen, X. Chen, G. Gao, and W. Shieh, “Dual-LP11 mode 4x4 MIMO-OFDM transmission over a two-mode fiber,” Opt. Express, vol. 19, pp. 16672–16679 (2011).

17. X. Chen, A. Li, J. Ye, A. Al Amin, and W. Shieh, “Reception of Dual-LP11-Mode CO-OFDM Signals through Few-mode Compatible Optical Add/Drop Multiplexer,” in OFC, paper PDP5B.4 (2012).

18. G. Keiser, "Optical Communications Essentials," in FTTX Concepts and Applications, 1, Wiley-IEEE Press, pp.19-44 (2006).

19. K.C. Kao and G.A. Hockham, “Dielectric-Fibre Surface Waveguides for optical frequencies” Proc. IEEE, 113, 1151 (1966)

20. E. E. Basch andT. G. Brown,”Jntroduction tocoherent optical fiber transmission,” IEEE Commun. Mag., vol. 23, pp. 23-30, May 1985.

21. T. Li, ”Advances in lightwave systems research,” AT&T Tech. J., vol. 66, pp. 5-18 (1987).

22. T. E. Bell, “Single-frequency semiconductor lasers,” IEEE Spectrum, pp. 38-45, Dec. 1983. R. A. Linke and P. S. Henry, “Coherent optical detection: A thousand calls on one circuit,” IEEE Spectrum, pp. 52-57 (1987).

23. R. A. Linke, “Optical heterodyne communications systems,” /IEEE Commun. Mag., pp. 36-41 (1989).

24. J. Salz, ”Modulation and detection for coherent lightwave communications,” IEEE Commun. Mag., vol. 24, pp. 38-49 (1986).

25. T. Okoshi, K. Emura, K. Kikuchi, and R. Th. Kersten, “Computation of bit-error rate of various heterodyne and coherent type optical communication schemes,” J. Opt. Commun., vol. 2, no. 3, pp. 89-96 (1981).

26. R. E. Wagner, N. K. Cheung, and P. Kaiser, “Coherent lightwave systems for interoffice and loop-feeder applications,” J. Lightwave Technol., vol. LT-5, pp. 429-438 (1987).

27. P. S. Henry, ”High-capacity lightwave local area networks,” IEEE Commun. Mag., pp. 20-26 (1989).

28. K. Nosu and K. Iwashita, “Optical FDM transmission techniques,” J. Lightwave Technol., vol. LT-5, pp. 1301-1308, (1987).

29. Fujitsu, “Digital Coherent Transmission: A Paradigm Shift of Optical Transmission Technology”, SubOptic Conference, (2010).

30. S. J. Savory, G. Gavioli, R. I. Killey, and P. Bayvel, “Electronic compensation of chromatic dispersion using a digital coherent receiver,” Optics Express, vol. 15, pp. 2120–2126 (2007).

31. D. S. Ly-Gagnon, S. Tsukarnoto, K. Katoh, and K. Kikuchi, “Coherent detection of optical quadrature phase-shift keying signals with carrier phase estimation,” J. Lightwave Technol., vol. 24, pp. 12–21 (2006).

32. S. B. Cohn and N. P. Weinhouse, “An automatic microwave phase measurement system,” Microwave Journal, vol. 7, pp. 49–56 (1964).

33. C. A. Hoer and K.C. Roe, "Using an arbitrary six-port junction to measure complex voltage ratios", IEEE Trans. on MTT, vol. MTT-23, pp. 978–984 (1975).

34. A. J. Lowery and J. Armstrong, “Orthogonal-frequency-division multiplexing for dispersion compensation of long-haul optical systems,” Opt. Express, vol. 14, no. 6, pp. 2079-2084 (2006).

35. W. Peng, X. Wu, K. Feng, V. R. Arbab, B. Shamee, J. Yang, L. C. Christen, A. E. Willner, and S. Chi, “Spectrally efficient direct-detected OFDM transmission employing an iterative estimation and cancellation technique,” Opt. Express, vol. 17, no. 11, pp. 9099-9111 (2009).

36. J. M. Tang, P. M. Lane, and K. A. Shore, “High-speed transmission of adaptive modulated optical OFDM signals over multimode fibers using directly modulated DFBs,” J. Lightwave Technol., vol. 24, no. 1, pp. 429–441 (2006).

37. W.-R. Peng, B. Zhang, K.-M. Feng, X. Wu, A. E. Willner, and S. Chi, J. Lightwave Technol. 27, 5723-5735 (2009).

38. P. D. Hale, T. S. Clement, and D. F. Williams, “Know your response: Measuring frequency response of high-speed optical receivers requires microwave measurements,” SPIE Mag., p. 55, Mar. (2001).

39. “High-speed lightwave component analysis,” Agilent Technologies, Palo Alto, CA, Applicat. Note 1550-6, June (2000).

40. T. S. Clement, P. D. Hale, and P. A. Williams, “Fiber and component metrology for high-speed communications: What the manual doesn’t tell you,” in Optical Fiber Communications Conf. Dig., Mar., Tutorial Sessions, Session W-Z (2002).

41. P. D. Hale, D. F. Williams, and T. S. Clement, “Calibrated high-speed optoelectronic measurements,” presented at the IEEE MTT-S Int. Mi- crowave Symp. Dig.Workshop Notes, June, Workshop WMC (2002).

42. T. Morioka, H. Takara, S Kawanishi, “1 Tbit/s (100 Gbit/s 10 channel) OTDM/WDM transmission using a single supercontinuum WDM source,” Electronics Letters, vol. 32, no. 10, pp. 906-907 (1996).

43. M. Saruwatari, “All-optical signal processing for terabit/second optical transmission,” IEEE Journal of Selected Topics in Quantum Electronics, vol. 6, no. 6, pp. 1363-1374 (2000).

44. I. Baldine , H. G. Perros , G. N. Rouskas , D. S. Stevenson, “JumpStart: a just-in-time signaling architecture for WDM burst-switched networks,” Communications Magazine, vol. 40, no. 2, pp. 82-89(2002).

45. M. Koshiba, “Wavelength division multiplexing and demultiplexing with photonic crystal waveguide couplers,” Journal of Lightwave Technology, vol. 19, no. 12, pp. 1970-1975(2001).

46. M. Duser and P. Bayvel, Analysis of a dynamically wavelength-routed optical burst switched network architecture. Lightwave Technology, Journal of, 20(4): p. 574-585 (2002).

47. J. Strand, A.L. Chiu, and R. Tkach, “Issues for routing in the optical layer,” Communications Magazine, vol. 39, no. 2, pp. 81-87 (2001).

48. G. Bosco, A. Carena, V. Curri, R. Gaudino, and P. Poggiolini, “On the use of NRZ, RZ, and CSRZ modulation at 40 Gb/s with narrow DWDM channel spacing,” Journal of Lightwave Technology, vol. 20, no. 9, pp. 1694-1704 (2002).

49. J. Yu, X. Zhou, M. F. Huang, Y. Shao, D. Qian, T. Wang, M. Cvijetic, P. Magill, L. Nelson, M. Birk, S. Ten, H. B. Matthew, and S. K. Mishra, “17 Tb/s (161x 114 Gb/s) PolMux-RZ-8PSK transmission over 662 km of ultra-low loss fiber using C-band EDFA amplification and digital coherent detection,” in 34th European Conference on Optical Communication, paper Th.3.E.2 (2008).

50. A. Sano, H. Masuda, T. Kobayashi, M. Fujiwara, K. Horikoshi, E. Yoshida, Y. Miyamoto, M. Matsui, M. Mizoguchi, H. Yamazaki, Y. Sakamaki, and H. Ishii, “69.1-Tb/s (432 x 171-Gb/s) C- and Extended L-Band Transmission over 240 Km Using PDM-16-QAM Modulation and Digital Coherent Detection,” in OFC, paper PDPB7 (2010).

51. T. Hayashi, T. Taru, O. Shimakawa, T. Sasaki, and E. Sasaoka, “Ultra-Low-Crosstalk Multi-Core Fiber Feasible to Ultra-Long-Haul Transmission,” in OFC, paper PDPC2 (2011).

52. J. Sakaguchi, Y. Awaji, N. Wada, A. Kanno, T. Kawanishi, T. Hayashi, T. Taru, T. Kobayashi, and M. Watanabe, “109-Tb/s (7×97×172-Gb/s SDM/WDM/PDM) QPSK transmission through 16.8-km homogeneous multi-core fiber,” in OFC, paper PDPB6 (2011) .

53. J. Sakaguchi, B.J. Puttnam, W. Klaus, Y. Awaji, N. Wada, A. Kanno, T. Kawanishi, K. Imamura, H. Inaba, K. Mukasa, R. Sugizaki, T. Kobayashi, M. Watanabe, “19-core fiber transmission of 19x100x172-Gb/s SDM-WDM-PDM-QPSK signals at 305Tb/s,” in OFC, paper PDP5C.1 (2012).

54. R. Ryf, R. Essiambre, A. Gnauch, S. Randel, M.A. Mestre, C. Schmidl, P. Winzer, R. Delbue, P. Pupalaikis, A. Sureka, T. Hayashi, T. Taru, and T. Sasaki, “Space-division Multiplexed Transmission over 4200 km 3-Core mircrosctructured Fiber,” in OFC, paper PDP5C.2 (2012).

55. B. Zhu, T. Taunay, M. Fishteyn, X. Liu, S. Chandrasekhar, M. Yan, J. Fini, E. Monberg, and F. Dimarcello, “Space-, Wavelength-, Polarization-Division Multiplexed Transmission of 56-Tb/s over a 76.8-km Seven-Core Fiber,” in OFC, paper PDPB7 (2011).

56. B. Zhu, T.F. Taunay, M. Fishteyn, X. Liu, S. Chandrasekhar, M. F. Yan, J. M. Fini, E. M. Monberg, and F. V. Dimarcello, “112-Tb/s Space-division multiplexed DWDM transmission with 14-b/s/Hz aggregate spectral efficiency over a 76.8-km seven-core fiber,” Opt. Express, vol. 19, pp. 16665–16671 (2011).

57. S. Berdagué and P. Facq, “Mode division multiplexing in optical fibers,” Appl. Opt., vol. 21, pp. 1950–1955 (1982).

58. D. Marcuse, “Light Transmission Optics”, Van Nostrand Reinhold, New York, USA (1982).

59. A. W. Snyder and J. D. Love, “Optical Waveguide Theory”, Chapman and Hall, London, UK (1983).

60. M. J. Adams, “An Introduction to Optical Waveguides”, Wiley & Sons, Inc., New York, USA, Chap. 7 (1981).

61. J. Sakai and T. Kimura, “Bending loss of propagation modes in arbitrary-index profile optical fibers,” Appl. Opt., vol. 17, pp. 1499–1506 (1978).

62. R. C. Youngquist, J. L. Brooks, and H. J. Shaw, “Two-mode fiber modal coupler,” Opt. Lett., vol. 9, pp. 177–179 (1984).

63. S. Savin, M.J. F. Digonnet, G. S. Kino, and H. J. Shaw, “Tunable mechanically induced long-period fiber gratings,” Opt. Lett., vol. 25, pp. 710–712 (2000).

64. M. Salsi, C. Koebele, D. Sperti, P. Tran, P. Brindel, H. Mardoyan, S. Bigo, A. Boutin, F. Verluise, P. Sillard, M. Bigot-Astruc, L. Provost, F. Cerou, and G. Charlet, "Transmission at 2x100Gb/s, over Two Modes of 40km - long Prototype Few - Mode Fiber, using LCOS based Mode Multiplexer and Demultiplexer," in OFC, paper PDPB9 (2011).

65. J. Carpenter, B. C. Thomsen, and T. D. Wilkinson, “Degenerate Mode-Group Division Multiplexing,” J. Lightwave Technology, vol. 30, no. 24, Dec (2012).

66. Glenn Baxter, Steven Frisken, Dmitri Abakoumov, Hao Zhou, Ian Clarke, Andrew Bartos, Simon Poole, “Highly programmable Wavelength Selective Switch based on Liquid Crystal on Silicon switching elements,” in OFC, paper OThF2 (2006).

67. N.K. Fontaine, R. Ryf, D. T. Neilson, “NxM Wavelength Selective Crossconnect with Flexible Passbands.” in OFC, paper PDP5B2 (2012).

68. E. Ip, N. Bai, Y. Huang, E. Mateo, F. Yaman, S. Bickham, H. Tam, C. Lu, M. Li, S. Ten, A. P. T. Lau, V. Tse, G. Peng, C. Montero, X. Prieto, and G. Li, "88×3×112-Gb/s WDM Transmission over 50 km of 3 Mode Fiber with Inline FMF Amplifier," in ECOC, paper Th.13.C.2 (2011).

69. R. Ryf, N. K. Fontaine, and R. J. Essiambre, “Spot-Based Mode Coupler for Mode-Multiplexed Transmission in FMF,” IEEE Summer Topicals, paper TuC3.2 (2012).

70. R. Ryf, S. Randel, N. K. Fontaine, M. Montoliu, E. Burrows, S. Chandrasekhar, A. H. Gnauck, C. Xie, R. Essiambre, P. Winzer, R. Delbue, P. Pupalaikis, A. Sureka, Y. Sun, L. Gruner-Nielsen, R. V. Jensen, and R. Lingle, “32-bit/s/Hz Spectral Efficiency WDM Transmission over 177-km Few-Mode Fiber,” in OFC, paper PDP5A1 (2013).

71. J. Carpenter, T.D. Wilkinson, “Aberration correction in SLM based mode multiplexers,” in OFC, paper JW2A.27 (2013).

72. A. Li, A. A. Amin, X. Chen, and W. Shieh, “Reception of mode and polarization multiplexed 107-Gb/s CO-OFDM signal over a two-mode fiber,” in OFC, paper PDPB8 (2011).

73. R. Ryf, S. Randel, A. H. Gnauck, C. Bolle, A. Sierra, S. Mumtaz, M. Esmaeelpour, E. C. Burrows, R. Essiambre, P. J. Winzer, D. W. Peckham, A. H. McCurdy, and R. Lingle, “Mode-division multiplexing over 96 km of few-mode fiber using coherent 6x6 MIMO processing,” J. Lightw. Technol., vol. 30, pp. 521-531 (2012).

74. N. Bai, E. Ip, Y. Huang, E. Mateo, F. Yaman, M. Li, S. Bickham, S. Ten, J. Linares, C. Montero, V. Moreno, X. Prieto, V. Tse, K. M. Chung, A. P. T. Lau, H. Tam, C. Lu, Y. Luo, G. Peng, G. Li, and T. Wang, “Mode-division multiplexed transmission with inline few-mode fiber amplifier,” Opt. Express, vol. 20, pp. 2668-2680 (2012).

75. R. Olshansky, “Mode-coupling effects in graded-index optical fibers,” Appl. Opt., vol. 14, pp. 935-945 (1975).

76. R. Ryf, S. Randel, A. H. Gnauck, C. Bolle, R. Essiambre, P. Winzer, D. W. Peckham, A. McCurdy, and R. Lingle, “Space-division multiplexing over 10 km of three-mode fiber using coherent 6 × 6 MIMO processing,” in OFC, paper PDPB10 (2011).

77. N. K. Fontaine, C. R. Doerr, M.A. Mestre, R. Ryf, P. Winzer, L. Buhl, Y. Sun, X. Jiang, and R. Lingle, “Space-division multiplexing and all-optical MIMO demultiplexing using a photonic integrated circuit,” in OFC, paper PDP5B.1 (2012).

78. S. Randel, R. Ryf, A. Gnauck, M.A. Mestre, C. Schmidt, R. Essiambre, P. Winzer, R. Delbue, P. Pupalaikis, A. Sureka, Y. Sun, X. Jiang, and R. Lingle, “Mode-multiplexed 6x20-GBd QPSK Transmission over 1200-km DGD-Compensated Few-Mode Fiber,” in OFC, paper PDP5C.5 (2012).

79. R. Ryf, M.A. Mestre, A. Gnauck, S. Randel, C. Schmidt, R. Essiambre, P. Winzer, R. Delbue, P. Pupalaikis, A. Sureka, Y. Sun, X. Liang, D. Peckham, A.H.

McCurdy, and R. Lingle, “Low-Loss Mode Coupler for Mode-Multiplexed transmission in Few-Mode Fiber,” in OFC, paper PDP5B.5 (2012).

80. P. Sillard, M. Astruc, D. Boivin, H. Maerten, and L. Provost, “Few-Mode Fiber for Uncoupled Mode-Division Multiplexing Transmissions,” in 37th European Conference and Exposition on Optical Communication, paper Tu.5.LeCervin.7 (2011).

81. L. Gruner-Nielsen, Y. Sun, J. W. Nicholson, D. Jakobsen, R. Lingle, and B. Palsdottir, “Few Mode Transmission Fiber with low DGD, low Mode Coupling and low Loss,” in OFC, paper PDP5A.1 (2012).

82. Y. Yung, S. Alam, Z. Li, A. Dhar, D. Giles, I. Giles, J. Sahu, L. Grüner-Nielsen, F. Poletti, and D. Richardson, "First demonstration of multimode amplifier for spatial division multiplexed transmission systems," in 37th ECOC, , paper Th.13.K.4 (2011).

83. E. Ip, N. Bai, Y. Huang, E. Mateo, F. Yaman, S. Bickham, H. Tam, C. Lu, M. Li, S. Ten, A. P. T. Lau, V. Tse, G. Peng, C. Montero, X. Prieto, and G. Li, "88x3x112-Gb/s WDM Transmission over 50-km of Three-Mode Fiber with Inline Multimode Fiber Amplifier," in 37th ECOC, paper Th.13.C.2 (2011).

84. N. Bai, E. Ip, T. Wang, and G. Li, "Multimode fiber amplifier with tunable modal gain using a reconfigurable multimode pump," Opt. Express, vol. 19, pp. 16601–16611 (2011).

85. R. Ryf, A. Sierra, R. Essiambre, S. Randel, A. Gnauck, C. A. Bolle, M. Esmaeelpour, P. J. Winzer, R. Delbue, P. Pupalaikis, A. Sureka, D. Peckham, A. McCurdy, and R. Lingle, "Mode-Equalized Distributed Raman Amplification in 137-km Few-Mode Fiber," in 37th ECOC, paper Th.13.K.5 (2011).

86. N. Bai, E. Ip, T. Wang, and G. Li, "Multimode fiber amplifier with tunable modal gain using a reconfigurable multimode pump," Opt. Express, vol. 19, pp. 16601–16611 (2011).

87. C. Koebele, M. Salsi, G. Charlet, and S. Bigo, "Nonlinear Effects in Mode-Division-Multiplexed Transmission Over Few-Mode Optical Fiber," IEEE Photon. Technol. Lett., vol. 23, no. 18, pp. 1316–1318 (2011).

88. F. Ferreira, S. Jansen, P. Monteiro, and H. Silva, "Nonlinear Semi-Analytical Model for Simulation of Few-Mode Fiber Transmission," IEEE Photon. Technol. Lett., vol. 24, no. 4, pp. 240–242 (2012).

89. X. Chen, A. Li, G. Gao, A. A. Amin, and W. Shieh, "Characterization of Fiber Nonlinearity and Analysis of Its Impact on Link Capacity Limit of Two-Mode Fibers," Photonics Journal, IEEE, vol. 4, no. 2, pp. 455–460 (2012).

90. W. Shieh and Y. Tang, "Ultrahigh-Speed Signal Transmission Over Nonlinear and Dispersive Fiber Optic Channel: The Multicarrier Advantage," Photonics Journal, IEEE , vol. 2, no. 3, pp. 276–283 (2010).

91. Y. Tang, W. Shieh, and B.S. Krongold, "DFT-Spread OFDM for Fiber Nonlinearity Mitigation," IEEE Photon. Technol. Lett., vol. 22, no. 16, pp.1250–1252 (2010).

92. X. Chen, A. Li, G. Gao, and W. Shieh, "Experimental Demonstration of Improved Fiber Nonlinearity Tolerance for Unique-word DFT-Spread OFDM Systems," Opt. Express, vol. 19, pp. 26198–26207 (2011).

93. A. Li, X. Chen, G. Gao and W. Shieh, "Transmission of 1-Tb/s unique-word DFT-spread OFDM superchannel over 8,000-km SSMF", Proc. SPIE 8309, pp. 830929 (2011).

94. A. Li, X. Chen, G. Gao, W. Shieh, and B. Krongold, "Transmission of 1.63-Tb/s PDM-16QAM Unique-word DFT-Spread OFDM Signal over 1,010-km SSMF," in OFC, paper OW4C.1 (2012).

95. Yu, F. T. S. Yin, S. Ruffin, P. B.. “Fiber Optic Sensors,” CRC Press Taylor&Francis Group, ISBN 9781420053654, United State of America (2008).

96. D. Krohn, “Overview of Fiber Optic Sensors”, KMI’s 26TH Annual Newport Conference, October (2003).

97. Kashyap, R., “Photosensitive Optical Fibers: Devices and Applications”, Op. Fiber Tech., Vol.1 (1994).

98. J. Paulson “Distinctive advantacer conventional systems”, Technical Insights optical sensors analysis, Technical Insights, 13, Aug. (2003).

99. R. Narayanaswamy, O. S. Wolfbeis, Optical Sensors: Industrial, Environmental and Diagnostic Applications (2004).

100. F. Baldini, A. Giannetti, “Optical chemical and biochemical sensors: new trends”, Proc. SPIE,Vol: 5826, pp. 485-499 (2005).

101. F. Baldini, A. Falai, A. R. De Gaudio, D. Landi, A. Lueger, A. Mencaglia, D. Scherr, W. Trettnak, “Continuous monitoring of gastric carbon dioxide with optical fibres”, Sensors and Actuators, Vol: 90, pp. 132-138 (2003).

102. NI, “Fiber-Optic Sensing”, http://www.ni.com/opticalsensing/ (2012).

103. D. Erni, M. Jungo, and W. Baechtol, "Segmented VCSEL contact geometry for active coupling efficiency enhancement," in Workshop on Compound Semiconductor Devices and Integrated Circuits (WOCSDICE), (Photonics Communication Group, Swiss Federal Institute of Technology (ETHZ), , 67-68 (2003).

104. D. Lenz, B. Rankov, D. Erni, W. Bachtold, and A. Wittneben, "MIMO Channel for Modal Multiplexing in Highly Overmoded Optical Waveguides," in International Zurich Seminar on Communications (IZS), IEEE (2004).

105. F. Dubois, P. Emplit, and O. Hugon, “Selective mode excitation in graded-index multimode fiber by a computergenerated optical mask,” Opt. Lett. 19(7), 433–435 (1994).

106. J. E. Midwinter, “The prism-taper coupler for the excitation of single modes in optical transmission fibres,” Opt. Quantum Electron. 7(4), 297–303 (1975).

107. S. Zemon, and D. Fellows, “Tunneling leaky modes in a parabolic index fiber,” Appl. Opt. 15(8), 1936–1941 (1976).

108. E. Alon, V. Stojanovic, J. M. Kahn, S. Boyd, and M. Horowitz, "Equalization of modal dispersion in multimode fiber using spatial light modulators," in GLOBECOM '04. IEEE Global Telecommunications Conference, IEEE, 1023-1029 (2004).

109. B. R. Saltzberg, "Performance of an efficient parallel data transmission system," IEEE Trans. Commun., vol. 15, pp. 805-813 (1967).

110. W. Shieh and I. Djordjevic, Orthogonal Frequency Division Multiplexing for Optical Communications, Academic Press (2009).

111. W. Shieh and C. Athaudage, "Coherent optical orthogonal frequency division multiplexing," Electron. Lett., vol. 42, pp. 587–588 (2006).

112. S. L. Jansen, I. Morita, N. Takeda, and H. Tanaka, "20-Gb/s OFDM transmission over 4,160-km SSMF enabled by RF-Pilot tone phase noise compensation," in OFC, paper PDP15 (2007).

113. Y. Tang, W. Shieh, X. Yi and R. Evans, "Optimum design for RF-to-optical up-converter in coherent optical OFDM systems," IEEE Photon. Technol. Lett., vol. 19, pp. 483–485 (2007).

114. J. von Hoyningen-Huene, R. Ryf, and P. Winzer, "LCoS-based mode shaper for few-mode fiber," Opt. Express 21, 18097-18110 (2013)

115. K. S. Abedin, T. F. Taunay, M. Fishteyn, M. F. Yan, B. Zhu, J. M. Fini, E. M. Monberg, F. V. Dimarcello and P. W. Wisk, "Amplification and noise properties of an erbium-doped multicore fiber amplifier", Opt. Exp. 19, 16715-16721 (2011).

116. K. A. Murphy, T. A. Tran, W. V. Miller, A. M. Vengsarkar, and R. 0. Claus, "Miniaturized fiber optic Michelson-type interferometric sensors," Appl. Opt., vol. 30, p. 5063 (1991).

117. A. M. Vengsarkar and K. A. Murphy, "Fiber optic sensors in aerospace applications: The smart structures concept," Phofonics Specrrn, p. 1 19, Apr. (1990).

118. G. Meltz, J. R. Dunphy, W. H. Glenn, J. D. Farina, and F. J. Leonberger, "Fiber optic temperature and strain sensors," Proc. SPIE-Inr. Soc. Opt. Eng., vol. 798, p. 104 (1987).

119. M. Spajer, B. Carquille, H. Maillotte, Application of intermodal interference to fibre sensors, Optics Communications, 60 (5), pp. 261-264 (1986).

120. A. Bertholds and R. D/indliker, Conf. Proc. O.F.S. 84, VDE-Verlag GmbH, Berlin-Offenbach (1984).

121. J. G. Hanse and G. Mitchell "Linearized Fiber Optic Sensor Readout", Opt. Eng. 23(3), 233309 (1984).

122. A. M. Vengsarkar, W. C. Michie, L. Jankovic, B. Culshaw and R. O. Claus, "Fiber-optic dual-technique sensor for simultaneous measurement of strain and temperature," in Journal of Lightwave Technology, vol. 12, no. 1, pp. 170-177, Jan (1994).

123. N. Kaneda, Q. Yang, X. Liu, S. Chandrasekhar, W. Shieh, and Y.-K. Chen, "Real-Time 2.5 GS/s Coherent Optical Receiver for 53.3-Gb/s Sub-Banded OFDM," J. Lightwave Technol. 28, 494-501 (2010)

124. J. Wei, D. G. Cunningham, R. V. Penty, and I. H. White, "Feasibility of 100G Ethernet enabled by Carrierless Amplitude/Phase Modulation and Optical OFDM," in ECOC, paper P6.05 (2012).

125. T. M. F. Alves and A. V. T. Cartaxo, "Semi-analytical approach for performance evaluation of direct-detection OFDM optical communication systems," Opt. Express 17, 18714-18729 (2009).

126. B. O'Brian, U. S. Patent 2,825,260 (1958).

127. A. C. S. van Heel, "A new method of transporting optical images without aberrations," Nature, vol. 173, pp. 39 (1954).

128. H. H. Hopkins and N. S. Kapany, "A flexible fiberscope using static scanning," Nature, vol. 173, pp. 39–41 (1954).

129. B. I. Hirschowitz, U. S. Patent 3,010,357 (1961).

130. K. C. Kao and G. A. Hockham, "Dielectric-fiber surface waveguides for optical frequencies," IEE Proc., vol. 113, pp. 1151 (1966).

131. W. G. French, J. B. MacChesney, P. B. O'Connor, and G. W. Tasker, "Optical Waveguides with Very Low Losses," Bell Syst. Tech. J., vol. 53, pp. 951 (1974).

132. T. Miya, Y. Terunuma, T. Hosaka, and T. Miyashita, "Ultimate low-loss single-mode fiber at 1.55 μm," Electron. Lett., vol. 15, no. 4, pp. 106–108 (1979).

133. W.-R. Peng, Bo Zhang, K.-M. Feng, X. Wu, A. E. Willner, and S. Chi, "Spectrally Efficient Direct-Detected OFDM Transmission Incorporating a Tunable Frequency Gap and an Iterative Detection Techniques," J. Lightwave Technol. 27, 5723-5735 (2009).

134. R. Hui, M. O'Sullivan, “Fiber Optic Measurement Techniques,” Academic Press (2009).

135. N. H. Zhu, J. M. Wen, H. S. San, H. P. Huang, L. J. Zhao and W. Wang, "Improved optical heterodyne methods for measuring frequency responses of photodetectors," in IEEE Journal of Quantum Electronics, vol. 42, no. 3, pp. 241-248 (2006).

136. T.G. Giallorenzi, J.A Bucaro, A. Dandridge, G.H. Sigel, J.H. Cole, S.C. Rashleigh, and R.G. Priest, "Optical Fiber Sensor Technology," IEEE Trans. Microw. Theory Techn. 30(4), 472–511 (1982).

137. B. Lee, “Review of the present status of optical fiber sensors,” Optical Fiber Technology, 9(2), 57–79 (2003)

138. E. Udd, Fiber optic sensors, SPIE Optical Engineering Press (1993).

139. A. D. Kersey, M. A. Davis, H. J. Patrick, M. LeBlanc, K. P. Koo, C. G. Askins, M. A. Putnam, and E. Joseph Friebele, "Fiber grating sensors," J. Lightw. Technol. 15(8), 1442–1463 (1997).

140. K. O. Hill and G. Meltz, “Fiber Bragg grating technology fundamentals and overview,” J. Lightw. Technol. 15(8), 1263–1276 (1997).

141. Y. Liu, B. Liu, X. Feng, W. Zhang, G. Zhou, S. Yuan, G. Kai, and X. Dong, "High-birefringence fiber loop mirrors and their applications as sensors," Appl. Opt. 44(12), 2382–2390 (2005).

142. X. Dong, H. Y. Tam, and Ping Shum. "Temperature-insensitive strain sensor with polarization-maintaining photonic crystal fiber based Sagnac interferometer," Appl. Phys. Lett. 90(15), 151113 (2007).

143. M. Froggatt and J. Moore, "High-spatial-resolution distributed strain measurement in optical fiber with Rayleigh scatter," Appl. Opt. 37(10), 1735–1740 (1998).

144. D. Culverhouse, F. Farahi, C. N. Pannell, and D. A. Jackson. "Potential of stimulated Brillouin scattering as sensing mechanism for distributed temperature sensors," Electron. Lett. 25(14), 913–915 (1989).

145. J. P. Dakin, D. J. Pratt, G. W. Bibby, and J. N. Ross. "Distributed optical fibre Raman temperature sensor using a semiconductor light source and detector," Electron. Lett. 21(13), 569–570 (1985).

146. C. Koebele, M. Salsi, D. Sperti, P. Tran, P. Brindel, H. Mardoyan, S. Bigo, A. Boutin, F. Verluise, P. Sillard, M. Astruc, L. Provost, F. Cerou, and G. Charlet, "Two mode transmission at 2x100Gb/s, over 40km-long prototype few-mode fiber, using LCOS-based programmable mode multiplexer and demultiplexer," Opt. Express 19(17), 16593–16600 (2011).

147. S. Randel, R. Ryf, A. Sierra, P. J. Winzer, A. H. Gnauck, C. A. Bolle, R.-J. Essiambre, D. W. Peckham, A. McCurdy, and R. Lingle, "6×56-Gb/s mode-division multiplexed transmission over 33-km few-mode fiber enabled by 6×6 MIMO equalization," Opt. Express 19(17), 16697–16707 (2011).

148. X. Bao, D. J. Webb, and D. A. Jackson, "22-km distributed temperature sensor using Brillouin gain in an optical fiber," Opt. Lett. 18(7), 552–554 (1993).

149. K. Song, Z. He, and K. Hotate, "Distributed Strain Measurement with Millimeter-Order Spatial Resolution Based on Brillouin Optical Correlation Domain Analysis and Beat Lock-in Detection Scheme," in Optical Fiber Sensors, OSA Technical Digest (CD) (Optical Society of America), paper ThC2 (2006).

150. T. Kurashima, T. Horiguchi, H. Izumita, S. Furukawa, and Y. Koyamada, "Brillouin Optical-Fiber Time Domain Reflectometry, " IEICE Trans. Commun. E76-B(4), 382–390 (1993).

151. T. Horiguchi and M. Tateda, "BOTDA-nondestructive measurement of single-mode optical fiber attenuation characteristics using Brillouin interaction: theory," J. Lightw. Technol. 7(8), 1170–1176 (1989).

152. P. St. J. Russell, D. Culverhouse, and F. Farahi, "Experimental observation of forward stimulated Brillouin scattering in dual-mode single-core fibre," Electron. Lett. 26(15), 1195–1196 (1990).

153. K. Y. Song, Y. H. Kim, and B. Y. Kim, "Intermodal stimulated Brillouin scattering in two-mode fibers," Opt. Lett. 38(11), 1805–1807 (2013).

154. S. Li, M.-J. Li, and R. S. Vodhanel, "All-optical Brillouin dynamic grating generation in few-mode optical fiber," Opt. Lett. 37(22), 4660–4662 (2012).

155. Y. H. Kim and K. Y. Song, "Mapping of intermodal beat length distribution in an elliptical-core two-mode fiber based on Brillouin dynamic grating," Opt. Express 22(14), 17292–17302 (2014).

156. W. J. Bock and Tinko A. Eftimov, "Polarimetric and intermodal interference sensitivity to hydrostatic pressure, temperature, and strain of highly birefringent optical fibers," Opt. Lett. 18(22), 1979–1981 (1993).

157. J. Villatoro, V. Finazzi, V. P. Minkovich, V. Pruneri, and G. Badenes. "Temperature-insensitive photonic crystal fiber interferometer for absolute strain sensing," Appl. Phys. Lett. 91(9), 091109 (2007).

158. K. Y. Song, and K. Hotate, "All-optical dynamic grating generation based on Brillouin scattering in polarization maintaining fiber," in 19th International Conference on Optical Fibre Sensors, 70043T–70043T (2008).

159. Weiwen Zou, Zuyuan He, and Kazuo Hotate, "Complete discrimination of strain and temperature using Brillouin frequency shift and birefringence in a polarization-maintaining fiber," Opt. Express 17, 1248-1255 (2009)

160. T. Cižmár and K. Dholakia, “Exploiting multimode waveguides for pure fibre-based imaging,” Nat. Commun. 3, 1027 (2012).

161. T. G. Euser, G. Whyte, M. Scharrer, J. S. Y. Chen, A. Abdolvand, J. Nold, C. F. Kaminski, and P. S. Russell, “Dynamic control of higher-order modes in hollow-core photonic crystal fibers,” Opt. Express 16(22), 17972– 17981 (2008).

162. Y. Jung, Q. Kang, J. K. Sahu, B. Corbett, R. Winfield, F. Poletti, S. Alam, and D. J. Richardson, “Reconfigurable modal gain control of a few-mode EDFA supporting six spatial modes,” IEEE Photon. Technol. Lett. 26(11), 1100–1103 (2014).

163. O. Shapira, A. F. Abouraddy, J. D. Joannopoulos, and Y. Fink, “Complete Modal Decomposition for Optical Waveguides,” Phys. Rev. Lett. 94(14), 143902 (2005).

164. D. R. Gray, Z. Li, F. Poletti, R. Slavík, N. Wheeler, N. K. Baddela, M. N. Petrovich, A. Obeysekara, and D. Richardson, "Complementary Analysis of

Modal Content and Properties in a 19-cell Hollow Core Photonic Band Gap Fiber using Time-of-Flight and S2 Techniques," in ECOC, paper Mo.2.F.1 (2012).

165. J. W. Nicholson, A. D. Yablon, J. M. Fini, and M. D. Mermelstein, “Measuring the Modal Content of Large-Mode-Area Fibers,” IEEE J. Sel. Top. Quantum Electron. 15(1), 61–70 (2009).

166. D. R. Gray, S. R. Sandoghchi, N. V. Wheeler, N. K. Baddela, G. T. Jasion, M. N. Petrovich, F. Poletti, and D. J. Richardson, "Accurate calibration of S2 and interferometry based multimode fiber characterization techniques," Opt. Express 23, 10540-10552 (2015).

167. George S. D. Gordon, Feng Feng, Qiongyue Kang, Yongmin Jung, Jayanta Sahu, and Timothy Wilkinson, "Coherent, focus-corrected imaging of optical fiber facets using a single-pixel detector," Opt. Lett. 39, 6034-6037 (2014)

168. M. Akiba, K. P. Chan, and N. Tanno, "Full-field optical coherence tomography by two-dimensional heterodyne detection with a pair of CCD cameras," Opt. Lett. 28, 816-818 (2003).

169. I. Roudas, M. Sauer, J. Hurley, Y. Mauro and S. Raghavan, "Compensation of coherent DQPSK receiver imperfections," in Proc. IEEE LEOS Summer Topicals, Portland, OR, Jul, Paper MA3.4. (2007).

170. D. Gloge, “Weakly guiding fibres”, Appl. Opt. 10 2252-8 (1971).

171. D. J. Richardson et. al, “High power fiber lasers: current status and future perspectives,“ JOSA B 27, B63 (2010)

172. S. Ramachandran et. al, “Light propagation with ultralarge modal areas in optical fibers,” Opt. Lett. 31, 1797 (2006).

173. C. D. Poole, J. M. Wiesenfeld, D. J. DiGiovanni, and A. M. Vengsarkar, “Optical fiber-based dispersion compensation using higher order modes near cutoff”, J. Lightwave Technol. 12, 1746–1758 (1994).

174. S. Ramachandran, “Dispersion Tailored Few-Mode Fibers: A Versatile Platform for In-Fiber Photonic Devices,” JLT 23, 3426 (2005).

175. P. Steinvurzel, J. Demas, B. Tai, Y. Chen, L. Yan, and S. Ramachandran, "Broadband parametric wavelength conversion at 1 μm with large mode area fibers," Opt. Lett. 39, 743-746 (2014).

176. D. N. Schimpf, J. Limpert, and A. T¨unnermann, “Optimization of high performance ultrafast fiber laser systems to >10GW peak power,” J. Opt. Soc. Am. B 27, 2051–2060 (2010).

177. L. Dong, H. A. Mckay, A. Marcinkevicius, L. Fu, J. Li, B. K. Thomas, and M. E. Fermann, “Extending effective area of fundamental mode in optical fibers,” J. Lightwave Technol. 27, 1565–1570 (2009).

178. S. Ramachandran, J. W. Nicholson, S. Ghalmi, M. F. Yan, P. Wisk, E. Monberg and F. V. Dimarcello, ”Light propagation with ultra-large modal areas in optical fibers,” Opt. Lett. 27, 1797–1799 (2006).

179. A. Galvanauskas, M. C. Swan, and C.-H. Liu, “Effectively single-mode large core passive and active fibers with chirally coupled-core structures,” paper CMB1, CLEO/QELS, San Jose (2008).

180. F. Stutzki, F. Jansen, T. Eidam, A. Steinmetz, C. Jauregui, J. Limpert, and A. T¨unnermann, “High average power large-pitch fiber amplifier with robust single-mode operation,” Opt. Express 36, 689–691 (2011).

181. J. P. Koplow, D. A. V. Kliner, and L. Goldberg, “Single-mode operation of a coiled multimode fiber amplifier,” Opt. Lett. 25, 442–444 (2000).

182. R. Brüning, P. Gelszinnis, C. Schulze, D. Flamm, and M. Duparré, “Comparative analysis of numerical methods for the mode analysis of laser beams,” Appl. Opt. 52(32), 7769–7777 (2013).

Appendix A

Acronyms

SE	Spectral efficiency
SMF	Single-mode fiber
MMF	Multi-mode fiber
FMF	Few-mode fiber
MIMO	Multiple-input multiple-output
NA	Numerical aperture
LP	Linearly polarized
CP	Cyclic prefix
OFDM	Orthogonal frequency-division multiplexing
DSP	Digital signal processing
PM	Polarization-maintaining
TMF	Two-mode fiber
DMD	Differential mode delay
SDM	Space-division-multiplexing
FOS	Fiber optic sensors
SBS	Stimulated Brillouin scattering
BOTDA	Brillouin optical time domain analysis
BFS	Brillouin frequency shift
BDG	Brillouin dynamic grating
IM/DD	Intensity-modulation/direct-detection
LO	Local oscillator
PD	Photodetector
ASE	Amplified spontaneous emission

RIN	Relative intensity noise
ADC	Analog-to-digital converter
DM	Direct-modulation
DD	Direct-detection
DM/DD	Direct-modulation/direct-detection
RF	Radio frequency
VNA	Vector net-work analyzer
MUX/DEMUX	Multiplexer/demultiplexer
CD	Chromatic dispersion
MD	Modal dispersion
PBC	Polarization beam combiner
PBS	Polarization beam splitter
LPFG	Long-period fiber grating
SLM	Spatial light modulator
SMC	Spatial mode coupler
IL	Insertion loss
LCOS	Liquid Crystal-on-Silicon
LCD	Liquid-crystal display
DVI	Digital visual interface
AR	Anti-reflective
MDM	Mode division multiplexing
OAM	Orbital angular momentum
CDM	Code division multiplexing
TDM	Time division multiplexing
FDM	Frequency division multiplexing
ISI	Inter symbol interference
ICI	Inter-channel interference

MCF	Multi-core fiber
PMD	Polarization mode dispersion
EDFA	Erbium-doped fiber amplifier
RFI	Radio frequency interference
EMI	Electromagnetic interference
FBG	Fiber Bragg grating
PM	Phase-modulation
AM	Amplitude-modulation
CO-OFDM	Coherent optical OFDM
DDO-OFDM	Direct-detection optical OFDM
PAPR	Peak-to-average-power ratio
PD	Photo diode
LD	Laser diode
PBS	Polarization beam splitter
PMC	Polarization-maintaining coupler
TDS	Time-domain sampling scope
ECL	External cavity lasers
IM	Intensity modulator
OA	Optical amplifier
SSMF	Standard single mode fibers
BGS	Brillouin gain spectra
PMF	Polarization-maintain fiber
PCF	Photonic crystal fiber
SLI	Sagnac loop interferometer
RI	Refractive index
BOTDF	Brillouin optical time-domain reflectometry
e-TMF	Elliptical-core two-mode fiber

MI	Michelson interferometer
FPI	Fabry-Perot interferometer
MZI	Mach-Zehnder interferometer
Hi-Bi	high bifringence
PM-FMF	Polarization-maintaining few-mode fiber
PM-PCF	Polarization-maintaining photonic crystal fiber
c-FMF	Circular-core few-mode fiber
OSA	Optical spectrum analyzer
PID	Proportional-integral-derivative
PC	Polarization controller
c-2MF	Circular-core two-mode fiber
ERI	Effective refractive index
FM-BOTDA	Few-mode Brillouin optical time domain analyzer
c-5MF	Circular-core five-mode fiber
MMUX/MDMUX	Mode multiplexer/mode de-multiplexer
CW	Continuous-wave
OC	Optical circulators
MS	Mode stripper
MC	Mode converter
AFG	Arbitrary function generator
DSB	Double-sideband
OBPS	Optical band-pass filter
EOM	Electro-optic modulator
SOP	State of polarization
ML	Mode launcher
S2	Spatial and Spectral
CCD	Charge-coupled device

2-D	Two-dimensional
GSOP	Gram–Schmidt orthogonalization procedure
SI	Step-index
DGD	Differential group delay
ROADM	Reconfigurable optical add-drop multiplexer